On the Role of External Stimuli to Tailor Growth of Organic Thin Films

Dissertation

zur Erlangung des akademischen Grades
doctor rerum naturalium (Dr. rer. nat.)
im Fach Physik, Spezialisierung Experimentalphysik

eingereicht an der
Mathematisch-Naturwissenschaftlichen Fakultät
der Humboldt-Universität zu Berlin

eingereicht von	M. Sc. Linus Pithan
Präsidentin der Humboldt-Universität zu Berlin	Prof. Dr.-Ing. Dr. Sabine Kunst
Dekan der Mathematisch-Naturwissenschaftlichen Fakultät	Prof. Dr. Elmar Kulke
Gutachter	1. Prof. Dr. Stefan Kowarik 2. PD Dr. Stefan Kirstein 3. Prof. Dr. Jens Pflaum
Disputation Tag der mündlichen Prüfung	13.01.2017

Abstract

Applied physical research on soft matter thin films based on small organic molecules has been a vital field of research in the past decade. These efforts led to commercially available optoelectronics in the form of organic light emitting diodes, displays and organic photovoltaics. Key advantages of soft matter thin films are the strong light-matter interaction of molecular materials and the feasibility of roll to roll processing on flexible substrates. Nowadays, a significant share of research on organic thin film structures is attributed to new deposition techniques and the quest for additional growth control parameters in order to follow surface-by-design approaches. Besides the vast variety of molecular species available for organic thin film growth, the functionality of a molecular thin film also crucially depends on the structural properties which are in turn a result of the employed growth process. Here we[1] focus on crystalline thin films, thus, structural parameters in this context include the molecular orientation within the film, crystal polymorphism, the crystal grain size distribution and surface morphologies such as surface roughness, grain boundaries and monolayer coverages.

The first part of this thesis provides an overview of the utilised experimental techniques, in particular x-ray surface diffraction, optical spectroscopy and atomic force microscopy and highlights the applied methods and models. The second part presents the original research performed in the framework of this thesis.
First, we investigate the influence of light on the growth process of the organic semiconductor α-sexithiophene (6T). We find that 6T thin films deposited as conventional in dark environments on potassium chloride (KCl) exhibit a bimodal growth with phase coexistence of both low-temperature (LT) and high-temperature (HT) polymorphs. In contrast, films grown under illumination with 532 nm light at 1.5 W/cm^2 show an increased purity of the LT phase while the HT phase growth is slowed down by a factor four. To understand the mechanisms behind this optical control, we use *in situ* x-ray diffraction, atomic force microscopy (AFM), optical absorption measurements, as well as first principle calculations for the optical absorption spectra of the HT and LT phase. We deduce that the phase purification is due to optical heating of the molecular film and lower cohesive energy of the HT phase compared to the LT phase, so that nucleation and growth of the

[1] Although this dissertation is written by a single author who, if not stated otherwise, also has conducted the presented experiments and analysis, the chosen form of writing employs the use of first person plural throughout the work as it is common practice in scientific publications.

HT phase are significantly reduced by light.

Further, we establish light-directed molecular self-assembly (LDSA) to generate permanently aligned thin films of the molecular semiconductor tetracene and demonstrate direct patterning with light. A moderate light illumination of 5 W/cm^2 induces an optical symmetry axis perpendicular to the light polarisation direction leading to azimuthally photoaligned films on isotropic, amorphous substrates. Thus, LDSA can be regarded as a new degree of freedom in the quest for control-parameters in organic thin film growth with the ability of bridging nano scale self-assembly with photo-lithography on the meso- and makro scale.

We also discuss the impact of dynamic temperature oscillations on the time scales of molecular monolayer growth during organic molecular beam deposition. We use x-ray growth oscillations to trigger rapid thermal cooling cycles during the nucleation phase of each individual monolayer while growing the organic semiconducting molecule PTCDI-C_8 and thereby enhance layer-by-layer growth. We follow the concept of two mobilities to strongly increase the island density during nucleation and selectively increase interlayer diffusion at later stages of monolayer growth. Based on analytical growth models and phase field simulations, we analyse the interplay between interlayer transport and the size of molecular islands to understand kinetic processes during growth that define the surface morphology.

In a fourth experiment we show how thermal annealing can be used to improve smoothness and to increase the lateral size of crystalline islands of n-tetratetracontane (TTC, $C_{44}H_{90}$) films. By means of *in situ* x-ray diffraction we find an optimum temperature range leading to improved texture and crystallinity while avoiding an irreversible phase transition that reduces crystallinity again. We employ real-time optical phase contrast microscopy with sub-*nm* height resolution to track the diffusion of TTC across monomolecular step edges which causes the unusual smoothing of a molecular thin film during annealing. We show that the lateral island sizes increase by more than one order of magnitude from 0.5 μm to 10 μm. This desirable behaviour of 2d-Ostwald ripening and smoothing is in contrast to many other organic molecular films where annealing leads to dewetting, roughening, and a pronounced 3d morphology. We rationalise the smoothing behaviour with the highly anisotropic attachment energies and low surface energies of TTC.

Kurzfassung

Die Physik von Dünnschichtsystemen aus weicher Materie is eines der Forschungsfelder, dem in der letzten Dekade gesteigerte Aufmerksamkeit entgegen gebracht wurde. Große Fortschritte in der angewandten Forschung seit den frühen 2000er Jahren haben im Bereich der organischen Elektronik und Optoelektronik zu kommerziell nutzbaren Elementen geführt. Trotzdem stellt die Wachstumskontrolle für die Produktion von maßgeschneiderten, funktionalen organischen Dünnschichtmaterialien weiterhin eine Herausforderung dar. In dieser Arbeit werden neuartige Strategien zur Wachstumskontrolle aufgezeigt und analysiert, mit denen sich die physikalischen und funktionalen Eigenschaften molekularer Schichtsysteme gezielt beeinflussen lassen. Ein Fokus liegt dabei auf der Untersuchung des Einflusses von optischen Feldern auf das Wachstumsverhalten von kristallinen, organischen Strukturen. Ein weiterer Schwerpunkt wird auf das Grundlagenverständnis von thermisch aktivierten, kinetischen Prozessen, insbesondere der Diffusion, die die Morphologie während und nach dem Schichtwachstum beeinflussen.

Nach einer detaillieren Erläuterung der verwendeten Röntgen-Streugeometrien, optisch-spektroskopischen Methoden (insb. differentielle Reflektionsspektroskopie sowie polarisationssensitive Photolumineszenzspektroskopie) und Rasterkraftmikroskopie werden vier experimentelle Studien zur Kontrolle von strukturgebenden Prozessen in organischen dünnen Filmen dargelegt.
Zuerst wird am Beispiel des molekularen Halbleiters Sexithiophen (6T) gezeigt, wie sich Kontrolle über das Kristallphasengleichgewicht während des Wachstums auf Kaliumchlorid (KCl) erzielen lässt. Unter konventionellen Bedingungen wächst 6T parallel in zwei Kristallpolymorphen, die üblicherweise als Hochtemperatur (HT) und Niedrigtemperatur (LT) Phasen bezeichnet werden. Durch Beleuchtung mit 532 nm Laser Licht (1.5 W/cm^2) lässt sich das Wachstum der HT Phser um einen Faktor vier unterdrücken und dadurch quasi-phasenreines LT Wachstum induzieren. In dieser Studie wird der nachgewiesene Einfluss von Licht auf das Kristallwachstum in Bezug auf die optischen Eigenschaften der beiden Kristallformen und ihre thermische Stabilität diskutiert und gezeigt, dass die HT Phase 532 nm Laser Licht sowohl stärker absorbiert als auch thermisch instabiler ist. Auf Grundlage dieser Beobachtung wird die Reduktion des Anteils von HT Kristalliten auf Basis eines opto-thermischen Mechanismus diskutiert.

Im zweiten Teil der Arbeit wird eine neue Herangehensweise zur direkten Ausrichtung von Molekülkristallen im optischen Feld während ihrer Entstehung studiert. Außerdem wird

das damit verbundene Wachstum von polykristallinen dünnen Schichten mit anisotropen, optischen und strukturellen Eigenschaften erläutert. Am Beispiel von Tetracene wird gezeigt wie sich so optische anisotrope Absorptionseigenschaften von Molekülen dazu nutzen lassen den Brechungsindex eines polykristallinen Films lokal durch ein photolitographisches Verfahren zu beeinflussen. Die in Rahmen dieser Arbeit entwickelte lichtinduzierte molekulare Selbstassemblierung (LDSA) kann als Ausgangpunkt für neue Herstellungsverfahren von optoektronischen und photonischen Bauelementen basierend auf organischen Materialien gesehen werden.

Im dritten Teil wird der Einfluss von dynamisch variierenden Wachstumsbedingungen während des Schichtwachstums von PTCDI-C_8 studiert. Es wird gezeigt, dass sich die Oberflächenrauigkeit von PTCDI-C_8 (N,N'-Dioctyl-3,4,9,10-perylenedicarboximide) Schichten stark reduzieren lässt, indem zu Beginn des Wachstums jeder individuellen molekularen Monolage die Nukleationsdichte stark erhöht und in den darauf folgenden Wachstumsphasen die Diffusivität gezielt gesteigert wird. Diese zeitliche Kontrolle von Nukleationsdichte und molekularer Diffusivität wird durch schnelle Substrattemperaturvariationen während des Wachstums induziert, welche durch Röntgen-Wachstumsoszillationen mit dem Filmwachstum synchronisiert werden. Durch die Übertragung des „Konzeptes der zwei Mobilitäten" von anorganischer Homoepitaxie auf organische, heteroepitaktische Systeme wird in dieser Arbeit ein Verfahren zur Herstellung glatterer Grenzflächen in molekularen Dünnschichtsystemen entwickelt.

Im vierten Teil wird das Diffusionsverhalten von n-Alkan Schichten ebenfalls unter thermischen Einflüssen betrachtet. Es wird gezeigt, dass die inhärente molekulare Anisotropie von $C_{44}H_{90}$ Molekülen (TTC) sowie die sehr geringe, stark anisotrope, Oberflächenenergie dieses Materials ein ungewöhnliches Diffusionsverhalten auslöst. So weisen TTC Schichten eine durch tempern induzierte Oberflächenglättung auf. Dies steht im Gegensatz zu dem üblicherweise beobachteten, durch Temperatur induziertem, 3d Kornwachstum in molekularen Dünnschichten, welches bei den meisten kristallinen organischen Materialien beobachtet wird. Durch Einsatz einer speziellen optischen Reflektionsmikroskopiemethode mit Phasenkontrast lässt sich der Materialtransport zwischen individuellen TTC Schichten ortsaufgelöst festhalten und laterale Ostwaldreifung im TTC Film dokumentieren. Begleitende Beugungsexperimente zeigen außerdem strukturelle Parallelen zwischen Dünnfilmen, die aus mehreren molekularen Schichten bestehen, und selbstassemblierten TTC Monolagen auf.

Zusammenfassend werden in dieser Arbeit also neue Wege erläutert um durch Licht und dynamische Temperaturkontrolle gezielt Einfluss auf den Wachstumsprozess von molekularen Dünnschichtsystemen zu nehmen.

Table of Contents

1

Controlling Molecular Thin Film Growth

While there is the guiding principle *form follows function* in architecture and design, the reverse is found in the growth physics of today's organic (opto-) electronics. An elementary principle concerning the growth of organic thin film structures is *functionality follows structure*, as will be discussed in the following.

As far as the molecular structure is concerned there are two groups of organic materials: polymers and small molecules. While conjugated polymers show a tendency to form glasses and semicrystalline structures, small molecules on the other hand are likely to form molecular crystals. This thesis focuses on the latter group.
Molecular materials lay the foundation of organic devices such as organic field-effect transistors,[1,2] organic photovoltaics,[3,4] and organic light emitting diodes[5,6]. In comparison to conventional, atomistic semiconductors such as silicon or gallium arsenide, crystalline molecular materials have an additional, intermediate structural level between the atoms that they are made of and their crystal structure. Instead of defining a crystal structure based on few atoms per unit cell as in conventional semiconductors, there are whole molecules - which assembled of atoms themselves - in the unit cell of a molecular crystal. The unit cells of the here investigated molecular crystals consist of 2 to 4 molecules with 30 to 140 atoms each. The large number of atoms in the unit cell together with the flexibility of organic synthesis gives rise to a broad, nearly infinite spectrum of compounds that can be used as crystalline organic semiconductors.[7]
While there are mainly covalent chemical bonds in conventional semiconductors, there is a hierarchy of forces found in molecular semiconducting crystals: strong, covalent bonds lead to the formation of molecules and weaker, intermolecular *van der Waals* forces result in the self-assembly of individual molecules into molecular crystallites.[8]

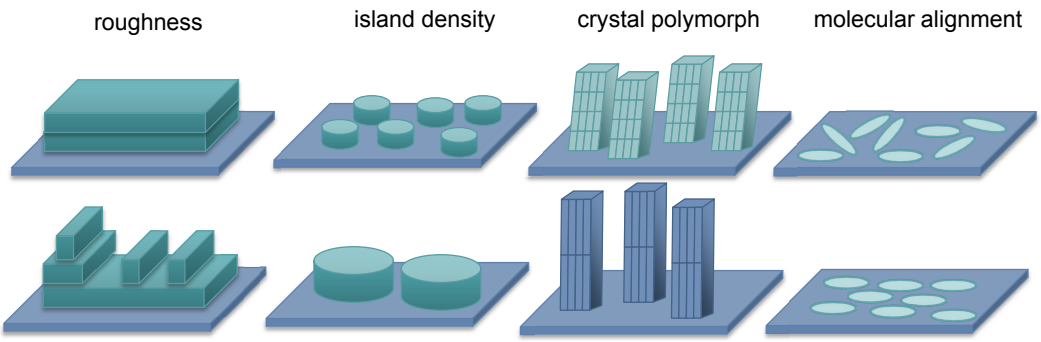

FIGURE 1.1: Structural characteristics of organic thin film growth. Control over roughness, island density, crystal phase and molecular alignment enables the fabrication of thin films with predefined functionality.

The molecular crystal structure and thereby the molecular packing defines the overlap of π-conjugated orbitals of neighbouring molecules and thus tunes the functionality of the material.[9,10] Besides the crystal structure, morphological characteristics and microscopic structure (such as surface roughness, island densities and unit cell alignment) are important in terms of functionally in organic thin films (Figure 1.1). Together these characteristics define the structural aspects and give rise to the functionality of an organic thin film structure.

Since there is a huge number of parameters and properties that define the thin film's functionality, there is an **ongoing quest for new control parameters during growth to optimise organic thin film structures**.[11,12]
Growth control in organic systems is especially demanding since molecular materials exhibit a large number of internal degrees of freedom. While in atomic systems only the position of the atom (with isotropic shape) in a crystalline unit matters, the situation is different in molecular crystals. In these systems the anisotropic shape of the molecule leads to additional degrees of freedom and not only the position, but also the orientation of the molecules within the unit cell become important.[13] Furthermore, the interaction potential of neighbouring molecules is much more complex due to the aforementioned anisotropy, the relatively far ranging *van der Waals'* forces and the ability of some molecules to change their confirmation during growth.[14] These characteristics of molecular crystals give rise to a multitude of crystal polymorphs of the same compound.

Besides control parameters that affect the thin film structure as a whole, local control is desirable to produce **patterned and locally structured films** to fabricate functional thin films and devices. While photo-lithography is commonly used in inorganic materials it faces difficulties when transferred to organic materials due to the incompatibility of photo resists and etching processes with soft matter materials.[12,15,16]

To tackle current challenges of growth control of organic thin films, **this thesis aims to address the applicability of additional external stimuli as control parameters**. Further the **underlying interaction mechanisms are analysed in detail**. Here, we

especially focus on

- **the potential of optical fields to control molecular thin film growth,**
- **the ability of temperature modulations during monolayer growth to enhance thin film smoothness,**
- **the influence of molecular anisotropy during annealing processes.**

Optical fields as control parameter in organic thin film growth

Light is a particularly simple control parameter for molecular growth because it can be applied remotely and can easily be incorporated into growth environments. Moreover, it can be shaped locally to imprint patterns and its polarisation state can be precisely controlled. It is known that some organic molecules polymerise under photo-excitation and that thereby the molecular building blocks are changed. This is observed for example in C_{60} films[17] under intense illumination or in monolayers of sexithiophene under strong UV irradiation.[18] Additionally, the electronic properties such as the surface potential can be changed through illumination during growth as shown by Sugi *et al.*.[19] The morphology of thin films can be altered through laser illumination as demonstrated by Balzer and Rubahn[20] who showed the local formation of nanostructures due to optically increased substrate temperature or as presented by Chen *et al.* based on photo-induced electrical charging.[21] Furthermore, the influence of light on the preferential molecular orientation in hetero-epitaxial growth on single crystalline substrates has been discussed,[22] but could not be reproduced in the framework of this thesis.

Light can also induce structural order via an additional photo-alignment layer based on photo-crosslinkable or photo-isomerisable material.[23,24] In conclusion, light has a high potential as a control parameter in organic thin film growth based on a variety of light-matter interaction mechanisms. However, prior to the work presented in this thesis, no direct influence of light on the molecular crystal structure and molecular alignment on amorphous substrates has been reported.

In Chapter 4 light is used to enhance phase purity in sexithiophene (6T) thin films, while in Chapter 5 we present a self-photoalignment method that allows one to control the azimuthal alignment of tetracene molecules in thin films on amorphous substrates. Both studies are based on illumination during growth and in the latter we additionally demonstrate the possibility to combine local patterning and molecular alignment in a single method. Thus, this method allows one to bridge the scale between alignment on molecular length scales of self-assembly and patterning on macroscopic length scales spanning over several molecular crystal grains.

Growth control via tailored molecular diffusion processes

In Chapter 6 we demostrate the beneficial influence of dynamic temperature control in form of rapid thermal cycles on the growth of the perylene derivative PTCDI-C_8 and thereby enhance the thin film surface smoothness. Instead of growing organic thin films at constant substrate temperature as in conventional organic molecular beam deposition (OMBD),[13,25] we synchronise dynamic temperature modulations to the evolution of individual monolayer growth. Thereby we transfer the *concept of two mobilities* known from inorganic homo-epitaxial growth to organic thin film growth.[26–28] This concept to control thin film growth relies on real-time knowledge of the coverage of individual molecular monolayers during growth which we acquire via anti-Bragg growth oscillations using modern x-ray diffraction measurements.[29]
For a detailed understanding of the involved diffusion and nucleation phenomena we present experimental findings as well as phase field simulations[30] which capture the observed effect in simulated, time resolved real space morphologies.

Molecular anisotropy and annealing

In contrast to the preceding studies, we focus on post-growth processes and treat thermal annealing in n-alkane thin films in Chapter 7. This study is motivated by the use of Tetracontane ($C_{44}H_{90}$) as a passivation layer in organic field effect transistors[31,32] and aims at surface smoothening and maximising the lateral island dimension. Compared to other molecules, n-alkanes are known for their interesting diffusion and aggregation behaviour close to their melting temperature and surface freezing.[33–35] Here we analyse thermally induced directed molecular diffusion processes which therefore can be regarded as control parameter to alter thin film structures.

Organisation of this thesis

This thesis is organised as follows: In part I, the relevant methods and techniques are introduced and explained in detail. Experimental findings and their interpretation are presented in part II consisting of the chapters 4 to 7. The key findings are summarised in part III that also provides a comprehensive conclusion and outlook.

I

Introductory Notes

2

Selected Fundamentals

In this chapter we review some fundamental aspects of organic thin film growth and molecular crystals. We especially focus on those facets that we will get back to during the discussion of the experimental studies in the following chapters. First we discuss molecular absorption spectra and their relation to the spectra of corresponding molecular crystals. After that we summarise in three sections the characteristics of anisotropic thin film structures, surface diffusion processes and polymorphism in organic crystals.

2.1. Light Matter Interaction in Organic Solids

Compared to other materials, organic molecules absorb visible light extremely efficiently. Absorption coefficients of molecular crystals typically lie in the range of $10^5\ cm^{-1}$ [8] so that they absorb light about 10 to 100 times more efficiently than silicon (with absorption coefficients between $10^3\ cm^{-1}$ and $10^4\ cm^{-1}$),[36] so that layers of only few nm already absorb a significant portion of light. This strong interaction with light makes organic thin films interesting candidates for optoelectronic applications. Recent examples are organic solar cells or commercially available organic light emitting diode (OLED) displays. To develop a basic understanding of the absorption spectra of organic molecular solids, the optical properties and excitations within a single molecule have to be discussed. Further, the formation of excited states that are delocalised over several molecules in a molecular crystal (so called *excitons*) need to be taken into account.

2.1.1. Absorption Spectra of Single Molecules

The spectral shape and position of optical absorption and emission features of organic semiconducting molecules are determined by the involved excited electronic and vibrational states. In the next paragraph, the quantum mechanical treatment of molecular optical transitions is presented following mostly Lanzani,[37] where it is discussed in more detail. Here we aim at an expression for the absorption cross section σ for optical absorption processes in molecular materials.

Staying in the framework of the *Born-Oppenheimer approximation* (also called adiabatic approximation) allows to express the molecular wave function as $\Psi(\mathbf{q},\mathbf{Q}) = \psi_e(\mathbf{q})\chi^e_\nu(\mathbf{Q})$, as it is based on the idea that nuclear and electronic motions can be treated separately.[38] The index e corresponds to an electronic state while ν represents the vibrational quantum number. The electronic wave function $\psi_e(\mathbf{q})$ only depends on the electronic coordinates $\mathbf{q}$ and the vibrational wave function $\chi^e_\nu(\mathbf{Q})$ solely depends on the nuclei coordinates $\mathbf{Q}$ for a given electronic state e.

The dipole moment operator that describes the interaction between light and the molecule can be written as

$$\hat{\mathbf{M}} = -q\sum_j \hat{\mathbf{r}}_j + q\sum_A Z_A\hat{\mathbf{R}}_A. \tag{2.1}$$

Here, the first term sums all electrons j (with elementary charge q) at their respective positions $\hat{\mathbf{r}}_j$ in the molecule and the second one sums all nuclei A with charges $-qZ_A$ at $\hat{\mathbf{R}}_A$. The transition matrix element that describes the amplitude of an optical transition - here from the ground state (G,ν) to an excited state (E,ν') - is given by

$$\begin{aligned}
\mathbf{M}_{G_\nu\to E_{\nu'}} \quad & \langle\Psi_E|\,\hat{\mathbf{M}}\,|\Psi_G\rangle && (2.2)\\
= \quad & \left\langle\psi_E\chi^E_{\nu'}\right|\hat{\mathbf{M}}\left|\psi_G\chi^G_\nu\right\rangle && (2.3)\\
= \quad & \langle\psi_E|\psi_G\rangle\left\langle\chi^E_{\nu'}\right|q\sum_A Z_AR_A\left|\chi^G_\nu\right\rangle - \langle\psi_E|\,q\sum_j\hat{\mathbf{r}}_j\,|\psi_G\rangle\left\langle\chi^E_{\nu'}|\chi^G_\nu\right\rangle && (2.4)
\end{aligned}$$

The first term in 2.4 vanishes in *Born-Oppenheimer approximation*, as the electron ground-state and excited state are orthogonal. Therefore, the transition dipole moment (TDM) can be identified as

$$\mathbf{M}_{G_\nu\to E_{\nu'}} = \underbrace{\langle\psi_E|-q\sum_j\hat{\mathbf{r}}_j\,|\psi_G\rangle}_{\mathbf{M}_{G\to E}}\left\langle\chi^E_{\nu'}|\chi^G_\nu\right\rangle. \tag{2.5}$$

While the overall intensity of the transition $\mathbf{M}_{G_\nu\to E_{\nu'}}$ is strongly influenced by the vibrational overlap integral $\left\langle\chi^E_{\nu'}|\chi^G_\nu\right\rangle$, the spectral position is given by the electronic dipole moment $\mathbf{M}_{G\to E}$. For the absorption cross section we have

$$\sigma = |\mathbf{E}\cdot\mathbf{M}_{G\to E}|^2\underbrace{\left|\left\langle\chi^E_{\nu'}|\chi^G_\nu\right\rangle\right|^2}_{FC}, \tag{2.6}$$

with the external electrical field unit vector **E** and the *Franck Condon Factor FC*.[37,39,40]

2.1.2. Polarisation of Molecular Transitions

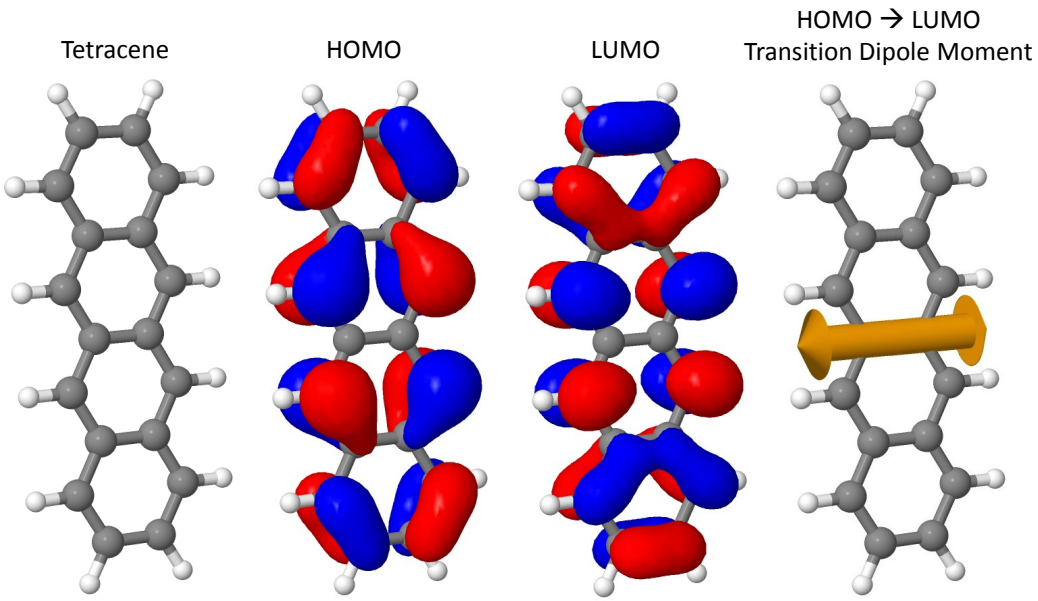

FIGURE 2.1: The optical properties of the $S_0 \rightarrow S_1$ transition in organic materials is defined by electronic transitions from the *highest occupied molecular orbital* (HOMO) to the *lowest unoccupied molecular orbital* (LUMO). The presented iso-surfaces of the according molecular wave functions with colour coding of the phase are calculated with *GAMESS* in Hartree approximation.[41] Based on the symmetry of HOMO and LUMO the orientation of the *transition dipole moment* (TDM) can be derived.

The orientation of $\mathbf{M}_{G\rightarrow E}$ within the molecule defines the polarisation direction of the according transition. Through the geometry of the involved electronic wave functions ψ_G and ψ_E, the orientation of the TDM in the molecule is determined. As this thesis focuses on optical transitions within semiconducting, organic molecules, here the $S_0 \rightarrow S_1$ transition in tetracene will be discussed exemplary.
In Figure 2.1 iso-sufaces of electronic wave functions for the *highest occupied molecular orbital* (HOMO) and *Lowest Unoccupied Molecular Orbital* (LUMO) of tetracene are shown. To describe the optical transition $S_0 \rightarrow S_1$ it is in this case sufficient to only consider the single electron wave functions (Hartree approximation) corresponding to HOMO and LUMO. In the absorption process one electron is excited from the HOMO into the LUMO as described by $\langle\psi_{\mathrm{LUMO}}| - q\hat{\mathbf{r}}\,|\psi_{\mathrm{HOMO}}\rangle$.
Considering the symmetries of HOMO and LUMO allows concluding on the orientation of $\mathbf{M}_{\mathrm{HOMO}\rightarrow\mathrm{LUMO}}$ with respect to the molecular axes. Due to the antisymmetry of $\hat{\mathbf{r}}$, only the 'odd' phase contribution with respect to a reflection plane does not vanish in the integral $\langle\psi_{\mathrm{LUMO}}| - q\hat{\mathbf{r}}\,|\psi_{\mathrm{HOMO}}\rangle$.[39] For the visualised $S_0 \rightarrow S_1$ transition in Figure 2.1 this implies

that there is no contribution to $\mathbf{M}_{\mathrm{HOMO}\rightarrow\mathrm{LUMO}}$ along the long molecular axis as the HOMO and LUMO are antisymmetric in this direction with respect to the centre of mass of the molecule. Along the short molecular axis there is a different situation: While the HOMO is antisymmetric the LUMO is symmetric, therefore $\mathbf{M}_{\mathrm{HOMO}\rightarrow\mathrm{LUMO}}$ does not vanish in this direction. HOMO and LUMO are antisymmetric normal to the molecular plane, thus there is only a contribution to $\mathbf{M}_{\mathrm{HOMO}\rightarrow\mathrm{LUMO}}$ along the short molecular axis.

2.1.3. Davydov Splitting in Molecular Crystals

In the previous section the optical properties of a single molecule are discussed. With respect to crystalline, organic thin films, however, the solid state optical absorption and emission spectra are of great relevance. The optical characteristics of molecular crystals are defined through the optical properties of the individual molecules as well as by their interaction. Here we will focus the discussion on the simplest case, the so-called mini-excitons[42] that are spread over two molecules in a molecular dimer. They are e.g. found in crystals with a non-primitive unit cell and give rise to the so called *Davydov-Splitting*, which is also known as factor group splitting. The following discussion is based on the original work by Davydov[43] and Kasha[44] as well as on the textbooks (see references [8, 37, 45–47]).

The theoretical treatment of a molecular dimer in a strongly interacting π-conjugated system of equivalent molecules presented here is based on the assumption that there is no electron orbital overlap between the two molecules in states involved in the optical transition and that there is no electron exchange between the molecules on the relevant time scale for the excitation.[47] Following the discussion above we use the single molecule wave function Ψ, that is labelled with Ψ^1 and Ψ^2 to account for the two molecules 1 and 2 in the dimer. For a more convenient notation we do not explicitly note the vibrational states in the following discussion. The dimer ground state of two uncoupled molecules can be approximated by $|\Phi_G\rangle = |\Psi^1_G\Psi^2_G\rangle$. Within the discussed approximation we assume that the dimer wave function carrying a single S_1 excitation by either of the following linear combinations

$$\Phi_{\pm} = \frac{1}{\sqrt{2}}\left(\Psi^1_E\Psi^2_G \pm \Psi^1_G\Psi^2_E\right) \tag{2.7}$$

due to the symmetry of the problem.[47] Using the definition of the transition dipole moment as above for the two individual molecules $\mathbf{M}^1_{G\rightarrow E} = -q\langle\Psi^1_E|\mathbf{r}|\Psi^1_G\rangle$ and $\mathbf{M}^2_{G\rightarrow E} = -q\langle\Psi^2_E|\mathbf{r}|\Psi^2_G\rangle$, we can apply the same concept to Equation 2.7 and find

$$\begin{aligned}
\mathbf{D}_{\pm} &= -q\langle\Phi_E|\mathbf{r}|\Phi_G\rangle && (2.8)\\
&= \frac{-q}{\sqrt{2}}\langle\Phi_{\pm}|\mathbf{r}|\Psi^1_G\Psi^2_G\rangle && (2.9)\\
&= \frac{-q}{\sqrt{2}}\left[\langle\Psi^1_E\Psi^2_G|\mathbf{r}|\Psi^1_G\Psi^2_G\rangle \pm \langle\Psi^1_G\Psi^2_E|\mathbf{r}|\Psi^1_G\Psi^2_G\rangle\right] && (2.10)\\
&= \frac{1}{\sqrt{2}}\left[\mathbf{M}^1_{G\rightarrow E} \pm \mathbf{M}^2_{G\rightarrow E}\right]. && (2.11)
\end{aligned}$$

Therefore, the HOMO → LUMO transition in single molecule splits into two Davydov components that we will label with $\mathbf{D}_+ = \frac{1}{\sqrt{2}}\left[\mathbf{M}^1_{S_0\to S_1} + \mathbf{M}^2_{S_0\to S_1}\right]$ and accordingly $\mathbf{D}_- = \frac{1}{\sqrt{2}}\left[\mathbf{M}^1_{S_0\to S_1} - \mathbf{M}^2_{S_0\to S_1}\right]$. $\mathbf{D}_+$ and $\mathbf{D}_-$ are always orthogonally polarised. From an energetic point of view, the transitions according to $\mathbf{D}_+$ and $\mathbf{D}_-$ are spectrally separated.
We now assume a dimer Hamilton operator H_D of the form $H_D = H^1 + H^2 + V^{12}$, where H^1 and H^2 are the Hamilton operators for the isolated molecules and V^{12} contains the intermolecular interaction. For the ground state energy of the dimer we find $E_G = \langle \Psi^1_G \Psi^2_G | H_D | \Psi^1_G \Psi^2_G \rangle = 2E^1_G + D_G$ with the ground state energies of the isolated molecules E^1 and the energy correction D_G that lowers the ground state energy.
For the excited state we obtain

$$E^{\pm}_E = \langle \Phi_\pm | H_D | \Phi_\pm \rangle = E^1_G + E^1_E + \underbrace{\langle \Psi^1_E \Psi^2_G | V^{12} | \Psi^1_E \Psi^2_G \rangle}_{D_E} \pm \underbrace{\langle \Psi^1_E \Psi^2_G | V^{12} | \Psi^1_G \Psi^2_E \rangle}_{\epsilon}, \tag{2.12}$$

with the energy correction for the exited state D_E (also known as *Coulomb interaction energy*) and the exciton energy splitting ϵ (also *resonance interaction energy*). The absolute

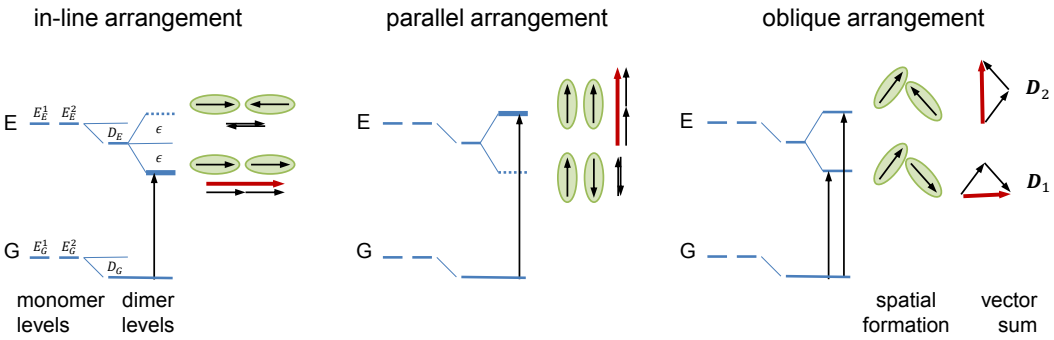

FIGURE 2.2: Emergence of dimer levels from a monomer spectrum in three geometrical formations (green). The transition probability is given by the absolute value of of the vector sum (red) leading to red-shifted J-aggregate spectrum (left), blue-shifted H-aggregate spectrum (centre) and two transitions with non-vanishing probability for oblique molecular arrangement (right).

transition probabilities strongly depend on the orientations of two TDMs in the dimer with respect to each other. We first study the more simple cases shown in Figure 2.2a and b. Two molecules arranged such that their transition dipole moments are in-line, also known as J-aggregates[1] (Figure 2.2a) show no transition probability for the out-of-phase arrangement and a high transition probability for the in-phase arrangement. Therefore, only the lower Davydov component can be seen in the absorption spectrum. Compared to the monomer spectrum, the J-aggregate spectrum appears red shifted.
In a setup with parallel aligned transition dipole moments, also called H-aggregates[2] (Figure 2.2b), we find the opposite behaviour. Here, the in-phase arrangement leads to a high transition probability for the higher Davydov component, whereas the transition corresponding to the out-of-phase arrangement is forbidden.

[1] J refers to E.E. Jelley who first described the phenomenon
[2] hypsochromic aggregates

To understand transition probabilities and spectral shapes in organic crystallites with molecular herringbone arrangement, we now focus on oblique transition dipoles, as found e.g. in tetracene crystals (discussed in Chapter 5). We find that neither of the two Davydov components vanishes completely (see Figure 2.2c). The in-phase arrangement corresponds to $\mathbf{D}_1$ (stronger head-to-tail character, thus, less dipole repulsion) and the out-of-phase arrangement to $\mathbf{D}_2$. The relative intensity distribution between the two transitions depends strongly on the exact geometrical arrangement of the molecules with respect to each other. Regarding molecular crystals instead of isolated dimers leads to a splitting of the dimer energy levels into exciton bands. [8]

2.2. Anisotropic Organic Thin Films

As we will highlight in Chapter 5 the above discussed anisotropic optical characteristics of molecular systems can be utilised to design molecular thin films consisting of aligned molecular crystallites. Therefore we present some general considerations concerning molecular and crystal orientations in thin film systems.

As there is a huge variety of molecular species used to fabricate organic thin films for a wide range of potential applications, ranging from photovoltaic energy conversion to (opto-) electronics, there are strongly differing demands regarding the thin film functionality and structure. While in organic photovoltaics so called bulk-hetero junctions, mostly relying on amorphous organic thin films, play a dominant role, [48] there are other applications such as organic field effect transistors where crystalline thin film structures are demanded. [31] Depending on the application and requested functionality, therefore, differing solid state arrangements are desirable.

From a structural point of view, amorphous thin films exhibit no texture[3] at all while the majority of crystalline organic thin films show a uniaxial texture through a defined crystallographic contact plane with an underlying substrate. This contact plane may differ depending on the substrate material, [49] the substrate surface [50] or the surrounding conditions during growth. [51]
In order to make full use of anisotropic material properties e.g. anisotropic charge transport, [8,52–54] biaxial texture is required in order to be able to also exploit azimuthal anisotropy in thin film structures. There are different strategies to produce organic thin films featuring biaxial texture. Using single crystalline substrates with suitable surface properties (lattice matching) encourages pseudoepitaxial growth and thereby imposes biaxial texture. [55–57] As this significantly reduces the choice of substrate materials, especially when aiming at flexible electronics, another strategy is to use additional alignment layers. [58–60]

A widely used way to indirectly control thin film formation processes and achieve

[3] In crystallography, texture is the distribution of crystallographic orientations of a polycrystalline sample. A sample with fully random orientations is said to have 'no' texture.

anisotropic structures is to add additional photoalignment layers prior the deposition of the compound with the desired functionality.[58–60] These layers consist of a photo-responsive molecular material which forms anisotropic structural properties under irradiation. These properties can be, e.g., topographical patterns which are formed through anistotropic rearrangement reactions or photodimerisation.
Organic semiconducting molecules deposited on top of this crystalline substrate may inherit this anisotropy.[15,61] As photoalignment layers often polymeric materials are used which are photo-crosslinkable or photo-dissociable.[58] Also materials containing azobenzene are used that make use of light induced reorganisation processes through photo-isomerisation.[59]

Within the framework of this thesis a new approach to induce biaxial texture in organic thin films through light without the need of an additional alignment layer has been developed that is discussed in Chapter 5.

2.3. Surface Diffusion Processes

Some of the studies presented in this thesis rely on tailored molecular diffusion, rather than light as control parameter. Here we shine light on the basics of diffusive processes during thin film growth.
In order to analyse growth processes of organic thin films and to understand the evolution of structural quantities such as the island density and surface roughness, a comprehensive understanding of surface diffusion processes is crucial. Apart from energetic considerations concerning the growth mode (Volmer–Weber, Stranski–Krastanov and Frank–van der Merwe),[13,28] surface diffusion and inter-layer transport of diffusing ad-atoms or ad-molecules (unbound, solitary particles) are processes defining the thin film morphology during the growth process.[13,28]

Diffusion processes as dealt with here are classical rate processes that follow the Boltzmann

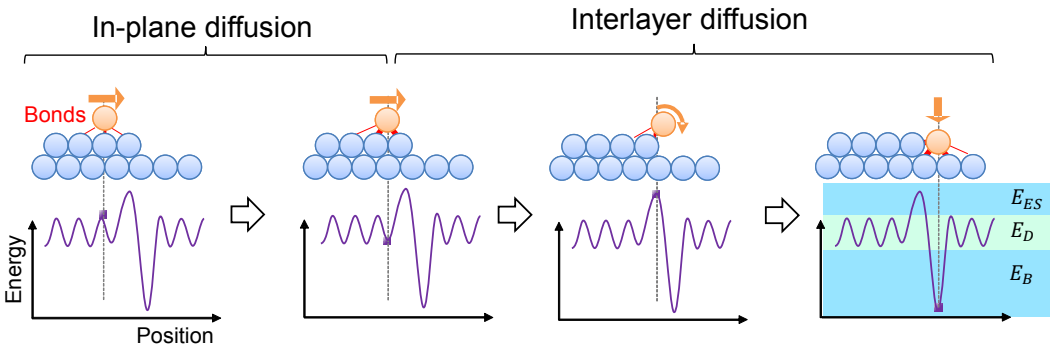

FIGURE 2.3: Simplistic energy landscape of surface diffusion processes including the binding energy E_b. Cf. [62]

statistics. Therefore, rates in diffusive processes can be captured in the form

$$R = \nu_0 \, exp\left(-\frac{Q}{k_B T}\right). \tag{2.13}$$

The exponential term is known as Boltzmann factor with the Boltzmann's constant k_B and Q the activation energy. The attempt frequency ν_0, also known as prefactor, captures the time-scale and depends e.g. on geometric details of the diffusion path or the atom density.[63] The expression in Equation 2.13 is also referred to as *Arrhenius rate*.

In Figure 2.3 diffusion steps of a molecule on a surface and the according potential landscape are shown in a schematic way. When diffusing within the same monolayer (in-plane diffusion) without being close to surface step edges, the molecule experiences a periodic potential (modulation depth E_D) which can be interpreted as the origin of epitaxial growth since the crystal lattice sites are energetically favourable. In the vicinity of surface step edges, however, there is a position of particularly low energy (last scene in Figure 2.3) where the molecule is integrated into the former edge gaining the binding energy E_b. In order to get to this position, an additional energy barrier, the Ehrlich-Schwoebel barrier E_{ES}, has to be overcome.

2.4. Polymorphism in Organic Crystals

Organic materials often crystallise in different solid state crystal structures that are all based on the same molecules.[64] This behaviour is known as crystal polymorphism. As we will discuss the impact of the crystalline structure on material properties in the main part of this theses it is important to also consider crystal polymorphs in this discussion.

Many planar, semiconducting organic molecules that are of interest for this study are known to crystallise in more than one crystal structure. This includes e.g. oligothiophenes,[65,66] polyacenes,[67,68] para-phenyles[69] and perylene derivates.[57] Many of the polymorphic structures of one particular molecule are structurally closely related.[65,68] Some polymorphs only occur in proximity to surfaces or interfaces of thin films and do not exist in single crystals.[70,71] These polymorphs are called surface induced phases. It needs to be mentioned, that in the context of organic thin films, different crystal orientations with respect to the substrate are sometimes misleadingly also labelled as distinct crystal phases.[72]

The physical properties of organic crystals and crystalline thin films may differ strongly depending on the respective polymorph of the crystal.[11] Examples of polymorph depended properties can be found in form of differing charge carrier mobilities,[11,73,74] optical constants,[66,75] or thermal stabilities.[76]

Thus, control over polymorphism in organic thin films is important in structure-by-design and surface-by-design approaches in order to define desired functionalities for organic (opto-)electronic devices.

3
Methods & Techniques

In this chapter all relevant techniques and methods used in the framework of this thesis are discussed in detail. First organic molecular beam deposition is presented as a sample preparation method. Afterwards x-ray scattering and spectroscopic techniques as well as atomic force microscopy and phase contrast microscopy are introduced. Finally a brief description of phase-field theory is given which we use to simulate the surface evolution of grown thin film structures.

3.1. Organic Molecular Beam Deposition OMBD

We use a portable ultra-high vacuum (UHV) chamber as shown in Figure 3.1 to grow [13,25] organic thin film structures for *in situ* and *ex situ* experiments. The chamber is optimised for the use in x-ray diffractometers which highly constrains its overall size. The chamber is equipped with a 360° Beryllium windows to enable x-ray scattering experiments. The portability of the setup enables *in situ* experiments at synchrotron light sources as described in Chapter 3.2. A molecular raw material (in form of powder) is thermally evaporated in custom build crucibles and deposited on a substrate. The growth rate is monitored by a quartz crystal microbalance (QCM). The substrate temperature can be controlled in a temperature range between 100 K and 900 K.

The setup is highly adaptable and has been modified for each experiment described in Chapters 4 to 7. This includes a mountable laser system, a Peltier element based sample holder allowing rapid variation of the substrate temperature and an attachable polarisation resolved setup for optical spectroscopy.

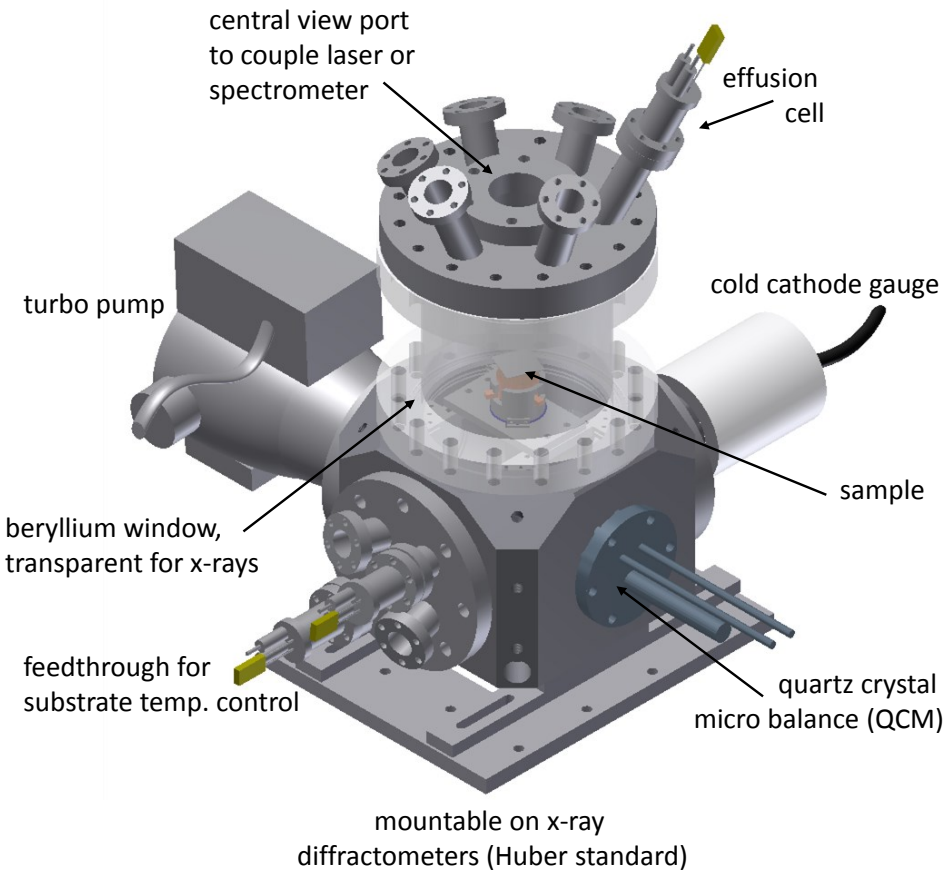

FIGURE 3.1: Compact OMBD growth chamber that can be used for *in situ* experiments at synchrotron diffraction beamlines. It is equipped with a 360° beryllium window, so that in-plane and out-of-plane x-ray experiments can be performed. The top flange allows attaching setups for optical spectroscopy or laser light sources normal to the sample surface.

3.2. Surface Diffraction Beamlines at Synchrotron Light Sources

The x-ray scattering results presented in this dissertation have mainly been collected at surface diffraction beamlines at the four synchrotron light sources ESRF (European Synchrotron Radiation Facility; Grenoble, France), Diamond (Didcot, United Kingdom), SLS (Swiss Light Source, Paul Scherrer Institute; Villingen, Switzerland) and PETRA III (Desy, Deutsche Elektronen-Synchrotron, Hamburg; Germany). The beamlines ID03[77], ID10[78] (both at ESRF), I07 (Diamond)[79] MS (SLS)[80] and P03 / MiNaXS (PETRA III)[81] are all undulator equipped and thus enable investigations even of weakly scattering samples. In the following, a brief description of x-ray generation at synchrotron light sources as well as the experimental setup at a surface diffraction beamline is given.

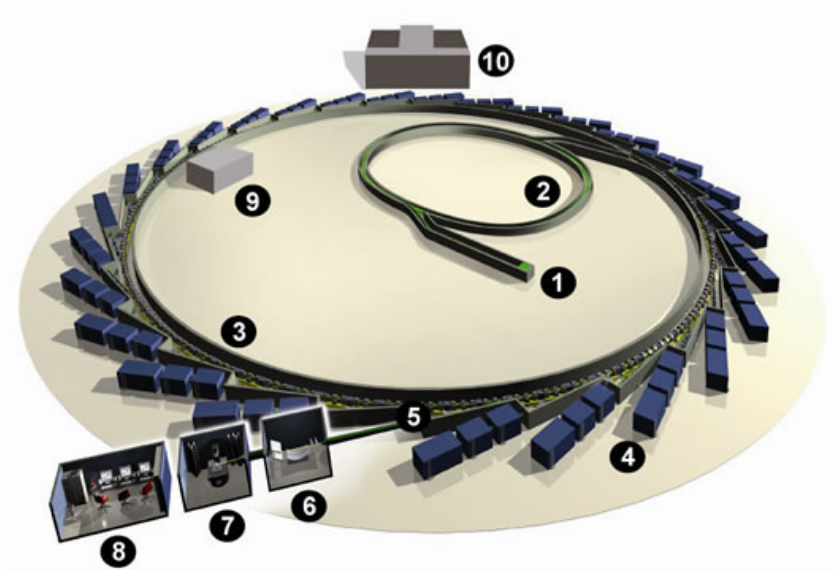

FIGURE 3.2: Illustration of a synchrotron machine. (1)Linac; (2) Booster synchrotron; (3) Storage ring; (4) Beamline; (5) Front-end; (6) Optics Hutch; (7) Experimental Hutch; (8) Beamline control Cabin; (9) Radiofrequency Cavity; (10) Accelerator control room. Reprint with permission.[1]

To generate extremely powerful and brilliant x-rays, 3rd generation[82] synchrotron sources (Figure 3.2) are widely used in today's material science. The radiation is produced by highly energetic electrons kept at constant (ultra-relativistic) energy in a storage ring. The electron beam is about 250μm wide and 16μm high (Diamond). Applied magnetic fields force the electrons to travel along a curved path. Whenever the electrons are accelerated radially, either to keep them on their closed path (with bending magnets), or when exposed to additional obstacles such as wigglers and undulators they emit so called synchrotron radiation (Figure 3.3). Modern diffraction beamlines as the ones mentioned

[1] Interior view of the Diamond synchrotron, Harwell Campus, Oxfordshire, UK, Diamond Light Source Ltd, 2016

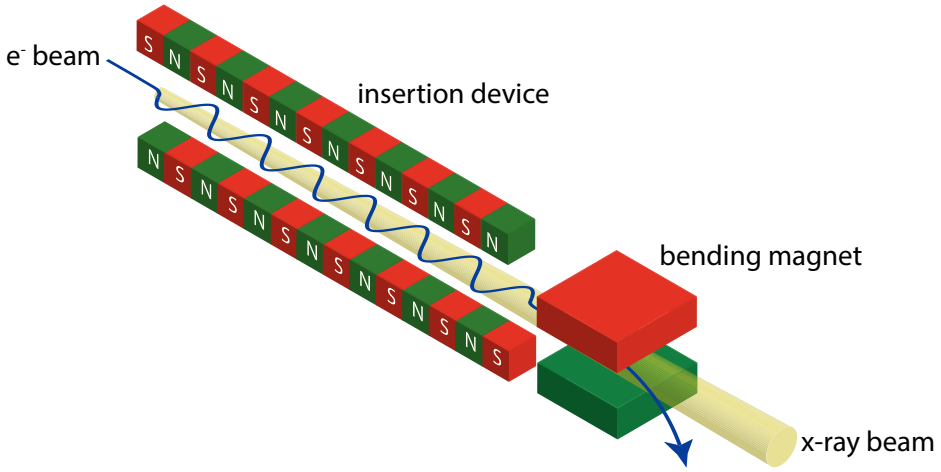

FIGURE 3.3: Insertion device for Synchrotron storage ring to produce intense x-ray radiation. Through altering magnetic fields electrons with an relativistic energy in the GeV range are accelerated perpendicular to the electron-beam direction and emit synchrotron radiation.

above use undulator insertion devices that consist of a series of dipole magnets arranged such that the generated radiation at each position in the undulator adds up in phase. Thereby, extremely high radiation intensities and small opening angles can be reached. The undulator spectrum can be regarded as quasi-monochromatic, consisting of one particular wavelength and its harmonics.[82] The generated radiation leaves the storage ring facilities tangentially at the so called front end ((5) in Figure 3.2) and enters the beamline.

Around the storage ring there are typically 30 to 50 research stations, so called beamlines. They are arranged in line with their associated insertion device or bending magnet. Each beam line consists of an optics hutch (6), an experimental hutch (7) and an control room (8) (Figure 3.2). In the optics hutch the beam is monochromatised and shaped according to the needs of the experiment. For the performed thin film diffraction experiments beam, dimensions in the order of $\simeq 50x150\mu m$ at the sample position have been used at energies between $10\,keV$ and $20\,keV$.

The most important components in the experimental hutch of a surface diffraction beamline are the x-ray detector and the diffractometer. Area detectors such as *Dectris Pilatus* or *MaxiPix* are used to spatially resolve the diffracted x-ray signal in an extended solid angle rather than at an single point.[83] The Diffractometer (Figure 3.4) consists of multiple rotation axes that all rotate around the same centre of rotation and allow to position the detector and the sample independently from each other. There are at least two degrees of freedom for both, detector and sample, to allow horizontal and vertical rotations independently from each other. To align the sample surface with respect to the centre of rotation and the incoming beam, there are 6 additional degrees of freedom provided through a hexapod. In figure Figure 3.4 the setup at the beamlines I07 (Diamond) and ID10 (ESRF)

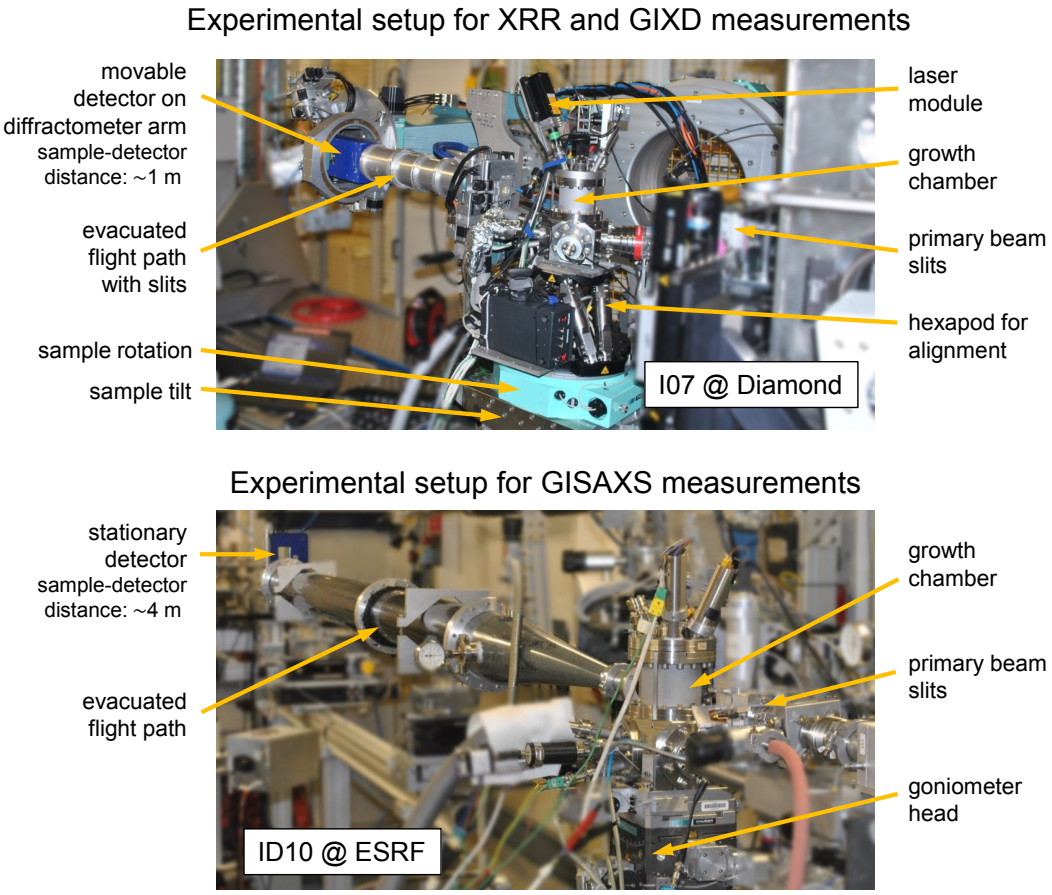

FIGURE 3.4: Experimental setups used in the framework of this thesis at I07 (Diamond) and ID10 (ESRF). A portable growth chamber is mounted on the beamline's diffractometer and the detector positioned according to the experimental needs of XRR and GIXD (top) or GISAXS (bottom). In the picture of I07 also the laser module used in Chapter 5 is shown.

are exemplary shown.

At I07 the OMBD growth chamber is mounted on the diffractometer and aligned using a hexapod. The detector is mounted on the diffractometer arm with roughly 1 m sample detector distance (SDD). The flight path between sample and detector is evacuated to minimise the background signal produced by air scattering. A pair of slits at the entry window of the flight path allows blocking of the scattering from entry and exit window of the growth chamber. An additional sample rotation stage underneath the hexapod (above sample tilt) is used for azimuthal scans. In this configuration x-ray reflectivity (XRR) and grazing incidence x-ray diffraction (GIXD) measurements are performed.

For grazing incidence small angle x-ray scattering (GISAXS) experiments the setup in the experimental hutch differs significantly and is shown in Figure 3.4 (bottom) as realised at ID10, ESRF. In order to resolve the small angle scattering signal, the SDD is increased to 4 m and only limited through the available space in the hutch. The instrumental resolution in this geometry is defined through the beam divergence and the detector pixel size. To

achieve large SDDs, the detector is not mounted on the diffractometer arm, but a stationary detector is used instead. A small entry window of the flight tube ensures suppression of signals that are due to parasitical scattering in the beryllium window of the vacuum chamber.

3.3. X-ray Scattering on Organic Thin Film Structures

X-ray scattering methods are especially suited to study thin film growth processes as they allow accessing a variety of thin film properties and enable non-invasive *in situ* and real time measurements. Acquirable are the layer structure through x-ray reflectivity (XRR) and anti-Bragg growth oscillations, island densities through small angle scattering and the crystal structure through in-plane and out-of-plane Bragg reflections. Since scattering techniques generally probe reciprocal space information complementary real space methods such as atomic force microscopy are an additional valuable tool to shine light on the real space arrangement.

3.3.1. The Momentum Transfer Vector q

Based on the wave vector for the ingoing x-ray beam $\mathbf{k}_i$ and the outgoing, scattered wave $\mathbf{k}_f$. Concidering elastic scattering $\left(|\mathbf{k}_i| = \left|\mathbf{k}_f\right| = |\mathbf{k}| = {}^{2\pi}/_{\lambda}\right)$ allows to formulate Bragg's law in the form

$$|\mathbf{q}| = 2\,|\mathbf{k}| \sin\frac{2\theta}{2} \tag{3.1}$$

with $\mathbf{q} \equiv \mathbf{k}_f - \mathbf{k}_i$ and 2θ being the experimental scattering angle. Therefore, a scattering experiment can be visualised as a map in momentum space, where $\mathbf{q}$ is the independent variable and the scattered intensity is the depended variable.[84] The momentum transfer is the fundamental variable used to present the results of a scattering experiment independent from the x-ray wavelength λ used in the experiment and is also used in scattering theory.[85]

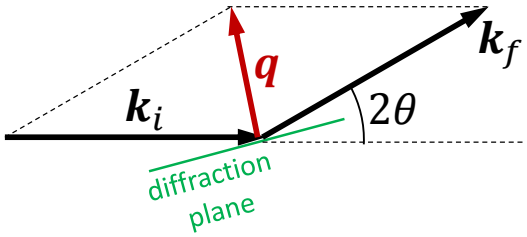

Figure 3.5: Construction of the momentum transfer vector $\mathbf{q}$.

In diffraction experiments there are two outstanding directions of $\mathbf{q}$: the one normal to the sample surface which we will label with q_z and the scattering in the surface plane denoted as $q_\parallel$.

3.3.2. Out-of-Plane Diffraction and X-Ray Reflectivity

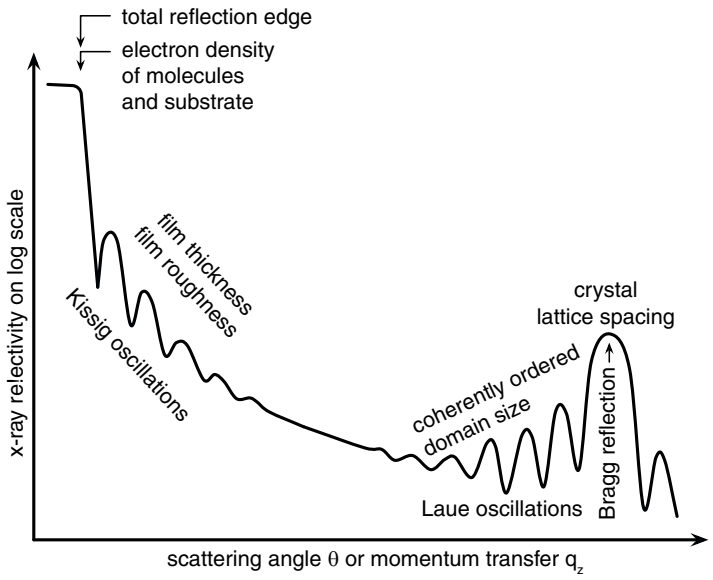

FIGURE 3.6: Diffraction features and their structural origin acquired in an x-ray reflectivity scan

A common approach to study the electron density profile in an organic thin film as well as the crystal structure normal to the substrate surface is to acquire the scattered intensity for **q** normal (out-of-plane) to the substrate surface. These measurements are called x-ray reflectivity (XRR) for $|\mathbf{q}|$ below $\sim 0.2\,\text{Å}^{-1}$ and out-of-plane, $\theta - 2\theta$ or q_z-scans for larger momentum transfer values. They require $\alpha_i = \alpha_f$ for incidence and exit angle with respect to the substrate surface.

The recorded Bragg reflections can be used to identify the contact plane of the molecular crystallites on the substrate surface. To extract the electron density profile, the *Parratt* algorithm can be applied to model the recorded scattering intensity over q_z through a box model.[86]

3.3.3. Anti-Bragg Growth Oscillations and Rate Equation Model

To study the out-of-plane morphology, namely the surface roughness and individual layer coverages, anti-Bragg growth oscillations have proven to be a useful tool.[29,49,51,62,71,84,87,88] The scattered intensity under the anti-Bragg condition defined by $q_z = {}^1\!/_2\, q_{\text{Bragg}}$ (illustrated in Figure 3.7) is given by

$$I(t) \quad = \quad \left| A_{\text{substrate}} \cdot e^{i\phi} + f_{\text{monolayer}} \sum_n \theta_n(t) \cdot e^{i d n \frac{1}{2} q_{\text{Bragg}}} \right|^2 \tag{3.2}$$

involving the following quantities:

- $A_{\text{substrate}}$, the substrate reflection amplitude,
- ϕ, phase constant (scattering phase between substrate and film),
- $f_{\text{monolayer}}$, structurefactor of a single molecular monolayer,
- $\theta_n(t)$, coverage of the n$^{\text{th}}$ monolayer,
- d, lattice spacing,
- q_{Bragg}, out-of-plane momentum transfer probing the lattice spacing d.

Compared to the scattered intensity under Bragg conditions (Figure 3.7 left) that increases quadratically with the thickness of the grown film, the anti-Bragg intensity oscillates with emerging film thickness. To fulfil the Bragg condition, $q_{\text{Bragg}} = \frac{4\pi}{d}$ is chosen such that two subsequent molecular monolayers (MLs) with the lattice spacing d scatter in phase.

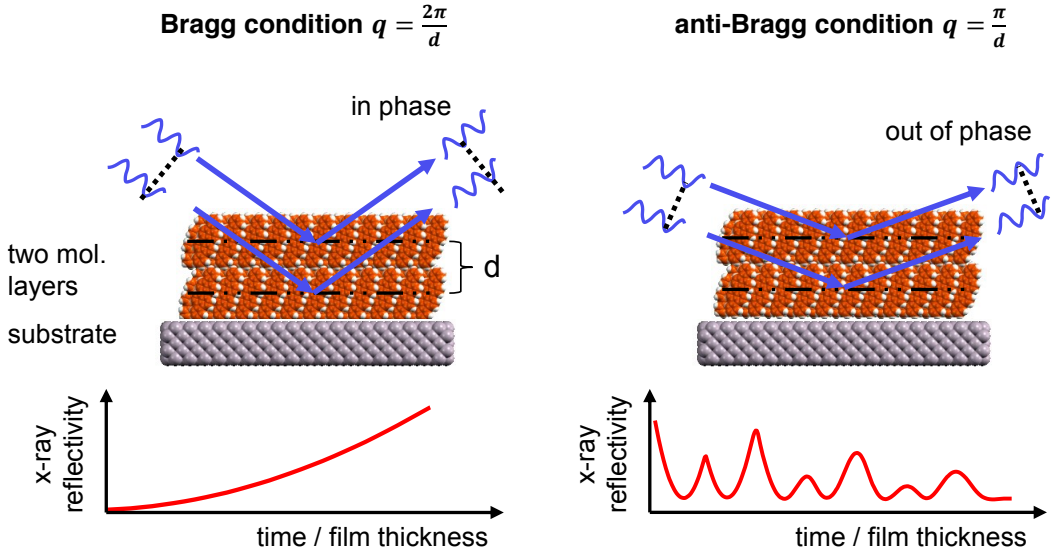

FIGURE 3.7: Sensing growth oscillations. Top: Under Bragg condition, x-rays are scattered in phase from two subsequent molecular monolayers of the distance d. In anti-Bragg condition twice the lattice spacing (half the q_z value, equivalently) is probed. Under this condition two subsequent monolayers just scatter out-of-phase. This results in high intensity for an even number of monolayers and low intensity for an odd number of monolayers in the sample, respectively. Bottom: Illustration of intensity evolution under Bragg and anti-Bragg condition over time. At constant growth rate, the Bragg intensity increases quadratically whereas the anti-Bragg intensity oscillates with an periodicity of two deposited molecular monolayers

Probing $\frac{1}{2}q_{\text{Bragg}}$ therefore leads to 180° phase shift between the scattered signal of two neighbouring MLs. This results in a scattering intensity that oscillates during thin film growth with a periodicity of typically two molecular ML, forming main and side maxima (schematic signal shown in Figure 3.7 right). Depending on ϕ, the local side maxima are more or less pronounced. Typically the surface roughness increases with film thickness,

hence, the coverage of several monolayers changes, at the same time causing a damping in the anti-Bragg signal.

Aiming to extract the individual layer coverages $\theta_n(t)$ from a recoded time series of anti-Bragg intensities during thin film growth, a set of rate equations can be used to model the growth process. The model developed by Trofimov[89,90] and Venables,[91] later silplified by Woll,[92] is based on the idea that beyond a critical layer coverage $\theta_{n,\mathrm{crit}}$ the subsequent layer starts to fill up even though the underlying one is not fully filled yet. The set of differential equations may be written as

$$\frac{d\theta_n}{dt} = R_n\left[\xi_{n-1} - \theta_n\right] + R_{n+1}\left[\theta_n - \xi_n\right] \tag{3.3}$$

$$\xi_n = \begin{cases} 1, & \text{if } n = 0 \\ 0, & \text{if } n \geq 1,\ \theta_n > \theta_{n,\mathrm{crit}} \\ 1 - e^{-\left(\sqrt{-ln(1-\theta_n)} - \sqrt{-ln(1-\theta_{n,\mathrm{crit}})}\right)^2}, & \text{otherwise} \end{cases} \tag{3.4}$$

with R_n being the deposition rates that may differ between the individual monolayers (MLs). Especially for the first ML (n=1) a distinct rate R_1 is often needed as the sticking coefficient[2] may differ for the growth on the bare substrate, compared to growth on previously deposited molecular layers.[29,93,94] ξ_n, the so-called *feeding zone*, describes the surface fraction of the n^{th} ML that contributes to the growth of the $(n+1)^{\mathrm{th}}$ ML. In the first layer $\xi_{n-1} = \xi_0 = 1$, thus, all molecules sticking on the bare substrate are used to fill up the 1^{st} ML. The term $[\xi_{n-1} - \theta_n]$ in Equation 3.3 describes the filled surface fraction of the $(n-1)^{\mathrm{th}}$ layer that is exposed to incoming molecules and thus, these molecules contribute to the growth of the n^{th} layer. The term $[\theta_n - \xi_n]$ describes the covered surface fraction of the n^{th} ML but still contributes to the growth of the n^{th} ML instead of the $(n+1)^{\mathrm{th}}$ ML. Thus, it expresses the interlayer transport (cf.[88]). The described processes are illustrated in Figure 3.8a.

The size of the feeding zone $\xi_n(t)$ is defined through the current coverage $\theta_n(t)$ and the critical layer coverage $\theta_{n,\mathrm{crit}}$. $\xi_n(t)$ is a normalised quantity, initially 0 and increases with coverage of layer n. It describes the fraction of the surface that is contributing to the nucleation and growth of the layer $n+1$.

In Figure 3.8b typical scenarios of layer filling over film thickness are shown. In the first case (solid lines) the individual layers fill up consecutively, meaning that the underlying layer fills almost completely before the subsequent one starts to grow. In the model this behaviour is captured through values of $\theta_{n,\mathrm{crit}}$ close to unity. In situations where layer-by-layer growth is less pronounced (dashed lines, smaller $\theta_{n,\mathrm{crit}}$), subsequent layers start to fill up even though the underlying one is not fully filled yet.
Based on the layer coverages, a total coverage $C_{\mathrm{tot}}(t) = C_\infty(t)$ and a RMS surface roughness

[2] share of modules in the vapour phase above the sample surface that integrate into the solid state film

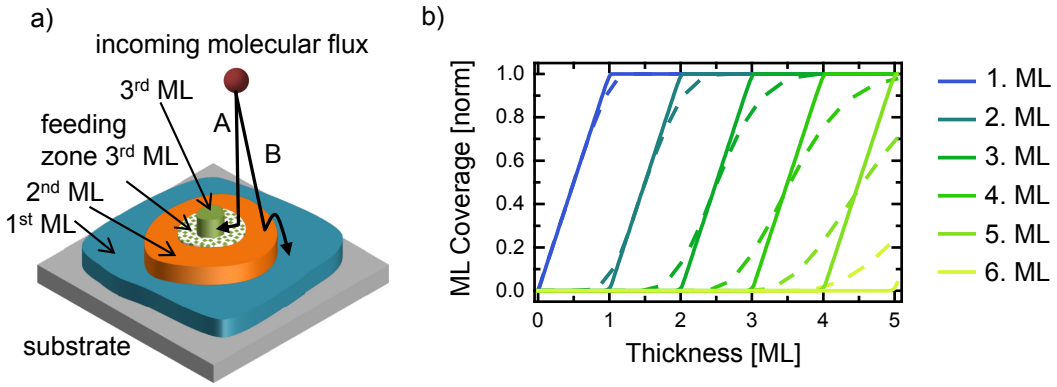

FIGURE 3.8: a) Visualisation of processes captured in the rate equation model. b) Prototypical evolution of individual layer coverages over time. Solid line: layer-by-layer growth; dashed line: subsequent monolayers start to nucleate before the preceding ones are fully filled.

$\sigma(t)$ can be defined by:

$$C_{\text{tot}} := \sum_{i=1}^{\infty} \theta_i \,, \tag{3.5}$$

$$\sigma = \sqrt{\sum_{i=1}^{\infty} (\theta_i - \theta_{i+1}) \, (i - C_{\text{tot}})^2} \,, \tag{3.6}$$

as established in [92].

3.3.4. In-Plane Diffraction: Grazing Incidence Diffraction (GIXD)

While the scattering methods discussed above describe the out-of-plane structure along q_z, grazing incidence diffraction that is described in the following is used to probe the in-plane sample structure probing $q_\parallel$.

At incidence angles below the critical angle $\alpha_i < \alpha_c$, x-rays undergo total external reflection and an evanescent wave that propagates parallel to the sample surface is formed. It does not penetrate the sample deeply as the corresponding electrical field E decays exponentially over the sample depth z

$$E = e^{ikz\sqrt{\alpha_i^2 - \alpha_c^2}} = e^{-z/\Lambda} \tag{3.7}$$

with an penetration depth Λ that typically lies in the range of few *nm*.[82] Therefore, GIXD is a very surface sensitive technique and allows to probe the *in-plane* structure of organic thin films on inorganic substrates.[95,96]

Even if the crystallites in a polycrystalline organic thin film all have a common contact plane with the substrate (i.e. the *ab*-plane for most planar molecules), their azimuthal orientation may still be statistically distributed (Figure 3.9a). This structure, also known as 2d powder, is predominantly found in organic thin films grown on amorphous substrates

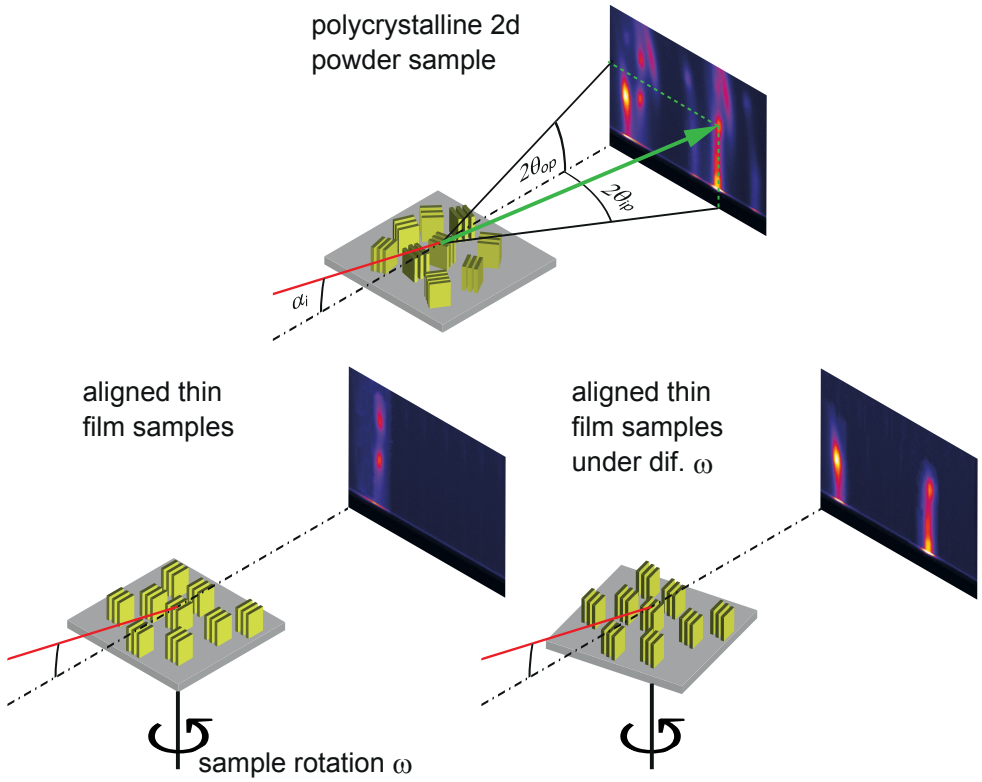

FIGURE 3.9: Grazing incidence diffraction pattern arising from a 2d powder sample (top) and aligned thin films (bottom). The diffraction pattern of the 2d powder sample is independent of the azimuthal sample orientation ω, whereas the diffraction pattern of the aligned thin film strongly depends on ω.

and in material systems where no epitaxial relation between substrate crystal structure and crystalline thin film is formed. Through the random orientation of the molecular in-plane unit cell, all Bragg reflections appear on the detector, regardless of the azimuthal sample orientation.

In contrast, it is also possible that the crystallites are azimuthally aligned along a preferential direction induced e.g. by the underlying substrate (i.e. epitaxial growth) or as in Chapter 5 through external light fields during growth. For these samples, the diffraction pattern observed on the detector strongly depends on the azimuthal sample orientation (illustrated in Figure 3.9b and c). This is due to the fact that the diffraction condition for a given Bragg reflection is only fulfilled under a certain azimuthal sample position. Diffraction experiments on this type of samples are further discussed in Section 3.3.5.

3.3.5. X-Ray Experiments to Study Azimuthally Aligned Thin Films

As mentioned in Section 3.3.4, GIXD is commonly used to study the in-plane structure of organic thin films, thus it is a versatile tool to study azimuthal alignment in organic thin films. There are two differing, widespread use cases of GIXD: 1) polycrystalline thin films without azimuthal texture, also known as 2d Powder [88,97,98] and 2) epitaxially grown thin films on single crystalline substrates where a fixed angular relation between GIXD reflections of the thin film and the substrate is studied. [25,99] In the experiment presented in Chapter 5 we will focus on azimuthal alignment of organic thin films on *amorphous* substrates so that the underlying material does not impose the azimuthal alignment of the organic film. Here we will discuss briefly how azimuthal scans acquiring GIXD intensities can be used to study the orientation of real space unit cell axes and the biaxial texture in thin films.

By definition there is a fixed relation between the orientation of direct (**a**,**b**,**c**) and reciprocal (**a***,**b***,**c***) lattice vectors [82]:

$$\mathbf{a}^* = 2\pi \frac{\mathbf{b} \times \mathbf{c}}{\mathbf{a} \cdot (\mathbf{b} \times \mathbf{c})} \quad \mathbf{b}^* = 2\pi \frac{\mathbf{c} \times \mathbf{a}}{\mathbf{a} \cdot (\mathbf{b} \times \mathbf{c})} \quad \mathbf{c}^* = 2\pi \frac{\mathbf{a} \times \mathbf{b}}{\mathbf{a} \cdot (\mathbf{b} \times \mathbf{c})} \tag{3.8}$$

In single crystal diffraction this allows one to define the orientation matrix that is used in diffraction experiments to relate the unit cell axis of a crystal in real space and the observed Bragg reflection. [100] Knowledge of this orientation matrix enables e.g. hkl-scans in surface diffraction experiments (e.g. [99,101]) of single crystalline surfaces. Aligned thin films are from an x-ray perspective, half way in between uniaxial textured 2d powder (with random azimuthal orientations of the individual crystal grains) and single crystal in terms of their diffraction behaviour. As they are polycrystalline samples, diffraction experiments of these structures are ensemble averages on a huge set of crystallites. Samples that consist of a multitude of crystal orientations with peaked azimuthal distribution, therefore, require a specific treatment. This is especially true in cases where no crystallographic relation to other (e.g. substrate) reflections are measured and where interest lies on the real space alignment of the thin film unit cell to correlate the crystal orientation with external stimuli (Chapter 5). The method presented in the following requires knowledge of the crystal structure (unit cell parameters) of the film and the contact plane with the substrate. In case there are unknown crystal structures in the sample, they have to be resolved by a crystal structure determination method before. [102,103] Additionally, the contact plane between the organic crystal and the substrate surface can be determined by XRR.

Based on the 2d *Ewald construction* [100] in the diffraction plane we can construct **q** (Section 3.3.1) in a way that the diffraction condition is fulfilled for a specific Bragg reflection (Figure 3.10a). In the illustrations we exemplarily treat the (022) reflection of the tetracene crystal. To probe a specific reflection according to a given momentum transfer vector **q** there is a set of orientations for the ingoing and outgoing beam that fulfil the diffraction condition. They all lie in a cone normal to the set of lattice planes that are probed. As

we assume a well-defined contact plane between substrate and molecular crystal, a certain realisation of $\mathbf{k}_i$ and $\mathbf{k}_f$ fulfilling the diffraction condition can be identified by the incidence angle α_i of the incoming beam (visualised in Figure 3.10b). For the α_i chosen in the experiment, this defines $q_{\parallel}$ and q_z in the laboratory reference frame under which the reflection occurs. To experimentally identify the preferred azimuthal crystal orientation in the sample it can be rotated around the sample surface normal (z in Figure 3.10c) while recording the diffraction intensity at the fixed detector position. For samples consisting of aligned crystallites there are well defined intensity maxima under certain azimuthal sample positions. For these sample orientations, where the diffraction condition is fulfilled, we are able determine the orientation of real space unit cell axes in the laboratory reference frame through Equation 3.8 as illustrated in Figure 3.10c.

In order to perform these measurements, very precise alignment of the sample is needed to avoid possible precession errors in azimuthal scans that strongly influence the acquired intensities as they influence the exact q_z, $q_{\parallel}$ position of the monitored reflection. Additionally, the incidence angle should be chosen large enough so that the footprint[104] is smaller than the sample for any azimuthal substrate orientation to ensure that the geometrical shape of the substrate does not influence the measured intensity.

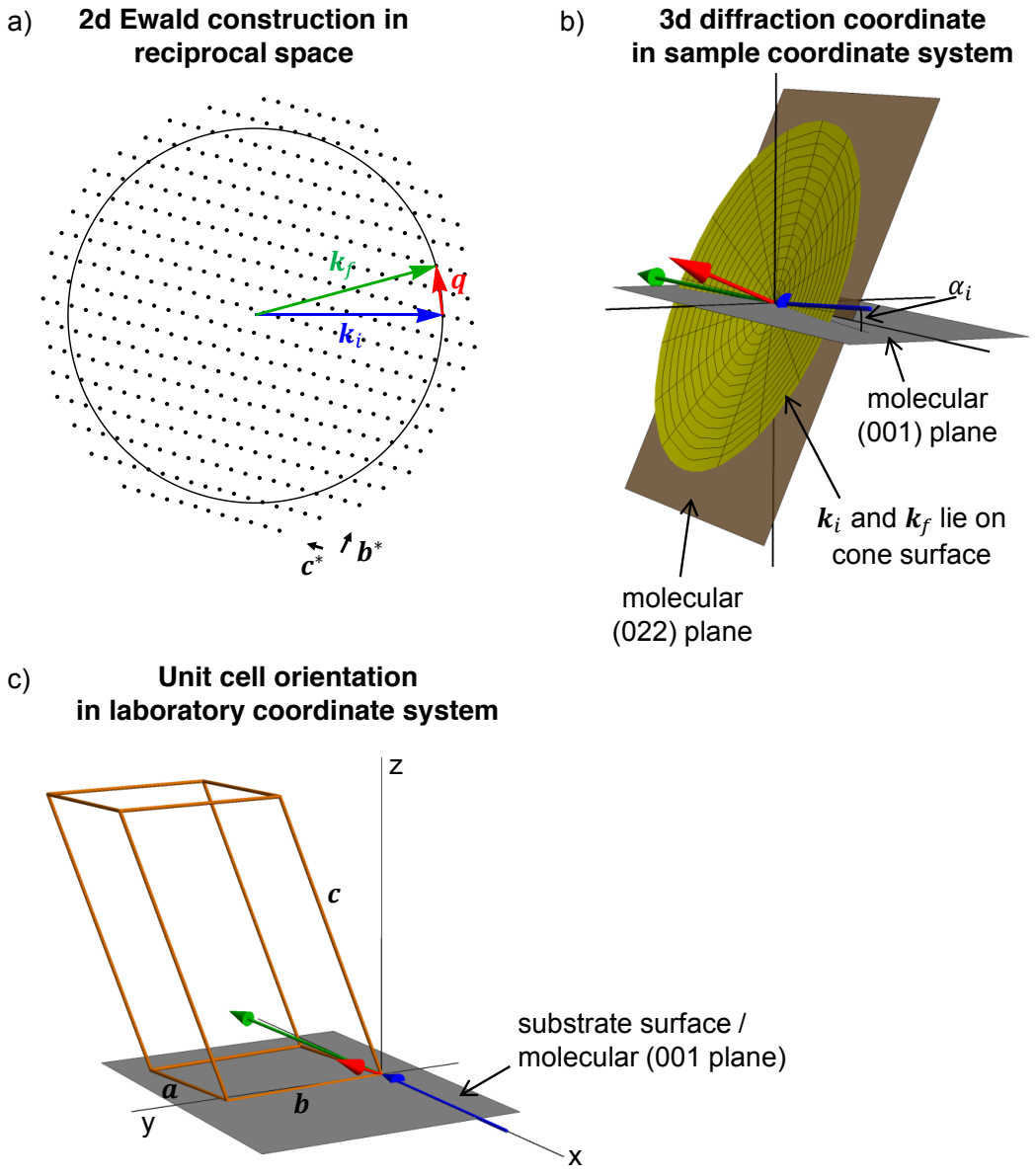

FIGURE 3.10: Determination of real-space unit cell orientation illustrated for tetracene (022) reflection: a)2d Ewald construction for $|\mathbf{k}| = 1.05\,\text{Å}^{-1}$ (as in experiment in Chapter 5); b) The diffraction condition can be fulfilled for all $\mathbf{k}_i$ lying on the cone surface. For a given α_i in the experiment there is only one orientation of $\mathbf{k}_i$ that meets the diffraction condition and thereby defines the detector position in order to probe $\mathbf{q}_{(022)}$. c) Through the fixed relation between direct and reciprocal unit cell the real space orientation of the unit cell in the laboratory reference framework is determined.

3.3.6. Grazing Incidence Small Angle X-Ray Scattering (GISAXS)

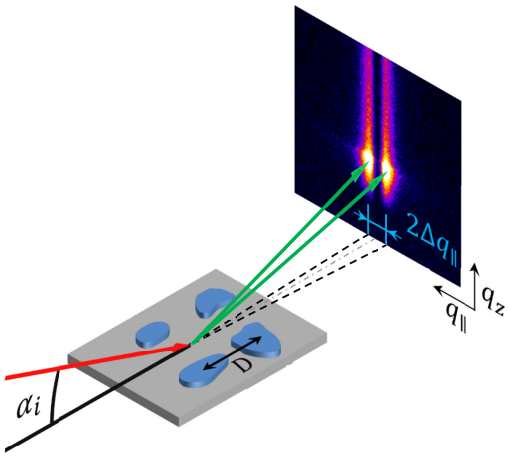

FIGURE 3.11: Schematic illustration of a grazing incidence small angle x-ray scattering (GISAXS) experiment. The island density in the sample correlates with the $q_{\parallel}$ splitting on the detector.

Similar to GIXD, grazing incidence small angle x-ray scattering (GISAXS) is a very surface sensitive technique.[105] When increasing the sample-detector-distance to several meters, for very small $q_{\parallel}$ values a peak splitting arising from structures of sizes ranging from few *nm* to several 100 *nm* can be observed.[81] Thus, this diffusively scattered signal is not attributed to the crystal structure of a sample but rather to larger objects on the sample surface. In organic thin film growth, this length scale corresponds to the distance between individual molecular islands (crystal grains) that are formed during thin film growth (Figure 3.11).[29,106] In kinematic, single scattering approximation, the scattering signal can be considered as the Fourier transform of the real space sample surface. Thus, the distance between the molecular islands D is related to the $q_{\parallel}$-splitting of $2\Delta q_{\parallel}$ via the relation

$$D \simeq \frac{2\pi}{\Delta q_{\parallel}}. \tag{3.9}$$

Modern, dedicated programmes like BornAgain[107], IsGisaxs[108] or FitGISAXS[109] use multiple scattering approximations like the distorted Born wave approximation to model GISAXS results in order to extract structural parameters such as the island diameter and inter-island distance separately. In the framework of this thesis, the simple approximation in Equation 3.9 is used in order to evaluate the island distance and therefore also the island density over time while the organic thin film is growing. Assuming a dense (hexagonal) packing,[29] the molecular island density can be calculated from

$$N = \frac{2}{\sqrt{3}} \frac{1}{D^2}. \tag{3.10}$$

From an instrumentational perspective, GISAXS is a demanding scattering technique as it requires very small x-ray beams with extremely low divergence and large sample detector

distances in order to allow resolving signals with less than 0.1 *mrad* angular separation. GISAXS experiments performed in the framework of this thesis were all carried out at the ESRF ID10 beamline (see Figure 3.4).

3.3.7. Time Resolved *In Situ* Studies Combining In-Plane and Out-of-Plane Sensitivity

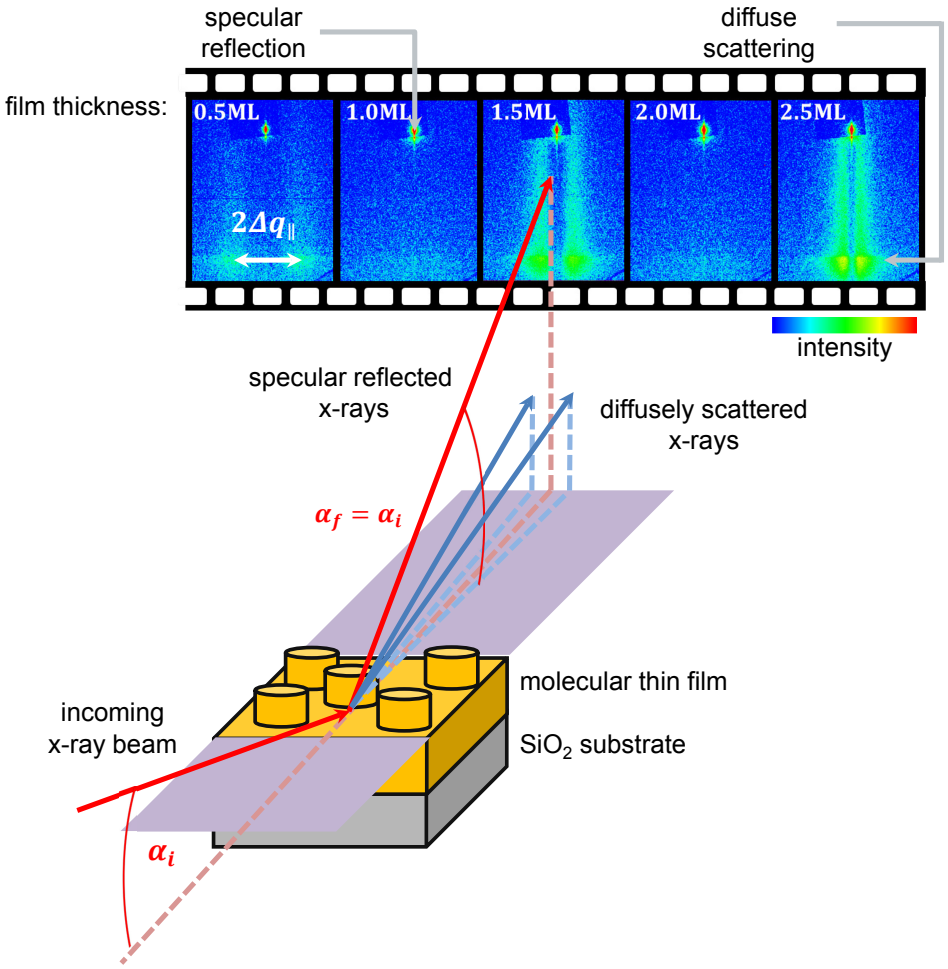

FIGURE 3.12: Scattering geometry to acquire anti-Bragg intensity and GISAXS simultaneously on an area detector in a real-time thin film growth experiment. The incidence angle α_i is chosen such that it matches the anti-Bragg condition and island density is extracted from the diffusely scattered signal in the yoneda region. The intensity of the diffusely scattered signal oscillates with the film thickness of the growing film. Whenever a layer closes, this signal vanishes due to the smooth surface (no surface islands to scatter on). Cf.[110]

To follow the structural evolution of a molecular thin film growth process in real time, it is beneficial to acquire both individual layer coverages (out-of-plane structure) and island densities (in-plane structure). As discussed, anti-Bragg growth oscillations allow one to follow the out-of-plane structure evolution over time, whereas the diffusively scattered GISAXS signal provides insights on the in-plane structure. Both scattering techniques can be combined into a single diffraction experiment using a 2d area detector. The scattering geometry is illustrated in Figure 3.12 where the incidence angle α_i of the incoming beam is increased well above the critical angle to fulfil the anti-Bragg condition. The intensity

of the specular reflected signal thus gives rise to anti-Bragg oscillations during thin film growth. At the same time the diffusively scattered signal (especially intense in the yoneda region) showes a $q_{\|}$-splitting and thus allows concluding on the characteristic island spacing in the growing molecular thin film in real time. This combined scattering geometry was used in previous studies.[29,102,106,111]

3.3.8. Quantitative Phase Analysis as used in Rietveld Method

In order to study the coexistence of different polymorphs in a single sample and to quantify the phase-content of the individual species in the sample, the Rietveld method is widely used.[112,113] Here we present a modified approach in order to be able to use the intensity of of XRR reflections in thin film samples to conclude on the phase content of two polymorphs in a sample.

In terms of the Rietveld method, the integrated intensity of a reflection is given by

$$I_{\mathrm{hkl}} = S\, m_{\mathrm{hkl}}\, (LP)_{\mathrm{hkl}}\, F^2_{\mathrm{hkl}} \tag{3.11}$$

where S is the scale factor, m_{hkl} the multiplicity, $(LP)_{\mathrm{hkl}}$ the Lorentz-polarisation factor and F_{hkl} the structure factor.[112] In samples that consist of phase mixtures, the scale factor S can be expressed in terms of m_{p} the mass of phase p present in the sample. This involves the number of molecules (formula units) per unit cell Z_p, the mass of one molecule M_p and the unit cell volume V_p. S is given by

$$S = \frac{m_p}{Z_p\, \mathrm{M}_p\, V_p}\mathrm{C} \tag{3.12}$$

with $C = \frac{\Phi_0\, \lambda^3 \mathrm{h\, w\, t}}{8\, \pi\, r^2}$ bundling the experimental quantities primary x-ray flux Φ_0 , wavelength λ, r specimen-to-detector distance and h, w, t the aperture height, width and counting time.[113]

The intensity ratio between two peaks of two phases A and B can be written as

$$\frac{I_{(hkl)_A}}{I_{(hkl)_B}} = \frac{m_{(hkl)_A}\, (LP)_{(hkl)_A}\, F^2_{(hkl)_A}}{m_{(hkl)_B}\, (LP)_{(hkl)_B}\, F^2_{(hkl)_B}}\, \frac{m_A}{m_B}\, \frac{Z_B\, \mathrm{M}_B\, V_B}{Z_A\, \mathrm{M}_A\, V_A}. \tag{3.13}$$

Assuming the two crystal phases A and B are crystal polymorphs, involving the same formula unit (molecular species), we can write $\mathrm{M}_A = \mathrm{M}_B$. Only considering reflections with the same multiplicity, we have $m_{(hkl)_A} = m_{(hkl)_B}$. Further restriction to reflections that appear in close proximity leads to the approximation $LP_{(hkl)_A} = LP_{(hkl)_B}$. From this we can deduce for the mass ratio $\frac{m_A}{m_B}$ of the two phases

$$\frac{m_A}{m_B} = \frac{F^2_{(hkl)_A}}{F^2_{(hkl)_B}}\, \frac{Z_B\, V_B}{Z_A\, V_A}\, \frac{I_{(hkl)_A}}{I_{(hkl)_B}}. \tag{3.14}$$

This allows us to determine the mass ratio of two polymorphs in a sample based on measured Bragg reflection intensities.

3.4. UV Vis Spectroscopy

Not only x-ray methods but also optical spectroscopy can be used to analyse the structure of molecular thin film systems *in situ* and in real-time.[62] Furthermore ultra-violet and visible light (UV Vis) spectroscopy is especially suited to study characteristics of organic semiconductors as their HOMO-LUMO gap typically lies in the energy range of 1 eV to 4 eV. Polarised spectroscopy additionally allows for probing anisotropy in thin films.

3.4.1. Luminescence Spectroscopy

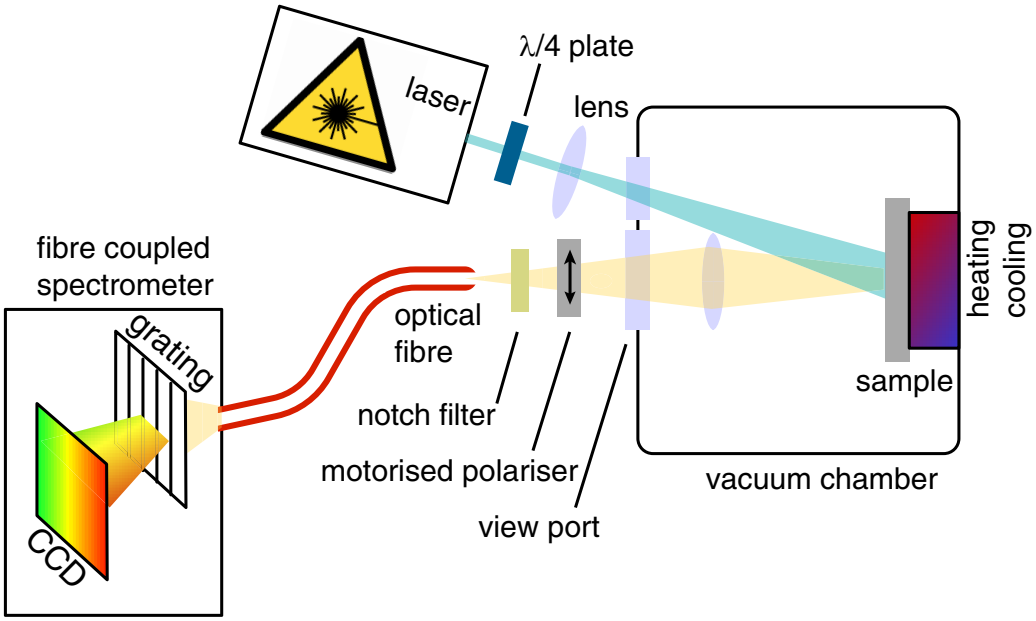

Figure 3.13: Fibre coupled grating spectrometer used to sense light emitted by the sample. The exciting laser is depolarised to ensure homogeneous excitation of all molecules regardless of their azimuthal orientation in the sample. Through the motorised polariser the polarisation of the luminescence signal is probed. The notch-filter matching the laser wavelength ensures that the spectrometer does not saturate due to the intense excitation signal.[3]

For this study, a fibre coupled spectrometer as shown in Figure 3.13 has been used to measure polarisation resolved luminescence spectra. The sample is excited via an external light source outside the growth chamber. Here circular polarised light of a 450 nm laser with variable optical output power (up to 1 $W\,cm^{-2}$) or unpolarised, focused LED light sources are used to excite the sample. The light emitted by the sample is collected via a lens setup and sent through a motorised polariser before it is collected by the fibre and transferred into the grating spectrometer (*Andor / Acton 2150i*). Since it is only possible to observe spectral features of the sample with energies below the exciting laser energy, a notch filter or even a simple longpass filter can be used to separate the diffusely scattered exciting laser line from the emission spectra. The polariser allows one to sense optical

anisotropies in the luminescence signal. Since all in-plane orientations of molecular transition dipole moments are excited equally, changing signal intensities for varying polariser orientations indicate polarised luminescence of the sample.

3.4.2. Differential Reflectance Spectroscopy

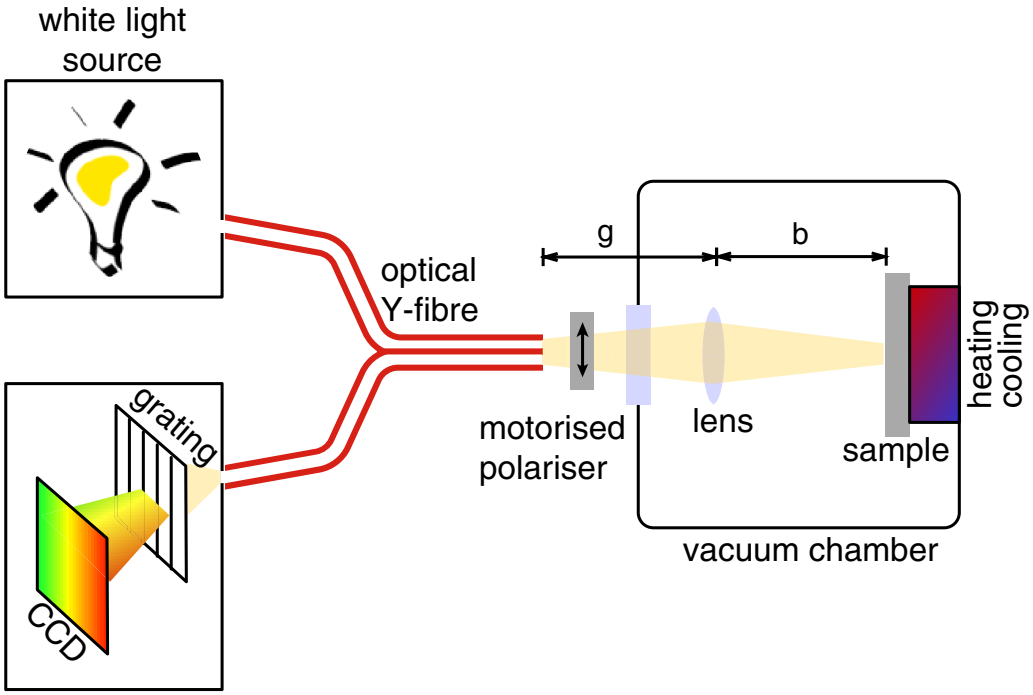

Figure 3.14: Setup for Differential Reflectance Spectroscopy (DRS). Using an optical Y-fibre, an unpolarised white light beam is transferred to the setup. Through the polariser a linearly polarised fraction of the incoming white light is used to illuminate the sample. The reflected spectrum (same polarisation as the incoming light) is recorded on a fibre coupled spectrometer.

Due to the confined geometry in the growth chamber (Figure 3.1) and the use of intransparent substrates (Si wafer with native oxide), a direct measurement of the light transmitted through the sample is often not possible. In these cases the setup shown in Figure 3.14 has been used to approximate the absorption properties of organic thin films by measuring the reflectance of a layered system. In contrast to the setup described in the previous paragraph, where the sample is exposed to monochromatic light, in this setup the sample is exposed to white light. A fibre coupled grating spectrograph equipped with a CCD detector is used to measure the whole spectrum at once.

Following Forker *et al.*[114] the Differential Reflectance Spectroscopy (*DRS*) signal which

[3]Depending on the laser wavelength used and the availability of a matching notch filter, the grating in the spectrometer may alternatively be displaced such that only energies well below the exciting energy are recorded.

is defined as

$$DRS(E,d) \quad = \quad \frac{R(E,d) - R(E,0)}{R(E,0)}. \tag{3.15}$$

$R(E,0)$ represents the bare substrate reflectivity at an energy E and $R(E,d)$ the reflectivity of the layer system consisting of the substrate and a thin film of the thickness d on top. As the *DRS* signal is a relative quantity, the absolute intensities cancel out each other and only intensity fluctuations influence the signal[115]. Knowing the substrate's optical constants, the absorption of the thin film can be derived by using the *Kramers-Kronig* relation in an optical transfer matrix method.[114] In case the thin film thickness being much smaller than the wavelength ($d \ll \lambda$), the *DRS* signal can be approximated by

$$DRS \quad \simeq \quad -\frac{8\pi d}{\lambda}[\overbrace{A \cdot \epsilon_{2,\mathrm{film}}}^{①} + \overbrace{B \cdot (\epsilon_{1,\mathrm{film}} - 1)}^{②}] \tag{3.16}$$

$$A \quad = \quad \frac{1 - \epsilon_{1,\mathrm{sub}}}{(1 - \epsilon_{1,\mathrm{sub}})^2 + \epsilon_{2,\mathrm{sub}}^2} \tag{3.17}$$

$$B \quad = \quad \frac{\epsilon_{2,\mathrm{sub}}}{(1 - \epsilon_{1,\mathrm{sub}})^2 + \epsilon_{2,\mathrm{sub}}^2} \tag{3.18}$$

as shown by McIntyre and Aspnes.[116] Here, the dielectric function is written as $\epsilon = \epsilon_1 + i\epsilon_2$. DRS can be used to determine the thin film absorption $\epsilon_{2,\mathrm{film}}$, if term ② is negligible compared to term ①. Under this condition the DRS further simplifies to

$$DRS \quad \simeq \quad -\frac{8\pi dA}{\lambda} \cdot \epsilon_{2,\mathrm{film}}. \tag{3.19}$$

Since we use DRS to reveal anisotropy in the optical properties of organic thin films, a polariser is added in between the fibre and the sample to probe the sample with linearly polarised light. As the DRS is measured under normal incidence, only the portion of the reflected light which has the same polarisation direction as the incoming light is guided into the spectrometer.

3.4.3. Absorption Spectroscopy

Samples on transparent substrates (float glass, quartz or KCl) can be analysed by absorption spectroscopy. While in DRS $\epsilon_{2,\mathrm{film}}$ is measured indirectly in the reflected signal, transmission spectroscopy directly allows to extract the thin film absorbance and is a handy tool for post-growth analysis. Transmission spectra of grown films have been recorded with a *Perkin Elmer LAMBDA 900* spectrometer in the framework of this thesis. In this dual beam setup, the sample is exposed to monochromatic light and the transmittance compared to a reference sample (bare substrate without film) is measured. The incoming intensity is divided into the three portions transmitted T, absorbed A and reflected R beam through the sample (not considering diffuse scattering). Conceptually, this reads

as $1 = T + A + R$ for normalised incidence intensity. Thus, measuring the transmittance at a given wavelength allows one to determine the absorption A at the same wavelength when considering the reflectance R of the sample as negligible. Scanning the energy of the incoming beam through the whole UV-Vis range reveals the full absorption spectrum.

3.5. Atomic Force Microscopy

The atomic force microscope (AFM) was introduced in 1986 by Binnig, Quate and Gerber allows probing surface morphologies on atomic-scale with only few limitations on the studied sample.[118] Other than in far field techniques such as conventional optical microscopy that are limited in resolution to length scales in the order of the used wavelength, scanning microscopic techniques allow for a much higher spatial resolution. Since AFM does not require an electrically conductive surface, in contrast to scanning tunnelling microscopy (STM), it is a very suitable tool to analyse organic thin film structures on varying substrates as done in the context of this thesis.

The basic working principle[119] relies on the detection of a minimal deflection of a cantilever according to *Hook's law*. The cantilever is equipped with a sharp tip that is placed in close vicinity of the sample surface (Figure 3.15). Typically, the deflection is detected through the electrical signal of a four-segment photo diode arising from the displacement of a laser beam reflected on the cantilever.[120] In vicinity of the sample surface, the tip may either experience attractive or repulsive interactions. The so called *force-distance-curve* is commonly governed by far ranging van der Waals interactions (attractive) and repulsive Coulomb interactions (Figure 3.16a). A piezo scanner is used to trace the tip across the sample.

Below the typical operation modes of an AFM are listed:[121]

- **Contact mode**
  The tip is positioned in 'physical contact' with the sample, so that the cantilever pushes down on the tip. As the tip is moved across the sample, the cantilever bends according to topographical changes on the sample surface. In case the cantilever

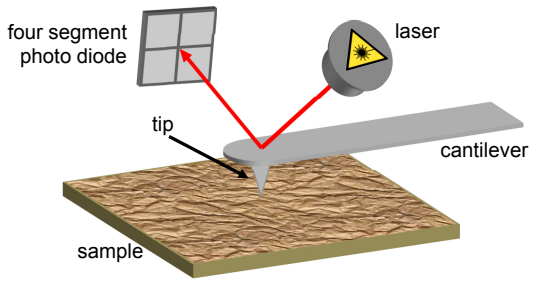

Figure 3.15: Experimental core of an AFM: The cantilever with tip is deflected when approaching the surface. The deflection is recorded through monitoring the position of a reflected laser beam on a four-segment photo diode. Cf. [117]

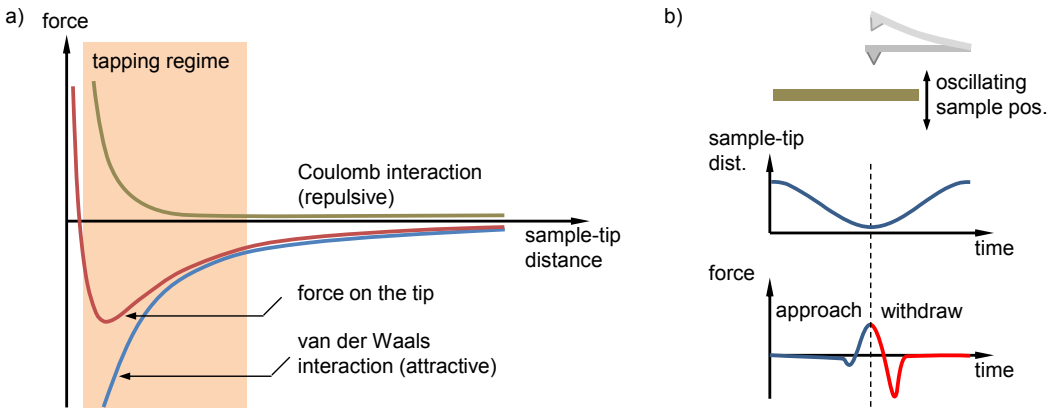

FIGURE 3.16: a) Force on the AFM-tip induced by the sample surface. b) Illustration of Peak Force Tapping Mode as e.g. implemented in *Bruker ScanAsyst*. At each xy-position the sample oscillates in z and at each position a force distance curve is acquired. Cf.[117]

is kept at a *constant height*, the deflection signal can directly serve as topographic signal. This method only works for very flat samples, therefore, it is often beneficial to rather apply a *constant force* on the cantilever and regulate its height accordingly by a feedback cycle. In this case, the height can be taken as topography signal.
The contact mode is rather limited to 'hard' samples and not often used to study soft matter thin films as binding forces in organic materials are mostly too weak to withstand the pressure applied trough the tip without damage.

- **Non-contact mode**
  Lifting up the tip away from the surface, only long range interactions remain to deflect the cantilever. In this region of the force-distance curve (Figure 3.16), van der Waals interactions play the dominant roll. The cantilever experiences a deflection with opposing sign, compared to contact mode.
  In this dynamic mode, the cantilever is sinusoidally excited by an additional piezo and can therefore be described as a driven harmonic oscillator. The cantilever is excited at or close to its resonance. In proximity to the sample surface the height of the cantilever is regulated such that either the frequency or the oscillation amplitude are kept constant. Both quantities are sensitive to probe-sample interactions. For instance, attractive forces between tip and sample result in a decrease of the resonance frequency. Due to the increased sample-probe distance and the long ranging forces involved, the resolution in this mode is significantly lower than in the contact mode. It allows, however, to work with much softer samples.

- **Tapping mode**
  The tapping mode, also known as intermittent mode, combines the higher resolution of the contact mode with the gentleness of the non-contact mode. Especially under ambient conditions where a thin wetting film of water covers both probe and sample, the non-contact mode does often reveal the surface topography of the wetting layer rather than the actual sample surface.

In the tapping mode, the cantilever is also dynamically excited, but compared to non-contact AFM with a much higher amplitude. Frequency and amplitude of the driving force are kept constant. The height is regulated such that the cantilever amplitude is kept at a certain level below its free air amplitude. During each cycle, the tip is in 'contact' with the sample shortly and thus the spatial resolution in this mode is rather similar to that in contact mode. As the tip is not constantly dragged across the sample surface but rather lifted and repositioned during each cycle, the lateral forces of the tip on the sample are significantly reduced and also soft, organic films can be examined without tremendous damage.

- **Peak force tapping**
  Modern AFM controllers additionally allow for a so called peak force tapping mode as described, e.g., in ref. [117]. Instead of driving the tip in resonance, significantly lower frequencies are used to modulate the distance between sample and tip. In some instruments the sample rather than the cantilever is oscillating in z (Figure 3.16b). This procedure avoids filtering effects and having to deal with the dynamics of a resonating system. At each xy-position a force distance curve is acquired. Thus, a height profile according to a certain, directly controllable force can be extracted to image the topography of the sample. Optimised real-time feedback cycles in the controller ensure a user-friendly handling of the instrument in this mode.

The AFM data presented in this thesis is acquired in a peak force tapping mode using a *Bruker Multimode 8* controller (with *Bruker ScanAsyst*).

3.5.1. AFM as Complementary Technique to Scattering Experiments

As x-ray scattering experiments do not allow to extract local sample morphologies, AFM measurements are an important complementary technique in order to gather a more complete data set of the sample. Typically, x-ray experiments are performed *in-situ* and in real time during thin film growth while AMF micrographs are recorded *ex-situ* at separately prepared samples. Thus, it is important to define measures that allow direct comparison between microscopic and scattering experiments.

Island densities
As described in Section 3.3.6 GISAXS measurements allow extracting the island density of a sample. Information on the island density is also contained in AMF micrographs. In GISAXS measurements the island density is evident through a peak splitting in the intensity profile over $q_{\parallel}$ (see above). The *2d Fourier transformation* of an AMF micrograph contains the equivalent measure (see Figure 3.17). On a technical level, there is an obstacle in realising this method based on the differing definitions of the *Fourier transformation* used in physics and digital data analysis.[122] In physics it is common to use

$$F(q) = \int_{-\infty}^{\infty} f(x) e^{-iqx} dx \qquad f(x) = \frac{1}{2\pi} \int_{-\infty}^{\infty} F(q) e^{iqx} dq, \tag{3.20}$$

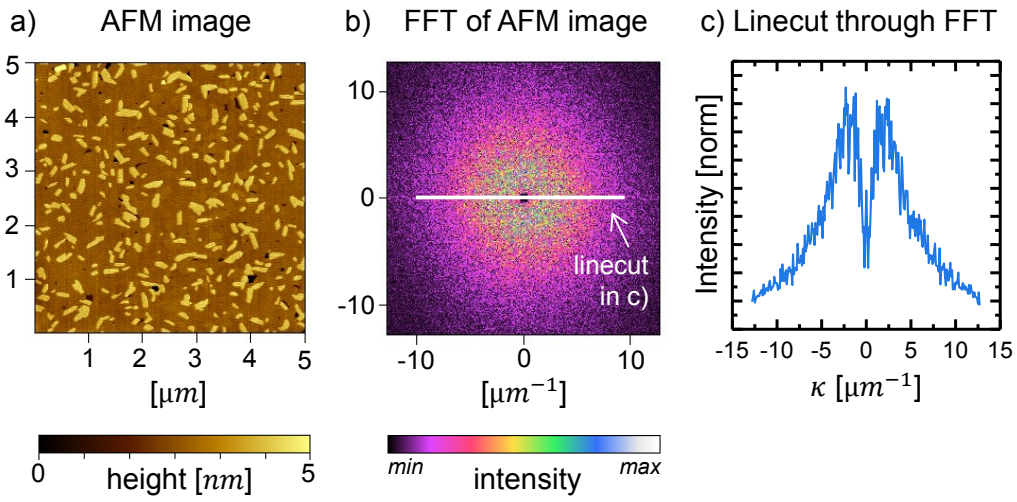

FIGURE 3.17: Line profile extracted from 2d FFT of AFM micrograph allows for direct comparison with peak splitting observed in grazing incidence small angle diffraction.

while for data analysis it is common to use

$$F(\kappa) = \int_{-\infty}^{\infty} f(x) e^{-i2\pi\kappa x} dx \qquad f(x) = \int_{-\infty}^{\infty} F(\kappa) e^{i2\pi\kappa x} d\kappa. \tag{3.21}$$

Therefore, for direct comparison between experimental $q_{\parallel}$-splitting in GISAX and the splitting extracted from AFM images based on the discrete version of Equation 3.21 the factor 2π in $q = 2\pi\kappa$ has to be regarded.

Surface roughness

Regarding the out-of-plane morphology, a direct comparison between AFM micrographs and anti-Bragg rate equation models (see Section 3.3.3) can be achieved through the *root-mean-squared roughness* (RMS roughness). For AFM measurements the RMS roughness is defined as

$$R = \sqrt{\frac{1}{n} \sum_{i=1}^{n} |y_i - \bar{y}|^2}, \tag{3.22}$$

with y_i the height of pixel i, the mean height $\bar{y}$ and n the number of pixels in the micrograph.[121]

3.6. Optical Microscopy Revealing *nm* Height Resolution by Interference Contrast

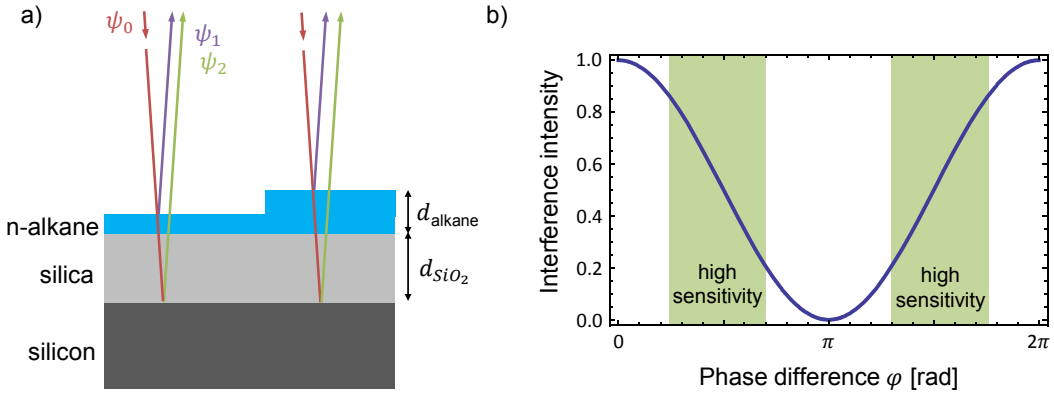

FIGURE 3.18: Optical microscopy with interference contrast to detect n-alkane layer thickness variations in the order of *nm*. To enhance sensitivity, the thickness of the silica layer has to be adapted according to the wavelength of the illuminating laser. Cf. [123]

To follow the temporal evolution of morphological changes in TTC thin films under annealing conditions as described in Chapter 7, we use a setup developed by Köhler *et al.* to resolve individual molecular monolayers in optical microscopy.[123] It is illustrated in Figure 3.18a and makes us of interference contrast. The sample consists of a multilayer n-alkane thin film ($n_{\text{alkane}} \approx 1.50$) that features a similar refractive index as the underlying silica layer ($n_{\text{SiO}_2} \approx 1.46$) at 532 *nm* illumination. The Si substrate has a significantly different refractive index with $n_{\text{Si}} \approx 4.15$ at 532 *nm*.[124]

The sample is illuminated with coherent light so that an interference pattern based on the optical path length difference depending on the local thickness of the alkane thin film can be observed. Considering ψ_0 as the incoming wave there is $\psi_1 = r_1\psi_0 e^{i\pi}$ for the wave reflected at the air-alkane interface. Neglecting the interface between alkane thin film and SiO layer due to their similar optical density we find

$$\psi_2(d_{\text{alkane}}) = t_1 r_2 \psi_0 e^{\frac{2\pi}{i}\lambda(2n_{\text{alkane}}d_{\text{alkane}}+2n_{\text{SiO}_2}d_{\text{SiO}_2})} \tag{3.23}$$

for the wave reflected at the SiO / Si interface. $r_i = \frac{n_a - n_b}{n_a + n_b}$ and $t_i = \frac{2n_a}{n_a + n_b}$ are the Fresnel coefficients for the corresponding interface at normal incidence. The overall reflected intensity $|\psi_1 + \psi_2(d_{\text{alkane}})|^2$ therefore depends on the local thickness of the alkane (d_{alkane}) film. There are also contributions resulting from multiple reflections that are not considered here.

To enhance the sensitivity of the system and to be sensitive of thickness variation of molecular monolayer height (in the order of few *nm*) the thickness of the silica layer d_{SiO_2} has to be chosen such that the phase difference between ψ_1 and ψ_2 lies close to multiples of $\pi/2$ to yield maximal intensity contrast (highlighted regions in Figure 3.18b).

3.7. Modelling Growth in Real Space in the Framework of Phase-Field Theory

Real space experiments are often beneficial in order to gain additional insights on processes affecting the surface morphology of organic thin films. Therefore, they are excellent complementary techniques to the presented x-ray methods that probe reciprocal space. Only in very few cases real space experiment are capable to deliver real time, *in situ* data (e.g. the annealing experiment described in Chapter 7). This is due to the fact they mostly require a local probe close to the sample surface, e.g. in AFM or optical microscopy. To study organic thin film growth in real space, there are comparably few experiments, relying mostly on low energy electron microscopy (LEEM).[93]

Another approach is to simulate the growth process and thereby identify underlying mechanisms producing the resulting surface morphologies. There has been great progress using *kinetic Monte Carlo simulations* to capture all microscopic processes on the surface and to simulate growth in a quantitative manner.[29,125] Challenging however, is the high temporal resolution that is needed in order to capture surface diffusion processes occurring on a μs time-scale to simulate monolayer growth on the time-scale of minutes or hours.[125]

To bridge molecular surface dynamics on the nano scale and macro scale multilayer thin film growth, effective theories can be used in order to reduce the necessary temporal resolution in the simulation and thus allow one to run the simulation for larger surface areas with affordable computational efforts.[126] Besides *cellular automata algorithms*[127] and *level set methods*[126,128] another approach is to use *phase field theory* that relies on a diffusion equation for the concentration of a mobile species $u(\mathbf{r}, t)$ and a differential equation capturing the solidification process into immobile coverage $\Phi(\mathbf{r}, t)$.[30,129] The governing equations in phase field theory are

$$\frac{d\Phi}{dt} = \frac{1}{\tau}\left[W^2\nabla^2\Phi - 2sin(2\pi\Phi) - \lambda u(2cos(2\pi\Phi) - 2)\right] + \lambda_n u^{i^*+1} \tag{3.24}$$

$$\frac{du}{dt} = \nabla\left[D(\mathbf{r}, t)\nabla u(\mathbf{r}, t)\right] - \frac{d\Phi}{dt} + \text{random deposition}(\mathbf{r}', t') \tag{3.25}$$

$$D(\mathbf{r}) = \begin{cases} e^{-\frac{E_D+E_{ES}}{k_B T}}, & \text{at surface step edges} \\ e^{-\frac{E_D}{k_B T}}, & \text{otherwise} \end{cases} \tag{3.26}$$

as described in references [30, 129–132]. Equation 3.24 is motivated in ref. [129] as a gradient penalty for creating steps followed by the *sin* term describing the tendency for Φ to select integral values corresponding to terraces, the *cos* term expressing diffusion-mediated step edge evolution. The last term integrates island nucleation in to the equation. The involved constants are

- W : thickness of phase-field transition zones
- λ : coupling constant

- λ_n : nucleation rate of islands
- τ : the characteristic time of attachment of ad-atoms at boundaries of islands
- i^*: critical nucleus size

Equation 3.25 describes the density of diffusing solitary particles i.e. the ad-atom gas. The diffusion constant $D(\mathbf{r})$ varies spatially and shows reduced values at surface step edges (see also Figure 2.3). The random deposition term captures the incoming flux of molecules during thin film growth. Matching the given deposition rate the value of u is increased at a random location $\mathbf{r}'$ at t'.

In order to use the presented equations to quantitatively simulate growth processes, the values of the involved constants that are either not directly experimentally accessible quantities (e.g. τ) or are not physically based (e.g. W and λ), have to be determined. This can be done on the basis of numerical considerations e.g. for W, which can be chosen just big enough to not produce numerical instabilities when solving Equation 3.25 in a finite difference scheme. For τ and λ the parameter space has to be explored through repeated simulations to find meaningful values.

Within the framework of this thesis a phase field code has been developed and implemented in *Java* in order to follow the surface evolution during thin film growth in real space based on a finite difference method. Due to temporal limitations, the parameters for organic growth have so far not fully been determined as described above and therefore, only qualitative results are presented.

Details on the code, concerning the numerical scheme can be found in Appendix C where the chosen approach to discretise $\nabla\left[D(\mathbf{r},t)\nabla u(\mathbf{r},t)\right]$ in 2d ($\mathbf{r}\in\mathbb{R}^2$) is described.

II

Experimental Results and Discussions

4

Controlling Polymorphism and Phase Purity in Organic Thin Films by Light

The aim of the work presented in this chapter is to show how laser illumination of α-Sexithiophene (6T) during growth leads to thin films with higher phase purity compared to those grown in the dark, suggesting that light can be used as a new control parameter to influence the molecular crystal structure in organic thin film growth. We find that illumination during growth suppresses the formation of high temperature phase (HT) crystallites by about a factor of 4 and increases low temperature phase (LT) purity, thereby improving the quality of the thin film. The findings presented in this chapter were published in references [76] and [133]. In part the text and figures have been adapted or reprinted with permission of the publisher American Chemical Society to reuse the article Crystal Growth & Design, 2015, 15 (3), pp 1319–1324, Copyright 2015 the American Chemical Society. [1]

6T is a well-studied organic semiconductor often used in thin film transistors[134] as well as in organic photovoltaics.[135,136] 6T thin films are crystalline but exhibit bimodal growth of both low-temperature[2] (LT) and high-temperature[3] (HT) phases (see Figure 1a). Both phases also occur in single crystals when grown from melt (HT-phase)[137] or by sublimation (LT-phase).[134] For thin films of 6T and the structurally similar quaterthiophene (4T) a number of studies report the occurrence of the HT-phase as well as further crystal

[1] A detailed listing of the contributions of all individual co-authors can be found on page 161.
[2] LT structure: a=44.71 Å, b=7.85 Å, c=6.03 Å; β=90.8°
[3] HT structure: a=9.14 Å, b=5.68 Å, c=20.67 Å; β=97.78°

polymorphs.[66,98,138–141] In 6T bulk crystals the HT-phase is predicted to be more stable than the LT phase.[65] The tilt angle ϕ between the long molecular axis and the small basal plane of the unit cell varies for the two structures with $\varphi_{\mathrm{LT}} = 65.9°$ and $\varphi_{\mathrm{HT}} = 56.3°$.[142] This different molecular tilt angle results in a different lattice spacing of 22.35 Å for the LT and 20.67 Å for the HT phase in the direction normal to the substrate surface (Figure 4.1a).[134] Thin films of 6T grown on KCl are known to be crystalline and consist of upright standing and flat lying molecules, where upright standing molecules often nucleate at lying down molecules in so-called ledge directed epitaxy.[143,144] The different molecular orientations and crystal structures are characterised by specific spectroscopic signatures in UV-Vis emission, depending on the intermolecular and molecule- substrate interactions as has been shown in references [145] and [146] for few monolayer coverages.

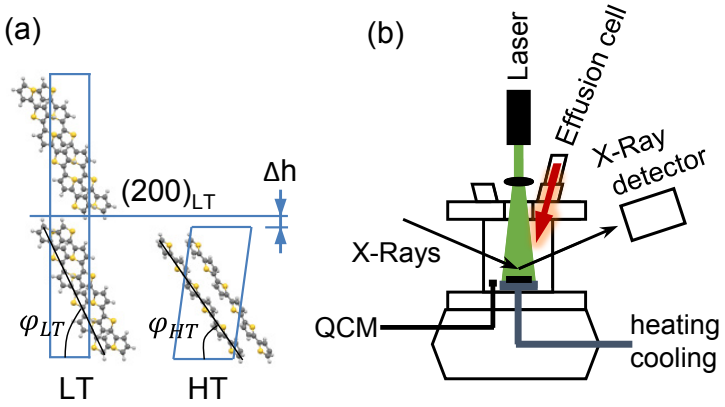

FIGURE 4.1: a) Low-temperature (LT) and high-temperature (HT) phase of 6T. The unit cell of LT (HT) consists of four (two) molecules. The molecular tilt angle φ is shown for both structures. b) Deposition geometry used in the experiment. Compared to conventional OMBD setups a 532nm laser is added to illuminate the sample during growth.

For this experiment[76] an OMBD setup as described in Chapter 3.1 is additionally equipped with a 532 nm laser that enters the vacuum chamber perpendicular to the substrate surface (Figure 4.1b). A telescope expands the laser beam to a full width half maximum (FWHM) of 14 mm, so that the $10 \times 10\, mm^2$ substrate is homogeneously illuminated. Cleaved KCl substrates are heated up to 420 $°C$ in vacuum to reduce surface contamination prior to the deposition. All films are grown with molecular deposition rates between 1 and 1.5 $Å/min$ to a thickness of (150 ± 20) Å. Real time x-ray measurements were performed at the surface diffraction end station of the MS beamline at the Swiss Light Source (Paul Scherrer Institute, Switzerland) using a photon counting Pilatus 100k detector at an energy of 16 keV.[80]

4.1. Results

To get an overview of the post-growth 6T film morphology, Figure 2a shows an AFM scan of a 150 nm thick 6T film on KCl grown without laser illumination at $T_{sub} = 60\,°C$. Islands

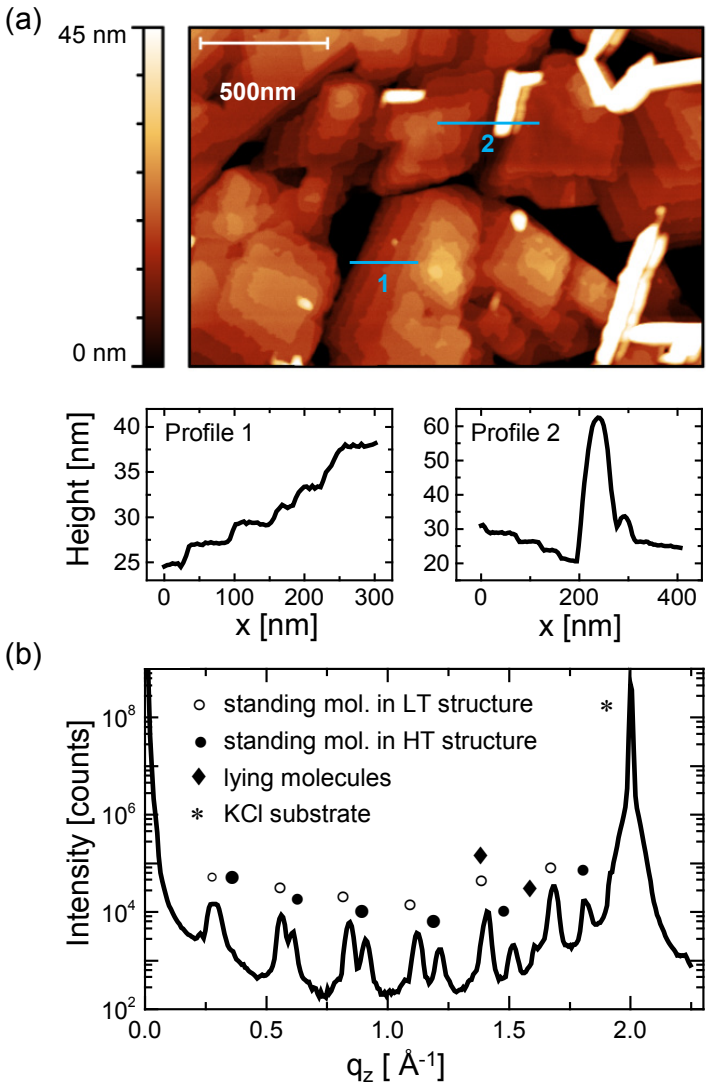

FIGURE 4.2: a) AFM micrograph showing the surface morphology of a 6T film on KCl grown in the dark at T_{sub}= 60 °C. Standing molecules form terraces with monomolecular step height and some 'needle-like' structures (white) are formed by flat lying molecules. b) $\theta/2\theta$- scan of a 6T film as shown in a). The recorded Bragg-reflections are labelled based on the according crystal structure.

of upright standing molecules with terraces of monomolecular step height of (22 ± 2) Å are clearly visible, and some 'needle-like' structures consisting of flat lying molecules are seen, in agreement with previous AFM results by Schwabegger *et al.* .[143] The step height difference between HT and LT phases cannot be resolved in our AFM image because it differs by only 2 Å. A corresponding X-ray $\theta/2\theta$- scan is shown in Figure 2b, exhibiting multiple Bragg-reflections due to upright standing molecules. Interestingly, these Bragg reflections are split into pairs, indicating a polymorphous growth behaviour of the upright standing molecules in both LT and HT crystal structures. Note that in the LT structure the long unit cell axis is defined as *'a'* whereas in the HT structure it is *'c'*.[137,147] For the LT structure the {100} plane forms the contact plane with the substrate resulting in (h00) labels for corresponding Bragg reflections, whereas for the HT phase the {001} plane forms the contact plane to the substrate resulting in (00l) labels for Bragg reflections of the HT phase. The higher order Bragg reflections indicate high structural order of the crystalline islands. At higher q_z the (-411) and (020) Bragg reflections are visible, which correspond to flat lying molecules, and the (200) KCl substrate reflection (see Section A.1.1 for details).

4.1.1. Phase Purification

In Figure 4.3a we compare the Bragg reflections of films grown in the dark and under illumination, with otherwise identical growth conditions. The blue curve corresponds to a film grown at $T_{sub} = 60\,^{\circ}C$ without illumination, while the red curve corresponds to a sample exposed to 532 *nm* laser illumination during thin film growth. Interestingly, the HT polymorph is significantly suppressed. In other words, illumination with 532 *nm* laser light increases the LT phase purity of the thin film. In order to define a quantitative measure for the increased film purity, we use the quantitative phase analysis formalism within the Rietveld method (see Section 3.3.8). From this we deduce under the given constrains the relation

$$\frac{m_{\mathrm{HT}}}{m_{\mathrm{LT}}} = \frac{I_{(hkl)_{\mathrm{HT}}}}{I_{(hkl)_{\mathrm{LT}}}} \; \frac{Z_{\mathrm{LT}}\, V_{\mathrm{LT}}}{Z_{\mathrm{HT}}\, V_{\mathrm{HT}}} \frac{F^2_{(hkl)_{\mathrm{HT}}}}{F^2_{(hkl)_{\mathrm{LT}}}} \tag{4.1}$$

with $m_{\mathrm{HT}}/m_{\mathrm{LT}}$ being the mass ratio between two co-existing crystal phases HT and LT in the sample, I the measured reflection intensity, Z the number of 6T molecules per unit cell and V the respective unit cell volume. We calculated the structure factors, which describe the strength of the Bragg reflections, to be $F_{(600)_{\mathrm{LT}}}$= 51.8 and $F_{(003)_{\mathrm{HT}}}$= 24.6.[148]

For the films shown in Figure 4.3a this leads to a mass ratio of $(m_{\mathrm{HT}}/m_{LT)_{\mathrm{dark}}}$= 0.077 and $(m_{\mathrm{HT}}/m_{LT)_{\mathrm{illum}}}$= 0.27 respectively, thus the growth of the HT phase is suppressed by a factor of 3.5. Using this quantitative measure, we consistently find a reduction of the HT phase content by a factor of 3 to 5 for more than 20 samples grown in this study, with the exact factor depending on substrate temperature during growth and also on variations

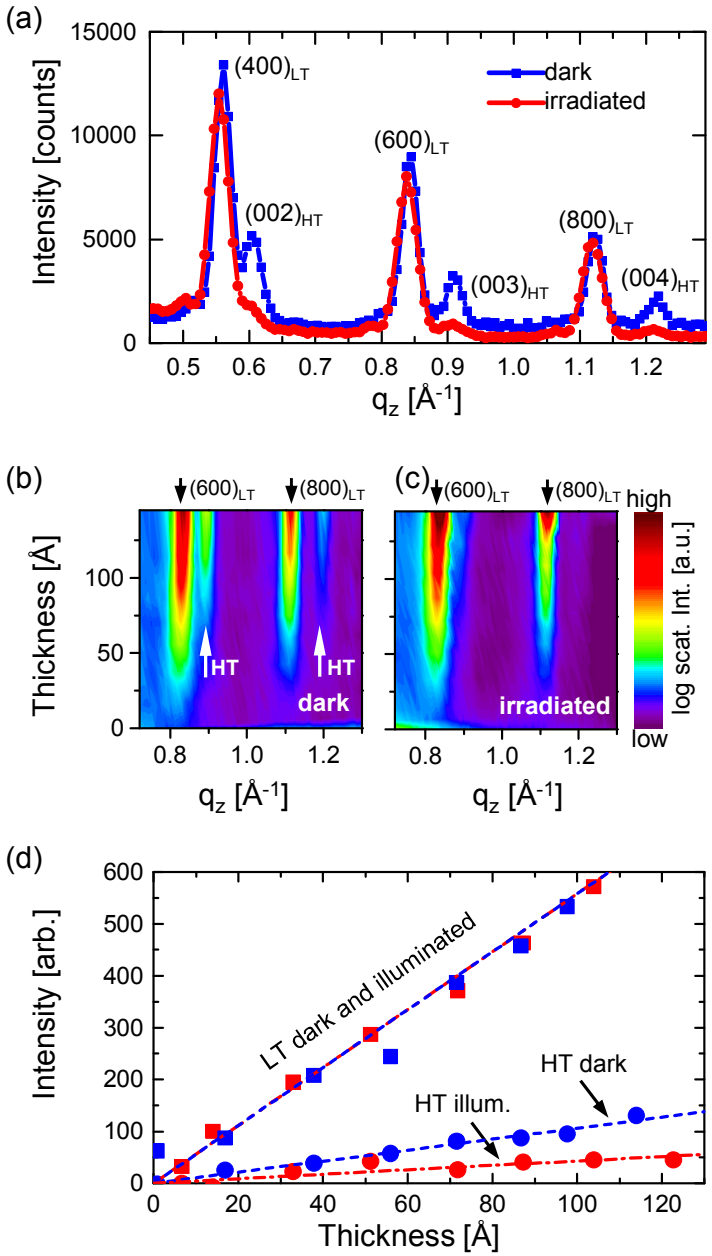

FIGURE 4.3: a) Post-growth $\theta/2\theta$-scans of 6T films on KCl grown in the dark (blue) and under illumination (red). The time resolved scattering intensity for the $(600)_{LT}$ /$(003)_{HT}$ and $(800)_{LT}$ /$(004)_{HT}$ reflection pairs is shown for films grown in (b) the dark and (c) illuminated environment. (d) Square root of the Bragg reflection intensities with and without illumination.

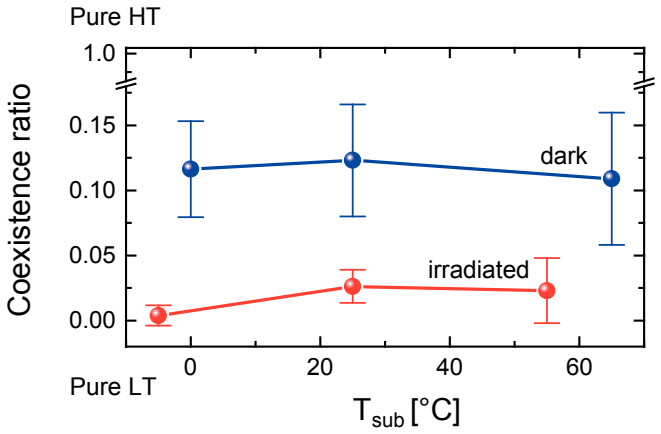

FIGURE 4.4: Growth and nucleation of the HT phase in a temperature range of over 60 K, with and without laser illumination is suppressed more than a factor of 3 to 5 through illumination.

in microscopic substrate quality, such as variations in KCl step edge density on cleaved surfaces.

To study the early-stage nucleation behaviour of HT and LT polymorphs and to find out whether both nucleate simultaneously or one phase appears after a critical thickness, we monitored the thin film growth process by means of time resolved in situ x-ray measurements during growth. In Figure 4.3b and c we present the Bragg intensity of the $(600)_{LT}$ / $(003)_{HT}$ and $(800)_{LT}$ / $(004)_{HT}$ reflections, which increases as a function of film thickness (that is growth time × molecular flux). Figure 4.3b shows the thin film growth in a dark environment with fairly strong reflections of the HT structure. In contrast, in the film grown under illumination (Figure 4.3c) the HT reflections are barely visible. In Figure 4.3d we present the integrated intensities of the $(600)_{LT}$ and $(003)_{HT}$ Bragg reflections, which increase linearly with the thickness of the emerging film. Both with and without laser illumination, at the start, there is no delay in HT phase formation and both phases crystallise simultaneously. However, the growth rate of the HT phase is reduced by a time independent factor via laser illumination.

After demonstrating the impact of laser illumination on phase purity, we show here that this effect is not simply caused by laser-induced heating of the substrate, but by interaction of the laser light with the molecular film. The use of an optically transparent substrate allows us to exclude significant absorption of light in the substrate. We estimate the uncertainty in the substrate temperature measurement at the sample holder to be in the range of ±5 °C with and without laser illumination. To exclude an influence of this small temperature uncertainty, in Figure 4.4 we compare films grown in a range of 60 K with and without laser illumination by calculating the phase coexistence ratio based on the integrated Bragg intensity of the $(003)_{HT}$ and $(600)_{LT}$ reflections. We find that this ratio between the two phases is independent of the substrate temperature T_{sub} within the range of 60 K. From this we conclude that possible substrate temperature changes within ±5 °C

due to the laser illumination can be neglected in comparison with the 60 K range in which the effect is observed.

4.1.2. Stability of LT and HT Phase

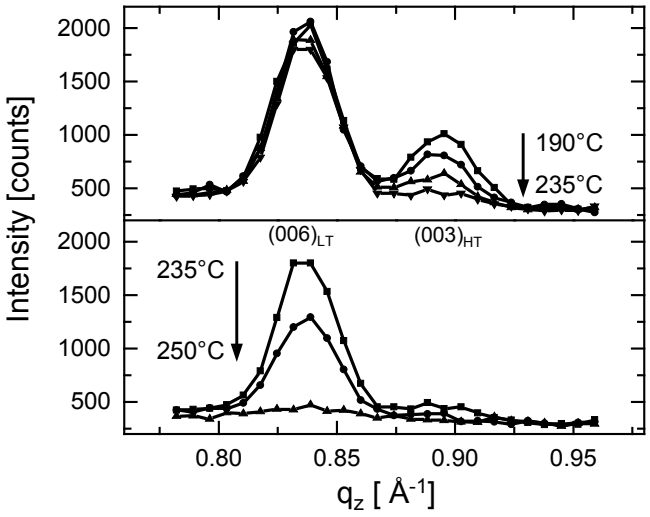

FIGURE 4.5: Desorption of 6T thin film in nitrogen atmosphere. Top: HT phase desorbs around 200 °C. Bottom: LT phase desorbs around 240 °C showing that in thin films the LT phase is more stable.

In a further experiment the temperature dependence of desorption of the two polymorphs at elevated temperatures is studied to determine which of the two phases is more stable. To do so, we heat a previously grown 6T film on KCl step by step in a nitrogen atmosphere. X-ray scans at different temperatures allowed us to monitor and separate the temperatures at which the reflections of the two crystal phases disappear. The results are shown in Figure 4.5. The reflections corresponding to the HT structure start to disappear at a significantly lower temperature (190 °C) than the reflections of the LT structure (235 °C, both for flat lying and upright standing molecules). The lower thermal stability of the HT phase in our samples is an important factor in explaining why the HT phase is suppressed by light. The energy of the absorbed light dissipates as heat in the molecular crystal through molecular excitation and conversion processes.

To study the difference in the thermal stability in more detail and also investigate the difference in the desorption energy barrier E_d of the two crystal structures the desorption rates of both LT and HT phase crystallites at a fixed temperature are measured. Heating this 6T film to a temperature of $428 \pm 15\,K$,[4] corresponding to the onset of molecular desorption, we observe that the intensities of the Bragg reflections drop linearly as shown in Figure

[4] the systematic difference in the observed desorption temperatures compared to the results presented above is due to distinct experimental setups and thereby define the uncertainty in the temperature measurement.

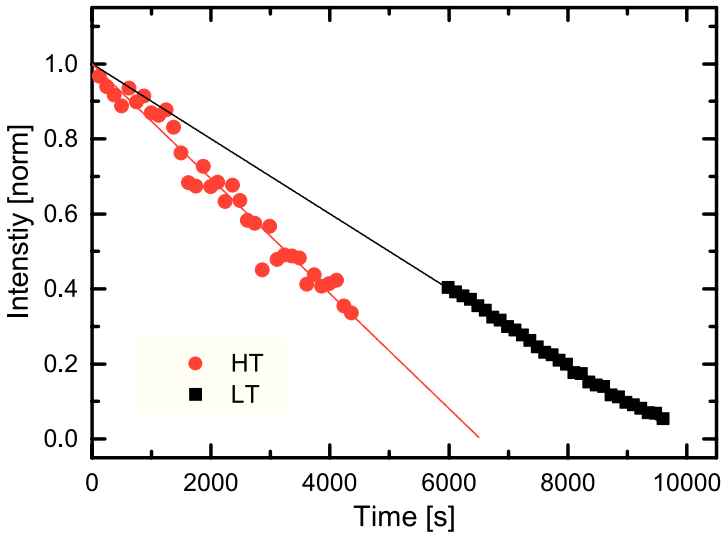

FIGURE 4.6: Decay of the $(003)_{HT}$ and $(006)_{LT}$ Bragg reflection intensities over time at a substrate temperature T=428 ± 5 K.

4.6. Interestingly, the HT phase desorbs at a faster rate [$R^{HT} = (1.531 \pm 0.050) \cdot 10^{-4}$ s^{-1}] than the LT phase [$R^{LT} = (1.000 \pm 0.011) \cdot 10^{-4}$ s^{-1}], indicating a higher stability of the LT phase.

For a quantitative analysis, we explain the differences between the temporal decay of the two Bragg intensities by a difference in desorption energy barriers E_d. Assuming that the Bragg intensity is directly proportional to the respective amount of HT or LT phase, the constant slope of the decay curves can be explained by molecular desorption from step edges at a constant rate without any significant morphological changes of HT and LT islands. In atomic force microscopy measurements, resolving molecular terraces of standing upright molecules, we find no distinctly different HT and LT islands, so that a similar geometry is assumed for both phases. We use an Arrhenius-type relation of the desorption rate $R = -A\, e^{-E_d/k_B T}$ with the molecular desorption energy E_d, the (constant) temperature T, and an attempt frequency A. Assuming $A = A^{LT} = A^{HT}$ for both phases, one can write

$$\ln\left(\frac{R^{HT}}{R^{LT}}\right) = -\frac{E_d^{HT}}{k_B T} + \frac{E_d^{LT}}{k_B T}. \tag{4.2}$$

Therefore the desorption energy difference $\Delta E_d = E_d^{LT} - E_d^{HT}$ is given by

$$\Delta E_d = \ln\left(\frac{R^{HT}}{R^{LT}}\right) \cdot k_B T. \tag{4.3}$$

From the decay rates we estimate $\Delta E_d = (15.7 \pm 3.1)\, meV$ between the two phases. This finding is in qualitative agreement with calculated values between 50 and 100 meV that are calculated based on density-functional theory (DFT) with different approaches to

include *van der Waals* interactions.[133] The calculations have been performed by B. Klett, C. Cocchi and C. Draxl.
The desorption energy difference is approximately 2–3 times smaller than the computed difference in relative stability. This discrepancy may be rationalised conceptually based on the idea that thermal desorption processes occur at the surface, where each molecule interacts only with a reduced number of nearest neighbours compared to the bulk, resulting in intrinsically lower binding energies. The DFT calculations in [133] do not take into account these surface effects but rather represent bulk values.
In the calculations as well as in the experiment we find the LT phase to have a higher binding energy than the HT phase. Thus, the HT phase is thermally less stable than the LT phase.

4.1.3. Differences in the Optical Properties of LT and HT Phase

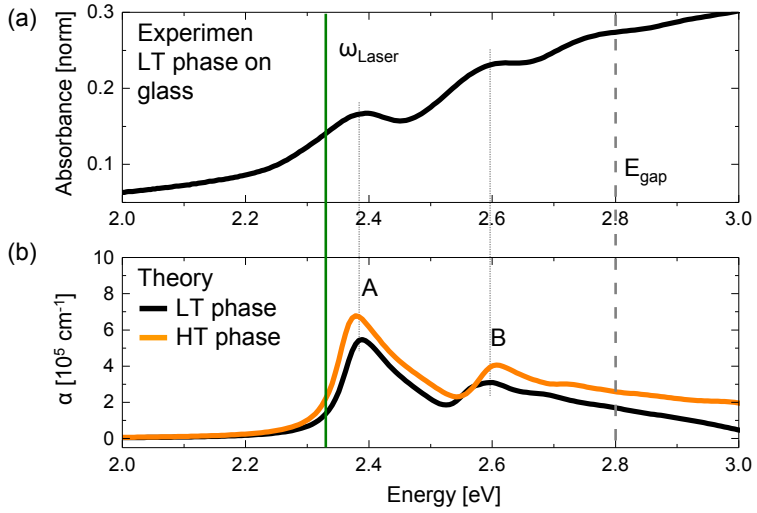

FIGURE 4.7: a) Onset of the experimental LT absorption spectra close to the photo-excitation energy; b): BSE calculation of the absorption coefficient α for an electric field lying on the substrate surface plane of LT and HT. The solid green line indicates the laser frequency ω_{Laser} (2.33 eV) while the grey dashed line at 2.8 eV is the computed fundamental gap for both structures. The peaks A and B are bound excitons. A Lorentzian broadening of 25 meV is applied to the computed spectra.

A further contribution to the suppression of the HT phase could be a differing absorption of the two phases. In order to better understand whether the two phases absorb 532 nm light differently, e.g. through different absorption coefficients or spectral shifts, we performed *ab initio* calculations of the optical absorption spectra of HT and LT. Computational details on the first-principle calculations performed in the framework of density-functional and many body perturbation theory with the `exciting` code[5] can be found in the references [76, 133, 149]. The results are shown in Figure 4.7. We computed in collaboration with C.

[5] http://exciting-code.org

Cocchi and C. Draxl the absorption coefficient α at normal incidence, with the electric field parallel to the substrate contact planes of the unit cells (b-c plane for LT and a-b plane for HT structure). The computed peak positions of the LT polymorph agree with the experiment (see Figure 4.7). The HT spectrum is only theoretically accessible, as no pure HT films could be grown. Comparing the theoretical HT and LT spectra, we find that the two phases have very similar optical absorption. The low-energy part is characterised by two strong excitonic peaks, A and B, which lie within the gap, E_g = 2.8 eV, for both HT and LT. The binding energies of these excitons are E_b (A) = 0.41 eV and E_b (B) = 0.19 eV in the LT phase and E_b (A) = 0.45 eV and E_b (B) = 0.22 eV in HT. It is important to note that exciton A lies within 10 meV above the frequency of the green laser.

The similarity of the absorption energies of A and B in the two phases points towards a minor role of excitonic shifts in the selective growth of LT upon laser illumination. Although, a slight difference in the absorbance can be observed in the spectra of Figure 4.7b, the height of peak A is about 20 % smaller in LT compared to HT. This feature can be associated with the different orientation of the molecules on the substrate, as shown in Figure 4.1a. Since the optical transition giving rise to peak A is aligned along the long molecular axis, the HT phase with a lower tilt angle has a better alignment between the optical transition and the electric field direction of the laser leading to higher absorption.

4.2. Discussion

The results presented above clearly indicate an influence of light on the crystallisation behaviour of 6T thin films beyond simple substrate heating. In the following we examine possible mechanisms that can explain this effect. These are excited-state crystallisation, optical absorption with subsequent local heating of LT and HT nuclei, as well as different cohesive energies.

Crystallisation in the photo-excited state has a negligible effect in this system, because the molecules are mostly in their ground state. Taking into account an absorption length of α=93 nm for 6T thin films[150] at 530 nm, there are roughly 10^5 absorbed photons per molecule for the given illumination at 1.5 W/cm^2 during the 20 min growth time of one molecular monolayer. Due to short exited-state life-times of less than 1 μs[151] combined with the low laser intensities, molecules are 99.999 % of the time in the ground state under the assumption of similar luminescence behaviour of the two phases.
As shown by first-principles calculations, the excitonic peak A, which is the closest to the wavelength of the illuminating laser, lies approximately at the same energy for the two phases. Hence, the influence of light on the growth of 6T cannot be explained by dissimilar absorption energies of peak A and thus a different overlap with the laser line. However, we notice that the oscillator strength in HT is 20% higher than in LT phase, due to the tilt of the molecules in the unit cell. Hence, molecules in the HT phase absorb more light than in the LT phase. Therefore molecules in HT orientation exhibit an increased laser-induced heating and gain additional energy.

From the desorption behaviour, we find a reduced thermal stability of the HT phase compared to the LT phase for the given sample morphology and phase mixture. The performed *ab initio* calculations also find the LT phase to be more stable than the HT phase. Therefore, we claim good agreement between our theoretical and experimental results, which identify the LT phase as the more stable one. It is finally worth mentioning that our result is in contrast with a previous work based on classical force-fields calculations.[65] In that case, the authors found the HT polymorph to be energetically favoured with respect to LT by about 15 meV/molecule. Although the absolute value of this difference is rather small, we can attribute the better accuracy and, importantly, the correct sign of our result to the inclusion of many body perturbation theory into the calculation.

4.3. Conclusion

In conclusion, the combination of the lower thermal stability of the HT phase in 6T thin films with stronger optical heating of molecules, as discussed above, can explain the origin of the observed phase purification. Additional contributions to the complex growth kinetics and phase coexistence could come from non-thermal excitation of vibrational modes, photo-electric charging, or an optical induced, direct phase transition from the HT into the LT phase. However, a quantification of these contributions goes beyond the scope of this work.
This finding demonstrates that light can serve as an additional control parameter in molecular crystal growth to optimise the structural quality of molecular thin films. As leading mechanism for this light-induced phase-purification we suggest a combination of a slightly more intense optical absorption in the HT phase together with a lower thermal stability of the HT phase. In Appendix A.2 we show preliminary results for pentacene where we also observe a transition in the phase coexistence ratio, similar to the behaviour of 6T discussed in this chapter.

5

Patterning and Controlled Azimuthal Alignment with Optical Fields

Molecular thin films are important building blocks in optoelectronics, biosensors and functional coatings.[152] Device functionality often requires supra-molecular assemblies, so that patterning techniques bridging self-assembly on the nanoscale and photo-lithographic techniques on meso- and macro-scales are highly relevant.[12] Here we report on light-directed molecular self-assembly (LDSA) generating permanently aligned thin films of the molecular semiconductor tetracene and demonstrate direct patterning with light. Light illumination of moderate intensity ($5\,W/cm^2$) induces an optical symmetry axis perpendicular to the light polarisation direction leading to azimuthally photo-aligned films on isotropic, amorphous substrates. This is evidenced by polarised fluorescence emission. We find azimuthal crystalline alignment and 'optical crystal twinning' in x-ray diffraction. The observed self-photoalignment and patterning enables novel device structures in organic electronics and is an important step towards structures such as vortex retarders,[153] photonic surfaces structures,[154] polarised organic light emitting diodes (OLEDs) or distributed feedback lasers[36] based on small organic molecules.

Organic single crystals feature pronounced anisotropy in their optical and electronic properties. They are birefringent[23] and show improved electronic mobility along specific crystallographic directions.[8,52–54] Technically relevant organic thin films on amorphous substrates, however, usually show only isotropic 'average' properties due to their poly-crystalline structure of azimuthally random oriented crystal grains and thereby lose the desirable anisotropy. Using e.g. single crystalline inorganic substrates[49,56,155] or alignment layers[59–61,156] leads to biaxial texture at the cost of increased processing complexity.

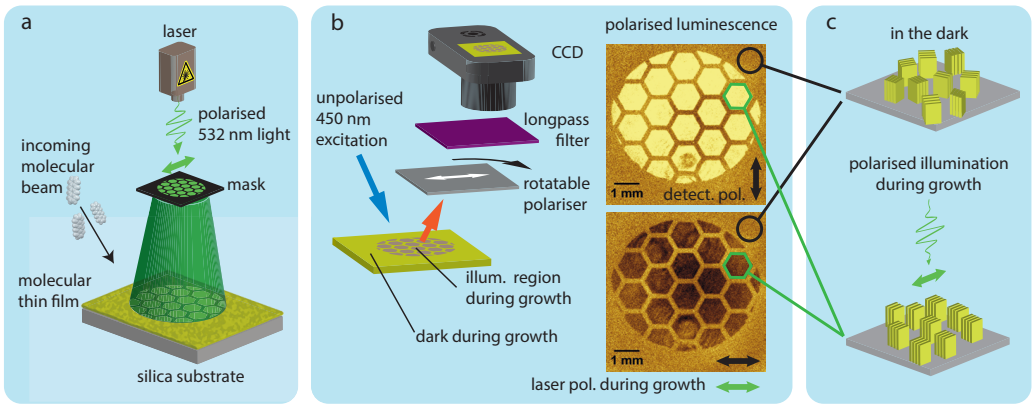

FIGURE 5.1: Direct photo-alignment and permanent patterning of tetracene thin films. a) Schematic illustration of the setup with an illuminating 532 nm laser, a shadow mask and molecular deposition process. b) Linearly polarised emission highlights anisotropy in the irradiated region's signal of a tetracene thin film grown via LDSA. The sample is excited by a 450 nm LED light source and photographs of the luminescence are recorded through a polarisation filter that is aligned to the laser polarisation during growth (bottom) and perpendicular to it (top). c) In regions that were dark during growth the orientation of molecular crystallites is randomly distributed, whereas there is a preferential orientation in the illuminated regions.

LDSA on the contrary exploits self-photoalignment to control molecular orientation in thin films through external optical fields. Direct photo-alignment has so far been used to temporarily orientate nematic liquid crystals.[157,158] Other photo-alignment methods require additional photoactive molecular species to introduce persistent anisotropy via chemical transformations such as photo crosslinking, dissociation or isomerisation.[23,24,58]

Besides molecular alignment, patterning is also highly desirable in order to produce functional structures. Here, we consider angular alignment to locally induce patterning on length scales significantly larger than individual crystal grains. A range of techniques to pattern molecular layers through external factors have been developed,[15,74,159] including laser-surface processing, also denoted as laser-induced periodic surface structures (LIPSS).[160] In contrast to LDSA, most methods either allow patterning or alignment of molecular structures in thin films, but not both simultaneously. Previously, photo-responsive molecular species such as polymers containing azo-benzene or surface assembled monolayers have been used to pattern and align molecular structures.[23,58,161] In turn this reduces the applicability to systems of very specific materials. Here we show that it is possible to align and pattern supramolecular structures in crystalline organic thin films with LDSA in a single step.

5.1. Experimental Setup for LDSA

In the LDSA process shown in Figure 5.1a, the sample is illuminated through a shadow mask with linearly polarised 532 *nm* light, while depositing tetracene molecules ($C_{18}H_{12}$,

Benz[b]anthracene) via organic molecular beam deposition as described in Chapter 3.1. The films are grown to a thickness of 15 nm to 25 nm at a rate of 1 to 3 $/min$ monitored by a quartz crystal microbalance. During growth, the substrate is cooled down to $T_{sub} = 220\,K$ to prevent desorption of deposited molecules from the substrate surface. After growth we probe the polarisation ependant luminescence properties (Figure 5.1b) and find a reproduction of the shadow mask in the fluorescence signal emitted by the sample. Regions of the sample which have been illuminated during growth show linearly polarised luminescence. In contrast, in regions that were in the dark during growth show unpolarised luminescence. Thus, the optical properties of the film are anisotropic in illuminated regions and azimuthally isotropic where the film was grown in the dark. This finding unravels the enhanced structural order induced by LDSA. The thin film formation process significantly differs in regions with and without illumination during growth. In dark regions during growth the individual crystal grains are randomly in-plane oriented, a polycrystalline structure also known as 2d powder (Figure 5.1c, top). On the contrary, molecular self-assembly in illuminated regions leads to azimuthally textured polycrystalline structures with preferred in-plane crystal orientations (Figure 5.1c, bottom). As control experiments (not shown here) we also grew samples in the dark for prolonged (300 min) post growth illumination with polarised 532 nm light. After post growth illumination these samples did not exhibit a significant anisotropy in their optical properties. That means LDSA only works during the thin film growth process and not subsequently. In the following we analyse the anisotropic optical and crystalline properties of tetracene films grown under illumination.

5.2. Results

5.2.1. Spectroscopic methods to analyse anisotropy in LDSA grown films

Probing the grown film by means of polarisation sensitive luminescence spectroscopy (Section 3.4.1) we find the emission to be aligned perpendicular to the polarisation direction of the light used to illuminate the sample during growth (Figure 5.2a and c). Using a polarisation sensitive differential reflectance spectroscopy (DRS) setup (see Section 3.4.2), we probe the absorption properties of the film (Figure 5.2). In the analysed spectral range we find the transition from the ground state S_0 to the first excited state S_1 and the corresponding vibronic progression in both absorption and emission. In the solid state spectra of tetracene the S_1 is split into two levels. Optical and structural properties of molecular crystals are defined through the properties of individual molecules and their interactions. Due to the non-primitive unit cell, containing two molecules, Davydov splitting is present (details in Chapter 2.1). In a quasi-classical transition dipole picture it is expressed by the vector summation of the monomer transition dipole moments (TDMs) $\mathbf{M_1}$, $\mathbf{M_2}$ leading to a splitting into two levels of monomer S_1 state (see Figure 5.2). There is the red shifted $\mathbf{D_+}=\mathbf{M_1}+\mathbf{M_2}$ at lower energies and the blue shifted $\mathbf{D_-}=\mathbf{M_1}-\mathbf{M_2}$ at higher excited state energy (see Section 2.1.3 for details). Due to the triclinic unit cell the

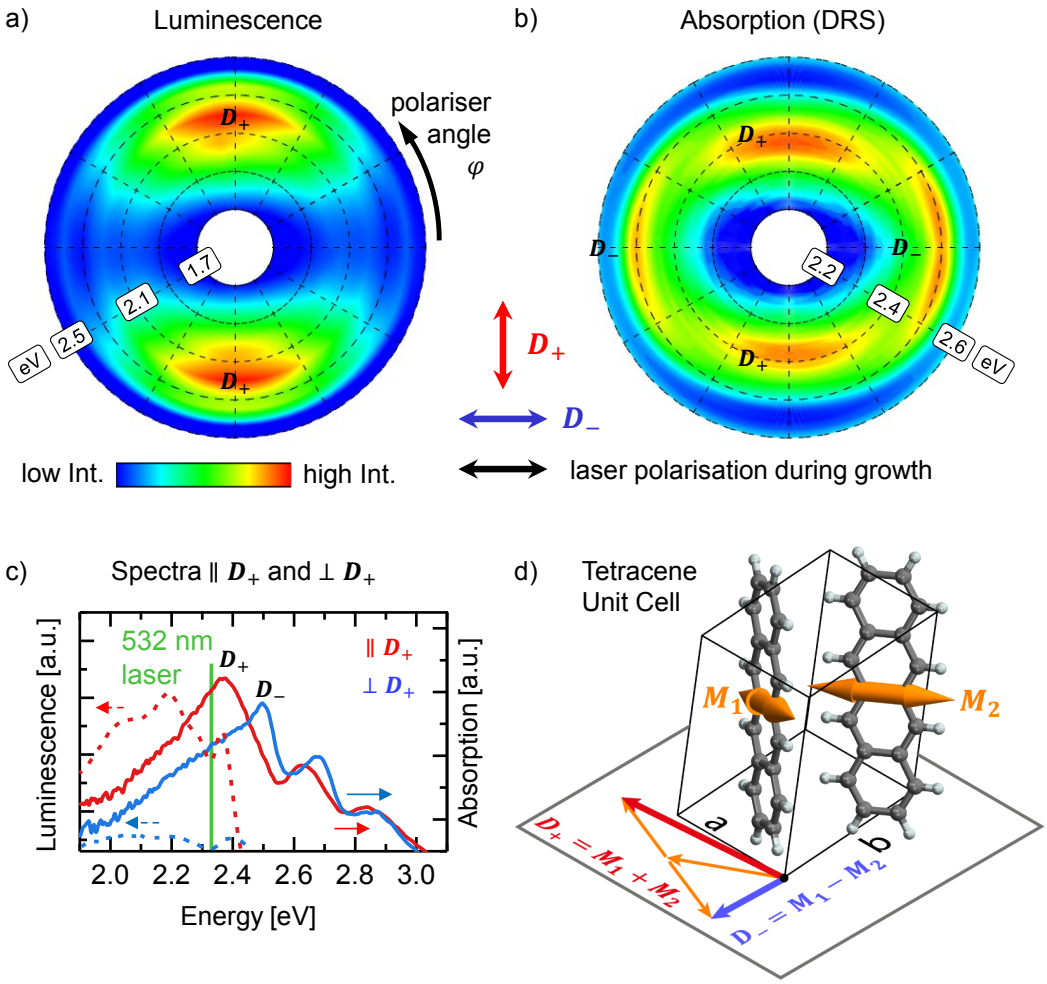

FIGURE 5.2: Anisotropic optical properties of photo-aligned tetracene thin films. a) Polarization resolved luminescence and b) absorption spectra of tetracene films grown under illumination. c) Line cuts through a) and b) with luminescence shown as dashed lines and absorption as solid lines. d) Orientation of in-plane components of molecular transition dipole moments (TDMs) and Davydov components $\mathbf{D}_+$ and $\mathbf{D}_-$ with respect to the molecular unit cell (unit cell).

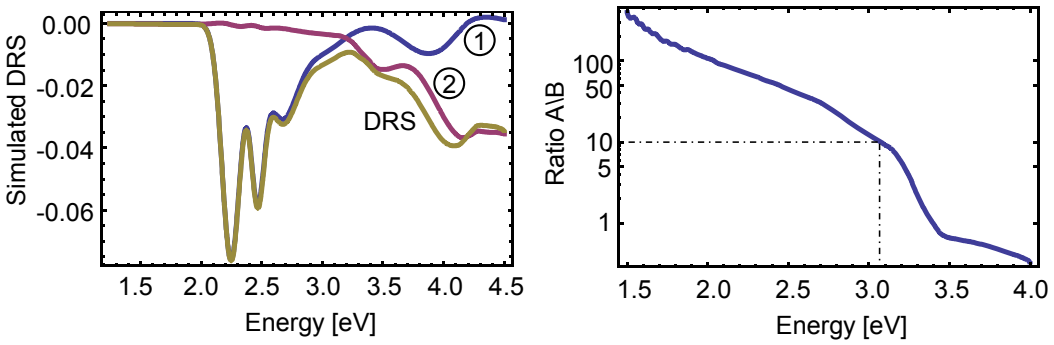

FIGURE 5.3: Simulated DRS for tetracene thin film on Si and the contributions from the terms (1) and (2) in equation 3.16; d) Ratio between A and B from equations 3.17,3.18. For energies below $3\,eV$ the ratio A/B is > 10 so that the *DRS* signal can be used to approximate the molecular absorption in the energy range between $1.5\,eV$ and $3.0\,eV$

directions of $\mathbf{D}_+$ and $\mathbf{D}_-$ are not identical to those of the unit cell axes a and b. However, $\mathbf{D}_+$ is almost parallel to a ($\sphericalangle(\mathbf{D}_-,a) \approx 4.3°$ in the ab-plane). As we illuminate the sample at normal incidence, only the $\mathbf{D}_+$, $\mathbf{D}_-$ components in the ab-plane of the unit cell (in-plane components) are relevant for the following discussion. The applied $2.32\,eV$ ($532\,nm$) laser excites the $\mathbf{D}_+$ state ($2.38\,eV$)[162] in resonance, while the $\mathbf{D}_-$ state at $2.46\,eV$[162] lies at considerably higher energy and therefore does not interact with the laser (see Figure 5.2). For the luminesence measurement shown in Figure 5.2, we illuminate a LDSA grown sample with blue $450\,nm$ unpolarised light and detect the luminescence intensity as a function of the polariser angle φ. We find a 180 ° degree symmetry and assign the observed luminescence feature to the lower Davydov component $\mathbf{D}_+$ as it is known from literature that the $\mathbf{D}_-$ state in tetracene is dark at room temperature.[163,164]. Similarity to the presented luminescence measurements we also apply a polarisation sensitive differential reflectance spectroscopy (DRS) to probe the anisotropic absorption properties of the LDSA grown film (Figure 5.2). As discussed in Section 3.4.2, the DRS signal can be used as a measure of the molecular absorption spectrum if the relation of the dielectric functions of film and substrate allow the approximation used in Equation 3.19. For the material system consisting of silicon as substrate and tetracene as molecular film the assumptions in Equation 3.19 are fulfilled in the spectral range between $1.5\,eV$ and $3.0\,eV$ (see Figure 5.3). We base this estimation (Figure 5.3) on the optical constants for tetracene derived by Gompf *et al.*[165] and Tavazzi *et al.*[162] from ellipsometry measurements and optical constants of silicon published by M. Green.[124]

The polarisation resolved absorption spectrum of a LDSA grown film (Figure 5.2) reveals both $\mathbf{D}_+$ and $\mathbf{D}_-$ at their corresponding energies polarised perpendicular to each other. In the samples grown by LDSA the crystallites are arranged such that the $\mathbf{D}_+$ transition is aligned perpendicular to the polarisation direction of the illumination during growth. This shows that the formation of crystallites resonantly absorbing the laser light during growth is strongly suppressed.

To quantify the degree of anisotropy induced by LDSA, several films have been grown

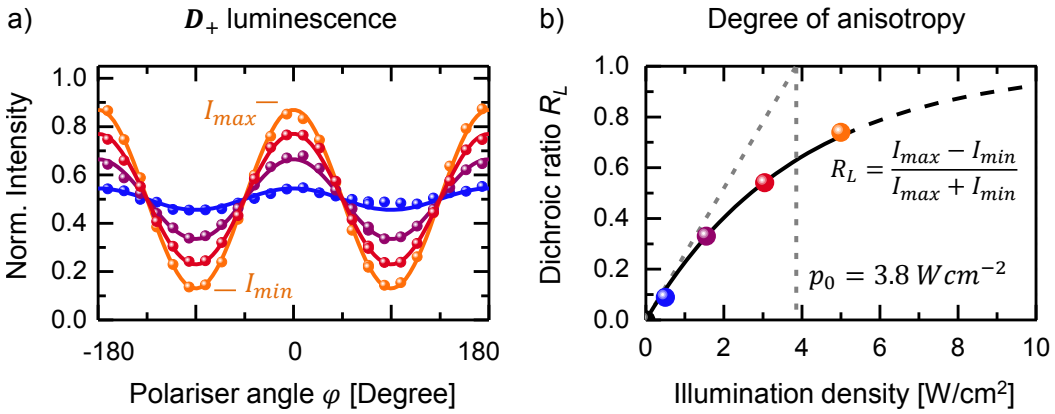

FIGURE 5.4: a) Normalized angular resolved luminescence intensity of $\mathbf{D}_+$ (blue: $5\,Wcm^{-2}$, violet: $3\,Wcm^{-2}$, red: $1.5\,Wcm^{-2}$, orange: $0.5\,Wcm^{-2}$, lines correspond to the model presented below). b) Dichroic luminescence ratio of tetracene films grown at different illumination intensities (colours correspond those in a)).

using different illumination intensities. We acquire the $\mathbf{D}_+$ luminescence intensity as a function of the azimuthal polarisation angle (Figure 5.4) that allows us to measure the anisotropy in terms of the dichroic luminescence ratio

$$R_L = \frac{I_{\max} - I_{\min}}{I_{\max} + I_{\min}}. \tag{5.1}$$

$I_{\max}$ and $I_{\min}$ are the $\mathbf{D}_+$ luminescence intensities perpendicular and parallel to the illuminating laser during growth, respectively. If all crystallites were aligned perfectly in the same direction, this ratio would be unity. The smaller this ratio, the wider the angular distribution of crystal orientations present in the film. R_L is shown in Figure 5.4b as a function of the power density p of the illuminating laser during growth and follows approximately $R_L(p) = 1 - e^{-p/p_0}$ with the threshold power density $p_0 = 3.8W/cm^2$. This demonstrates that for tetracene moderate illumination densities on the order of the threshold power density are sufficient for LDSA and induce significant anisotropy.

To relate R_L and the measurements presented in Figure 5.4a with an azimuthal probability distribution of $\mathbf{D}_+$ orientations (and thus also crystal orientations) we assume a Gaussian distribution in the angular crystallite orientation. We model the intensity of the luminescence signal on the detector behind a polariser in accordance with Equation 2.6 by

$$I \propto \left|\mathbf{e}_p \cdot \mathbf{D}_+\right|^2 \tag{5.2}$$

$$= cos(\phi - \varphi)^2 \left|\mathbf{D}_+\right|^2 \tag{5.3}$$

with $\mathbf{e}_p$ being a unit vector representing the polarisation direction of the polariser, the polariser angle φ and ϕ the direction of $\mathbf{D}_+$ (Figure 5.5a) (A similar mathematical representation is also used to describe NEXAFS[1] measurements in terms of x-ray absorption instead

[1] near edge x-ray absorption fine structure

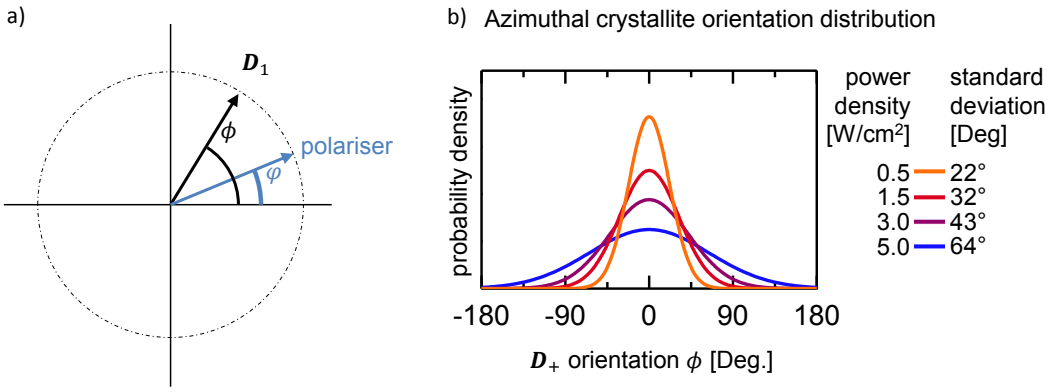

FIGURE 5.5: a) Illustration of $\mathbf{D}_+$ orientation angle ϕ and polariser angle φ as used in Equation 5.3. b) Angular crystallite orientation assuming Gaussian distribution of $\mathbf{D}_+$ to model measurements shown in Figure 5.4.

of visible transitions).[39,40]. Including a Gaussian distribution of the $\mathbf{D}_+$ orientations of the individual crystallites in Equation 5.3, it can be written as

$$I(\varphi) \propto \int_0^{2\pi} \frac{cos(\phi-\varphi)^2}{\sqrt{2\pi\sigma}} \left[e^{-\frac{(\phi+2\pi)^2}{2\sigma^2}} + e^{-\frac{\phi^2}{2\sigma^2}} + e^{-\frac{(\phi-2\pi)^2}{2\sigma^2}} \right] d\phi. \tag{5.4}$$

Here the 2π shifted replica of $e^{-\frac{\phi^2}{2\sigma^2}}$ are used to implement a Gaussian distribution with ϕ as angular coordinate.

The intensity calculated in Equation 5.4 allows us to simulate the luminescence intensity in dependence of φ (measured values and simulations shown in Figure 5.4a) and to conclude on the corresponding R_L. In the measurements we find $R_L \simeq 0.72$ is reached at $p \simeq 5W/cm^2$ which corresponds to $\sigma \approx 22\,^\circ$ in the described model. We extrapolate R_L to reach values above 0.9 ($\sigma \simeq 10\,^\circ$) at $p > 10W/cm^2$.

5.2.2. Crystal Structure Analysis and Optical Twinning

Another way to address the azimuthal orientation in thin films is to analyse them by means of x-ray diffraction. All presented measurements were performed at the I07 beamline located at the *Diamond Light Source* at an energy of 13 keV.[79] From XRR diffraction data (Figure 5.6) we conclude that there are two polymorphs present in the sample. While the Bulk polymorph, originally identified by Holmes *et al.*[166] in single crystals has also been extensively studied in thin films before,[165,167,168] the second polymorph has not attracted attention equally.[165,169,170] The increased out-of-plane lattice spacing suggests that the second polymorph is an surface induced phase[70] and therefore only occurs in thin films. To our knowledge the full set of unit cell parameters has not been derived from experimental data before. In order to determine also the unit cell parameters of this second polymorph, which we label *thin film phase* (TF) we record the grazing incidence

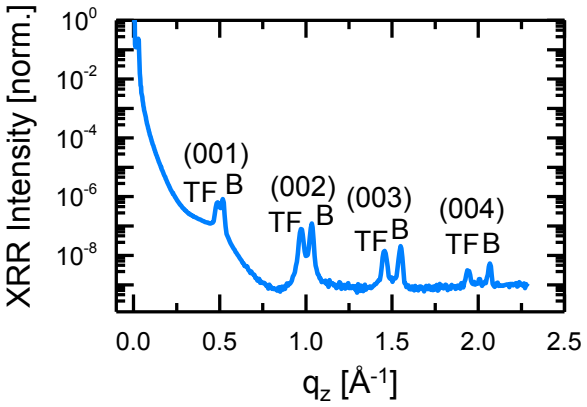

FIGURE 5.6: X-ray reflectivity curve of a 20 *nm* tetracene thin film grown in the dark. Reflections of bulk (B) and thin film (TF) phase show similar intensities.

	a [Å]	b [Å]	c [Å]	α [°]	β [°]	γ [°]
Tetracene						
Bulk [166]	6.066	7.837	13.010	77.13	72.12	85.79
Bluk (fit)	6.0(5)	7.8(4)	13.0(9)	76.(6)	72.(3)	85.(7)
Thin film (fit)	5.9(3)	7.5(6)	14.1(1)	80.(4)	68.(3)	89.(9)
Pentacene						
Bluk [68]	6.06	7.90	15.01	81.6	77.2	85.8
Thin film [68]	5.92	7.54	15.63	81.5	87.2	89.9

TABLE 5.1.: Unit cell parameters of tetracene as found in literature and resulting from structure calculations in the context of this thesis. For comparison, also the unit cell parameters of pentacene are given to highlight the structural similarities between bulk and thin film structure comparing different acene molecules.

x-ray diffraction (GIXD) map of a film grown in the dark (no azimuthal texture). Using the formalism presented in references [103] and [102] we are able to parameterise the TF unit cell with the unit cell parameters given in Table 5.1. The extracted parameters are plausible especially in comparison with what has been found for thin film structures and surface induced phases for other acene molecules. [68]

As we do not have data of the atomic coordinates of tetracene within this newly determined TF unit cell, we base the following analysis of orientational distributions on the bulk phase determined by Holmes *et al.*. [166] Their analysis on single crystal data allows to precisely determine not only the unit cell parameters but also atomic positions and the orientation of the molecules within the unit cell (structure in Figure 5.2). Therefore, the orientational relations between $\mathbf{D}_+$ and the in-plane unit cell axes a and b are known and can be used to correlate optical and structural thin film properties.

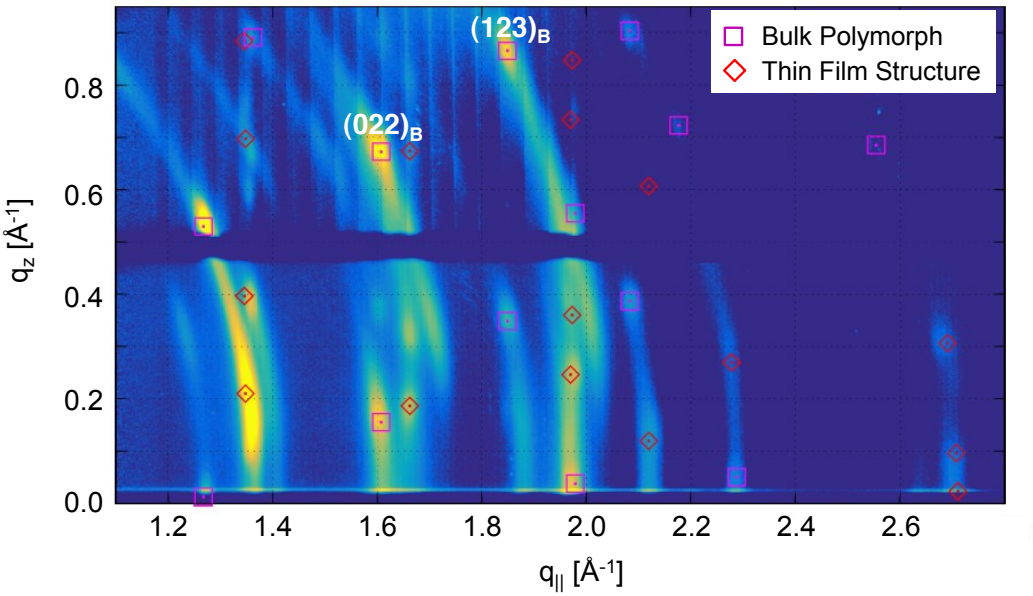

FIGURE 5.7: GIXD diffraction map of a tetracene thin film consisting of two closely related crystal polymorphs: bulk and thin film phase grown in the dark. The two highlighted reflections (022) and (123) of the bulk phase are used to characterise the anisotropy in illuminated samples.

In order to analyse anisotropy through GIXD measurements, we apply a formalism similar to what is known form single crystal diffraction (Details in Section 3.3.5). We rotate the sample while monitoring the grazing incidence x-ray diffraction (GIXD) intensities of selected Bragg reflections as illustrated as ω-scan in Figure 5.8a. Typical examples of two azimuthal intensity profiles are given in Figure 5.8b of the (022) and (123) reflections. We find four unit cell orientations in the film that all share a common orientation of the in-plane component of $\mathbf{D}_+$ (Figure 5.9). The ab-plane of the molecular unit cell forms the contact plane with the underlying substrate. Through 180° rotations perpendicular to the in-plane $\mathbf{D}_+$-axis in the substrate surface, the angles between the observed intensity maxima in the ω-scan (Figure 5.8) are defined. Additionally, there are also 180° in-plane rotated versions of the two cell orientations, which obviously fulfil the same condition with their $\mathbf{D}_+$ axis pointing in the same directionn.

The azimuthal angle under which the reflections occur can be derived as described in Section 3.3.5. In Figure 5.10 it is graphically motivated through the intersecting angle of the projection of (022) and (123) lattice planes corresponding to the rotated structures in the substrate plane. The *a*-axis of the two cells is tilted by 4.35° with respect to the common optical axis $\mathbf{D}_+$. Cuts for the (022) plane in red and (123) plane in blue highlight the azimuthal difference angles ϕ_{022} and ϕ_{123}. Since the (022) plane is parallel to the *a*-axis in the *ab*-projection we find $\phi_{022} = 2 \cdot 4.35° = 8.7°$. Similarly we find $\phi_{123} = 59.6°$ for the (123) planes of the two cells.

We find the laser polarisation plane to be aligned perpendicular to the common $\mathbf{D}_+$-axis,

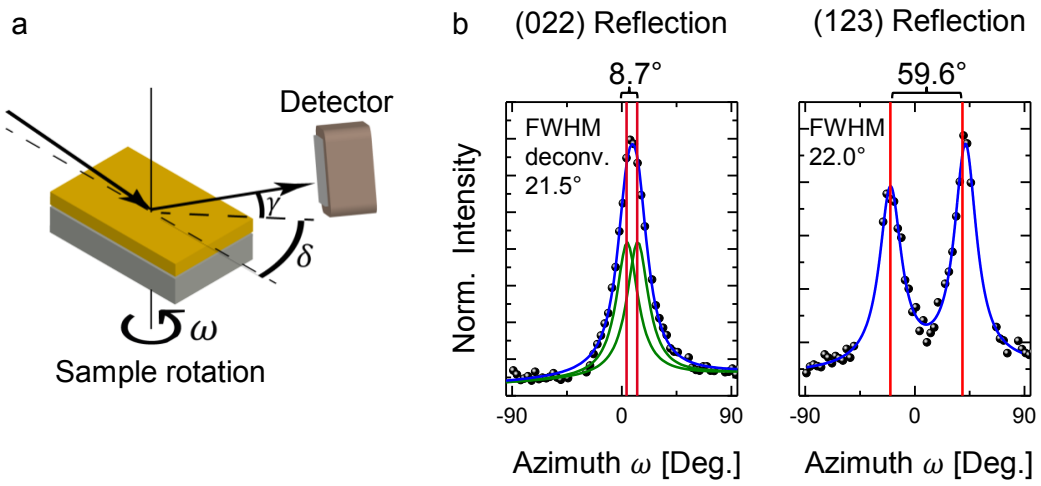

FIGURE 5.8: Determining the azimuthal distribution of crystallite orientation by means of x-ray diffraction. a) Measuring the azimuthal intensity dependence of grazing incidence x-ray diffraction (GIXD) reflections by rotating the sample detector fixed detector position (ω-scan). b) ω-scans of tetracene (022) and (123) reflections of tetracene. The vertical lines indicate the expected peak positions based on the optical twin model.

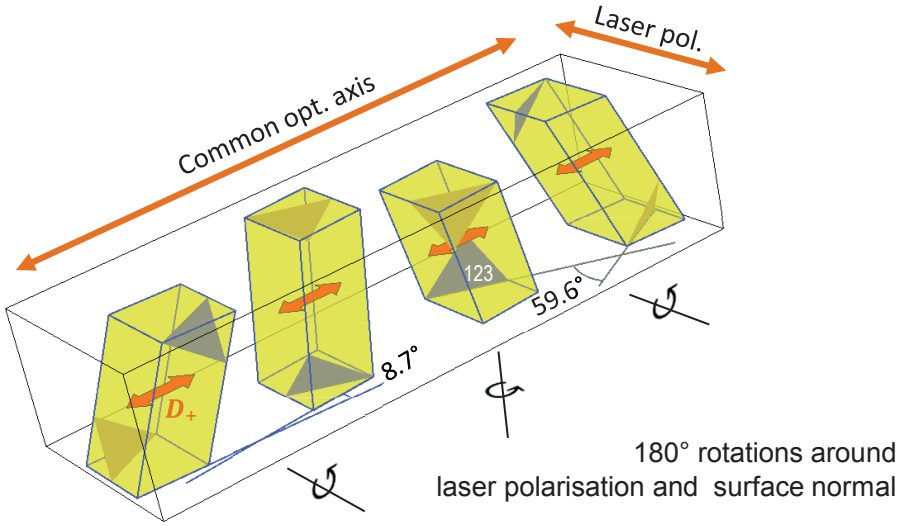

FIGURE 5.9: Illustration of the four observed unit cell orientations with respect to laser illumination during growth

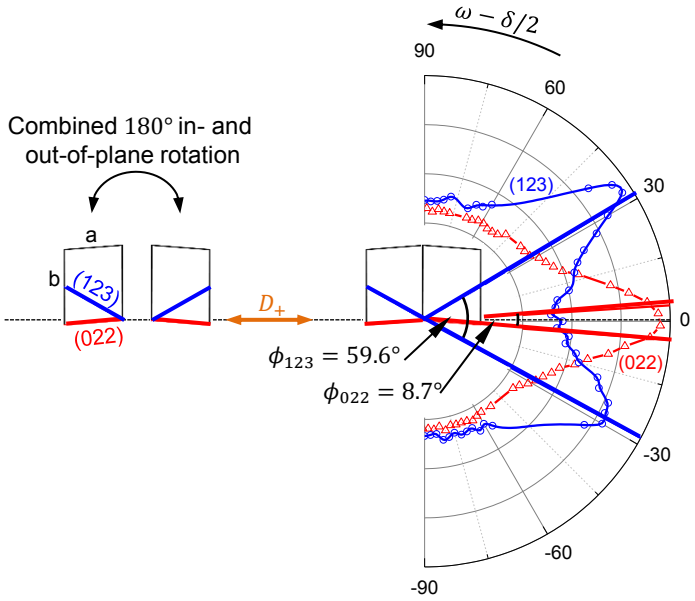

FIGURE 5.10: Azimuthal GIXD intensity of (022) and (123) reflections directly related to real space orientation of the tetracene unit cell and its optical twin.

thus, we label this axis the *optical twin axis*. Crystal twinning is a well-known phenomenon in crystallography[171] that characterises the structural relation between neighbouring crystal grains of the same crystal species in terms of a *twin law* describing orientation, chirality and contact relations. In analogy to this we define *optical crystal twins* as the set of crystal orientations that share a common alignment of a defined optical transition in molecular crystals.

From the width of the reflection (mosaicity $\sim 22\,°$) we deduce an angular spread of the $\mathbf{D}_+$ distribution with a standard deviation $\sigma \approx 10\,°$, for the (022) reflection the width is derived through deconvolution. Considering the difference in probe volume between the x-ray ($\sim 0.25\,mm^2$) and optical ($\sim 4\,mm^2$) setups and the inhomogeneous degree of alignment due to the Gaussian intensity profile of the illuminating laser, the angular spreads determined by the two methods are in good agreement ($\sigma_{\text{opt}} \sim 2\,\sigma_{\text{xray}}$). σ_{xray} (smaller value) represents best the capabilities of LDSA at $5\,W/cm^2$ due to the smaller corresponding probe volume reflecting the increased homogeneity in the illumination density in this area.

5.3. Crystallite alignment through opto-thermal reorganisation

5.3.1. Mechanism

We consider two models to describe the mechanism behind LDSA: one is based on optical birefringence conveying angular momentum[172–174] and the other on opto-thermal re-organisation. In birefringent nematic liquid crystals (NLCs) external optical fields can induce an optical torque (optical Fréedericksz effect) that aligns the slow optical axis parallel to the field.[157,158,175] Based on the optical constants for tetracene derived by Tavazzi et al.[162] we find, however, the fast optical axis to be aligned with the external optical field in the LDSA grown samples. While the NLCs do not necessarily absorb the exciting light, tetracene on the contrary absorbs a significant portion of the light. Therefore, we hypothesise opto-thermal re-organisation to be the origin of the observed alignment. Using the optical constants[165] of tetracene thin films, we deduce that about 10% of the incoming $2.32\,eV$ light is absorbed in a film of 25 nm thickness. Based on this figure we rationalise that every molecule in the film is excited on the millisecond time scale, given an irradiating power density of $5\,W/cm^2$ ($1.3 \cdot 10^{19}$ photons s^{-1} cm^{-2}) at $2.32\,eV$. Since in tetracene crystals singlet fission plays a dominant role, the quantum efficiency of S_1 luminescence is extremely low (0.002 to 0.009)[176] and non-radiative processes such as internal conversion lead to a significant energy transfer into tetracene crystallites. The opto-thermal re-organisation is based on the strongly anisotropic absorption where more energy is absorbed in crystallites that are oriented with their $\mathbf{D_1}$ axis parallel to the external laser field. This suggests that crystallites in this orientation are more mobile and more likely to dissolve or re-orientate than those that are oriented perpendicular. In these terms, the energetic landscape induced by the laser may be described as a pseudo potential with a minimum for crystallites that are oriented such that their $\mathbf{D_+}$ axis lies perpendicular to polarisation plane of the exciting light, as schematically illustrated in Figure 5.11. The impact of this effect at illumination intensities studied here is limited to small crystallites only, because closed monolayers and large crystallites in fully grown 25 nm thick films do not re-orientate. Therefore, LDSA has to be applied during thin film growth.

5.3.2. Applicability to other molecular materials

LDSA can in principle also be applied to molecules other than tetracene that are known to form crystalline thin films and show the suitable optical properties. Of crucial importance in this context are:

- Pronounced anisotropic, spectrally separated absorption properties (e.g. sufficiently wide Davydov splitting in case of non-primitive unit cells).
- Suitable orientation of the excitonic TDMs in the molecular crystal, so that azimuthal

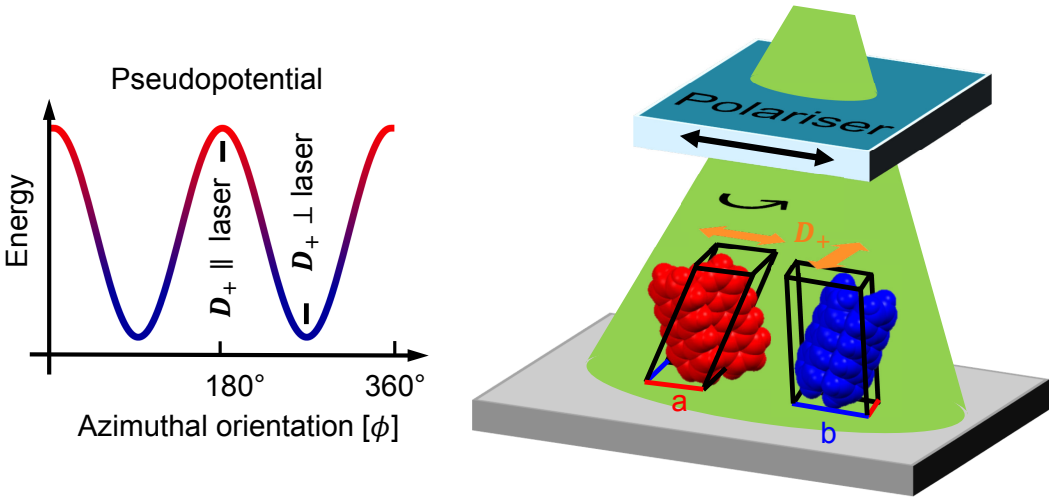

FIGURE 5.11: Schematic illustration of the opto-thermal re-organisation mechanism. Molecular crystallites, that absorb resonantly (red) are in a less favourable position in the pseudo potential than those, that do not absorb the incoming light. Small molecular crystallites therefore rotate until they do not absorb resonantly any more.

anisotropy can be induced through resonant illumination.

- Availability of intense monochromatic light source with photon energy matching the transition energy.

Assuming inert substrates with low surface energies, planar molecules tend to form crystals in an upright standing manner. Under this condition, LDSA works for molecules that have TDMs aligned perpendicular to their long molecular axis (e.g. polyacenes). For many rod-like molecules however the TDMs are oriented along the long molecular axis. Thus, the according excitonic transitions cannot selectively be excited at normal incidence.

5.4. Conclusions

In summary, we present a study on the control of anisotropy in organic thin films through the presence of optical fields during growth. Since light can be formed, shaped and applied very precisely, this method opens up new ways to pattern organic thin films as demonstrated above. The specific potential of LDSA is the possibility to pattern organic molecular thin films and to align molecules within these films simultaneously without the need of alignment layers or photoactive groups such as azobenzenes or groups for photo-crosslinking. We demonstrate the enhanced degree of structural order and anisotropy in films grown by LDSA through crystallographic and optical methods. Beneficial effects on the directed electric charge due to the azimuthally aligned crystal grains in LDSA grown films are expected. Furthermore, LDSA will enable the design of organic light emitting

diodes (OLEDs) emitting polarised light and potentially lasing, light emitting organic field effect transistors.[177,178] We anticipate our work will help advance the surface-by-design approach in order to fabricate organic surface structures as used in photonic applications, such as optical Bragg gratings, planar waveguides, distributed feedback lasers and surface patterns for optical meta-surfaces through the ability to locally pattern the dielectric constants of the organic thin film.

6

Controlling PTCDI-C_8 Thin Film Growth through Rapid Thermal Cycles

In the previous studies we used light as a control parameter. Here, rather than using light to control organic thin film growth, we aim to explore possibilities to tailor thin film growth through manipulating the morphology of individual molecular monolayers during the thin film formation processes. For organic material systems thin film growth is often governed by kinetic processes far from equilibrium that define the island density during individual monolayer growth.[179,180] The two most important experimental parameters are the substrate temperature and molecular deposition rate that in turn govern diffusive processes and the availability of ad-molecules[1].
The island density $N_{\max}$ in the film that is formed during the nucleation phase of a growing monolayer is described by

$$N_{\max} = \eta N_0 \cdot \left(\frac{4R}{N_0 \nu_0}\right)^p \cdot exp\left(\frac{E_{\text{nuc}}}{k_B T}\right) \tag{6.1}$$

with a prefactor η, a scaling exponent p, the growth rate R, the attempt frequency ν_0, the nucleation energy E_{nuc} and the number of surface sites per unit area (for PTCDI-C_8 $N_0 = 2.27 \cdot 10^{14}$ molecules/cm^2).[91,110,181] The energy barrier E_{nuc} bundles various energy barriers such as the diffusion energy E_D, the attachment energy E_a and the binding energy E_b.[110] The scaling exponent p is a function of the critical nucleus size i^* and the maximum number of monomers in an unstable cluster. Considering Equation 6.1, raised growth

[1] Unbound, solitary molecules on top of the thin film that are not integrated into solid state domains yet (see Chapter 2.3).

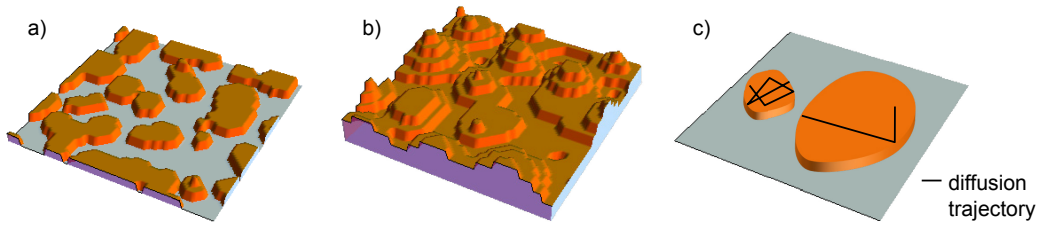

FIGURE 6.1: a,b) Surface morphology evolution and terrace formation through the presence of an additional step edge barrier E_{ES}. c) Schematic illustration of differently sized surface islands and simplified diffusion trajectories of a diffusing molecule on top. Within the same number of diffusion steps, the diffusing molecule on the small island approaches the step-edge much more often than on the large island. Assuming the same interlayer transport probabilities for an isolated step-edge diffusion approach, the overall downward transport rate significantly depends on the island size through differing number of step-edge approaches.

rates and lowered temperatures yield increased island densities. Further, high molecular diffusivity (small E_D and thus small E_{nuc}) leads to a low island density.

In multilayer[2] thin film growth there is an additional energy barrier for interlayer diffusion (also step-edge diffusion barrier or Ehrlich-Schwoeble barrier, see Chapter 2.3) which reduces interlayer transport and potentially causes surface roughening during growth (see Figure 6.1). Considering homo-epitaxial growth with $i^* = 1$, one may picture this roughening in a mean free path model.[27,182] Given that a freshly deposited molecule attempts a certain number of diffusion steps before it reaches its final position and integrates into the solid state thin film, the mean free path of diffusion also defines the initial island density in the first layer. Molecules that are deposited on top of an island can diffuse to the edge of the island and potentially overcome it and integrate into the underlying layer within the mean free path length. As soon as islands coalesce the length scale on top is significantly larger than the mean free path of the molecules. Therefore, second layer islands are formed, resulting in layer-by-layer growth. The existence of additional step edge barriers results in reduced interlayer transport rates and thus causes reflection of the diffusing molecule on the step-edge, leading to second layer nucleation even before coalescence (see Figure 6.1c). On small molecular islands the diffusing molecule approaches the step-edge several times so that probability of interlayer diffusion eventually increases compared to larger islands. As will be discussed later in Chapter 6.4, sufficient interlayer transport is one of the key criteria for layer-by-layer thin film growth.

The described processes can be expressed in Arrhenius type rates

$$\nu = \nu_0 e^{-\frac{E_D}{k_B T}} \tag{6.2}$$

$$\nu_S = \nu_0 e^{-\frac{E_D + E_{ES}}{k_B T}} \tag{6.3}$$

with the diffusion rate ν for in-plane diffusion and ν_S for the reduced interlayer diffusion

[2] Several molecular monolayers stacked on top of each other.

across step edges (ν_0 being the attempt frequency[3]). Given the temperature dependence in Equation 6.2, it is obvious that higher temperatures result in higher diffusion rates which go hand in hand with an increase in the mean free path of diffusion and lead to the following dilemma:

- High island densities and high molecular diffusivity are mutually exclusive in conventional thin film growth.

On the one hand, high island densities that correspond to many small islands are beneficial for interlayer transport and layer-by-layer growth. On the other hand, high molecular diffusivity increases the mean free path of diffusion and the probability to overcome the step-edge barrier and is thereby also favourable for layer-by-layer growth. In the following, we discuss a method that can be used to overcome the dilemma in a way that has not been applied to soft matter thin films before.

Inspired by the work of Rosenfeld *et al.* on inorganic, homo-epitaxial systems, we use the *concept of two mobilities* to decouple initial island densities and diffusive processes in advanced stages of monolayer growth.[27,28,182] The concept is based on the idea that differing surface diffusion conditions (e.g. differing deposition rates, energy barriers or temperatures) at distinct stages during monolayer growth can strongly impact the resulting morphology of the multilayer thin film.
To be able to combine the beneficial aspects of high surface diffusivity and high island densities regarding surface smoothness, dynamic control over the surface temperature is necessary to ensure the formation of high island densities in the early stage of monolayer growth and high diffusivities during later stages. At this point, it is helpful to recall the three phases scheme of layer-by-layer growth from literature (Figure 6.2).[29] The nucleation phase which is the first phase of monolayer growth lasting up to coverages of 5% to 10% defines the island density that stays almost constant throughout the lateral growth phase and reduces rapidly during coalescence. Therefore, the short period of nucleation essentially defines the island density in the growing monolayer (Figure 6.2, top). An increased mean free path for diffusive processes in the lateral growth phase ensures higher probabilities of ad-molecules to descent from surface islands (interlayer transport).
Based on the behaviour described above, a growth recipe for smooth thin film may be formulated as follows:

- At the beginning of growth of each individual monolayer, a short low temperature period seeds the initial island density.
- High temperatures during the remaining time of monolayer growth ensure high surface diffusion rates.

From this recipe we deduce a temperature scheme during growth as shown in Figure 6.2. We choose a (high) base temperature during lateral growth and coalescence phase in a

[3] Some authors use different attempt frequencies for in-plane and interlayer diffusion equations.[183] Following ref. [184], they are assumed to be the same for reasons of simplicity.

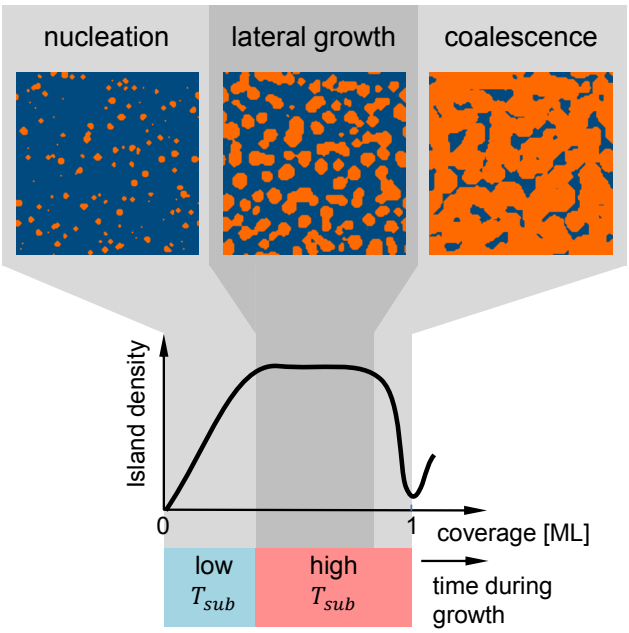

FIGURE 6.2: Three phases of monolayer growth: nucleation, lateral growth and coalescence. The growth phases are highlighted in a prototypical shape island density evolution of a growing monolayer. To increase the island density in the film, the sample is cooled down during the nucleation phase.

way that it matches the optimal growth conditions in conventional thin film growth. To enhance layer-by-layer growth, the substrate is cooled rapidly down during the nucleation phase so that the island density is abruptly increased. Thus, we are able to combine high island densities and high molecular diffusivity during monolayer growth.

6.1. Theoretical Case Study

To simulate the influence of temperature modulations on the surface morphology, a phase-field model described in Chapter 3.7 and Appendix C has been developed and is used in the following. Here we discuss one simulated growth run at constant temperature of $T = 300\,K$ ($E_D = 450\,meV$,$E_{ES} = 100\,meV$) and a second growth run where the temperature is lowered to $T = 230\,K$ for the first 10% of each monolayer growth cycle. Otherwise using the same parameters. Snapshots of the qualitative[4] results comparing the growth with and without temperature modulations are presented in Figure 6.3. The seeding of a high island density through the thermal cycle is well captured in the simulation of the thin film growth using temperate modulations. The direct comparison between the two films just after and before the next thermal cycle is instructive. While the film grown

[4] As anisotropies in the island shape are not yes captured in the simulations, we do not directly compare experimentally grown PTCDI-C_8 films to the simulations.

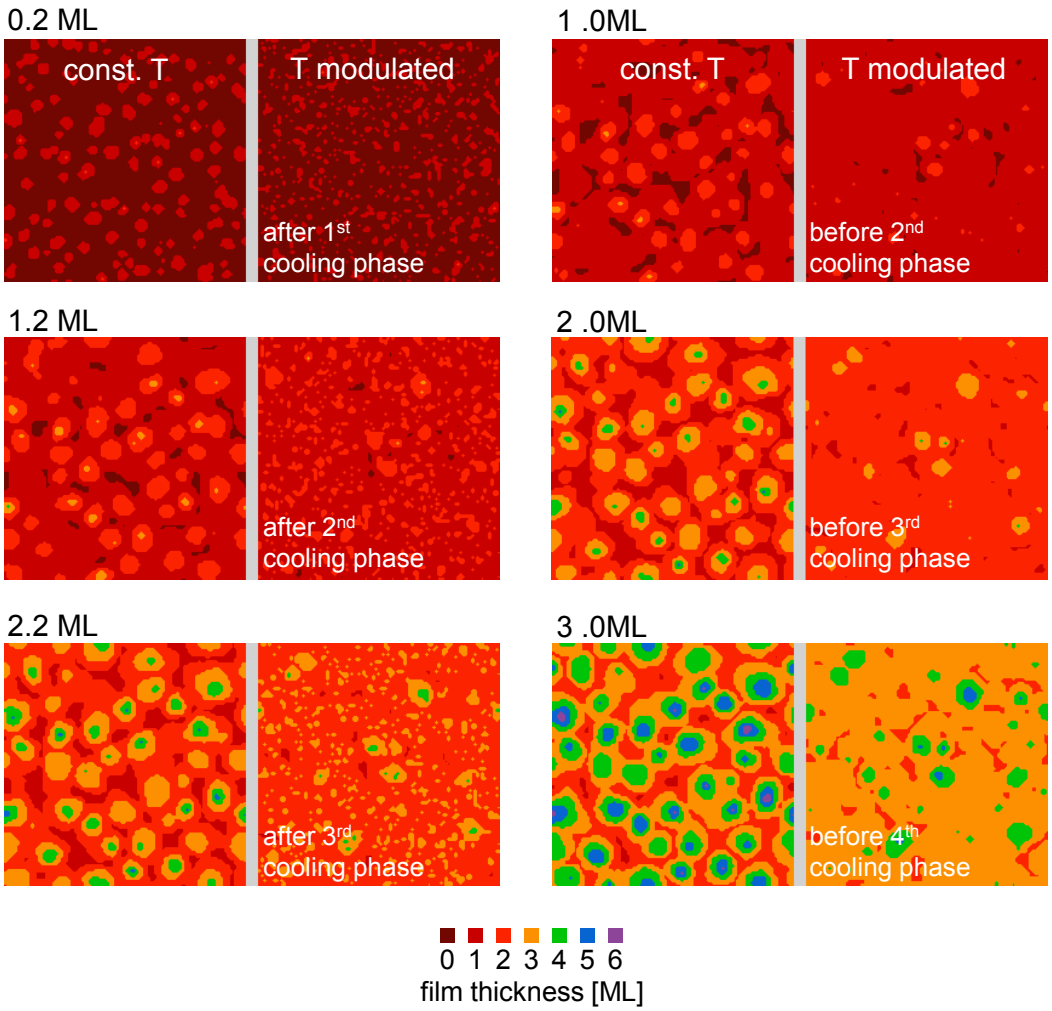

FIGURE 6.3: Comparison between surface morphologies resulting from phase field simulations. Shown are snapshots of $\Phi(t)$ just before and after the cooling cycle. Left: film grown at constant temperature; right: film grown with temperature modulations. The simulated area covers 100 x 100 lattice sites for each film.

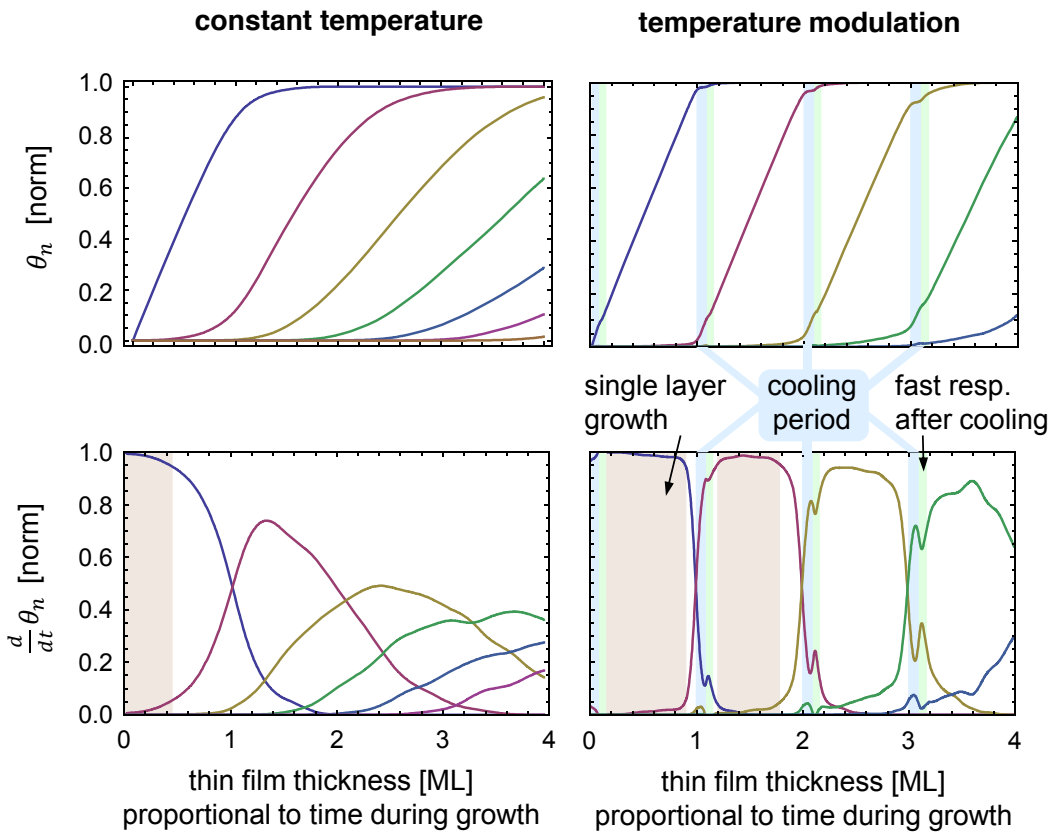

FIGURE 6.4: Simulated individual layer coverages θ_n and filling rates $\frac{d\theta_n}{dt}$. Left: growth at constant temperature; right: growth under temperature modulation. The grey shaded areas indicate single-layer-growth (95% threshold) and the cooling periods are highlighted in blue.

at constant temperature roughens over time, the temperature modulated film shows a much higher filling of the present ML.

To evaluate the simulated results thoroughly, we can follow the filling of the individual monolayers (coverages $\theta_n(t)$) over time as well as the filling rates $\dot{\theta}_n = \frac{d\theta_n}{dt}$. In Figure 6.1 the coverages and rates are presented as a function of total film thickness which is proportional to the time since the onset of molecular deposition with constant rate. Comparing how the individual monolayers fill up over time reveals that under the chosen growth conditions several layers fill up simultaneously when keeping the temperature constant during growth. As the substrate is initially flat, this effect becomes more evident during the filling of higher monolayers. Looking at the film simulated with temperature modulations during growth, we find that layers fill up much more consecutively. The difference between the two simulations is even more visible in rates $\dot{\theta}_n$ (Figure 6.1, bottom). $\dot{\theta}_n = 1$ indicates that only a single monolayer is growing at the respective point in time. For strict layer-by-layer growth, this should be the case at least during the lateral growth phase. For the film grown at constant temperature this growth mode can only be observed

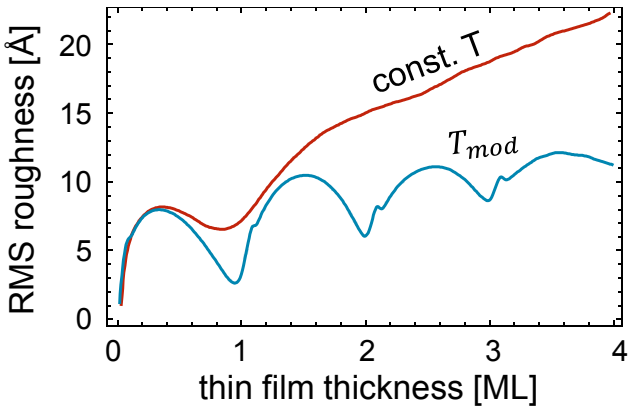

FIGURE 6.5: RMS surface roughness evaluation during thin film growth. In the simulation at constant temperature the surface continuously roughens after the second monolayer whereas the surface roughness breaks down under temperature modulations for each consecutive monolayer.

in the first layer (here we apply a 95% threshold) while it is also present in the second layer for the temperature modulated film.

During the cold phase[5], after layer n is almost completely covered we find an increased nucleation of islands in the subsequent monolayer $n+1$. When switching back to the high temperature some of these island dissolve again, thereby increasing the ad-molecule density (Equation 3.25) to its new equilibrium value. Simultaneously, we find a sharp increase in $\dot{\theta}_n$. Numerically this behaviour is based on the temperature dependent equilibrium value of u in Equation 3.25. Physically this can be interpreted as *Ostwald ripening*. The occurrence of *Ostwald ripening* at this point indicates that the growth temperature was chosen above the optimum value for maximised layer-by-layer growth.[182]

The root-mean-squared (RMS) surface roughness is evaluated to analyse the surface morphology.[90] In Figure 6.5 the RMS roughness for the two discussed simulated growth runs are shown. After the deposition of the first monolayer the roughness reduces, indicating the coalescence of islands in the film before a new layer is formed. From the second monolayer onwards, the behaviour in the two simulations differs significantly: In the case of constant temperature, the surface contentiously roughens while under modulated temperature the smoothening associated with the filling of the second and third monolayer is visible. These roughness oscillations indicate pronounced layer-by-layer growth.[90]

[5] In the simulation we use two discrete temperatures, rather than increasing or decreasing temperature profiles.

6.2. Experimental Realisation

We apply the *concept of two mobilities* to thin film growth of the molecular semiconductor PTCDI-C_8 (N,N'-Dioctyl-3,4,9,10-perylenedicarboximide), a perylene derivative that is known to produce high quality thin films of several monolayer thickness and which has been used in detailed *in-* and *ex situ* growth studies before.[102,110,185,186] We grow on Si wafers with native oxide layer and do not employ a cooling cycle during the nucleation of the first monolayer as the the island density is already significantly increased compared to PTCDI-C_8 homoepitaxial growth due to the underlying silica surface.[110]

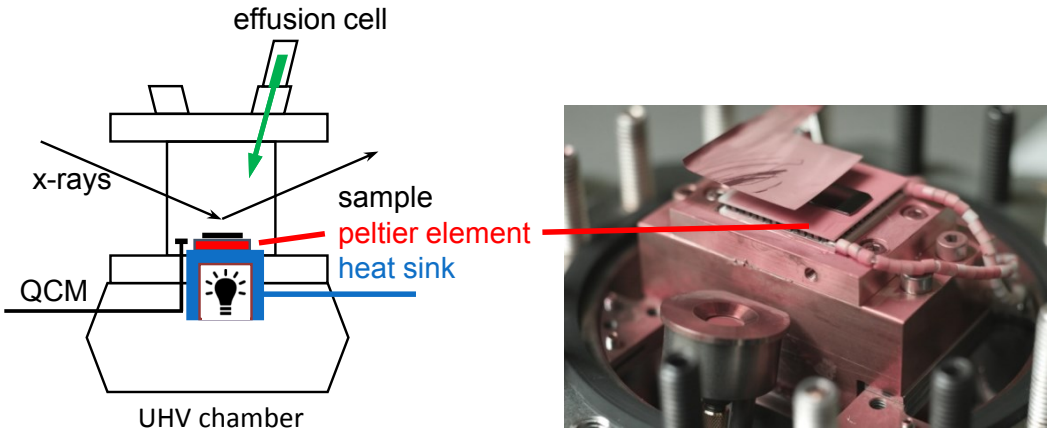

Figure 6.6: Sample holder with integrated Peltier element to realise rapid thermal cycles and heat-sink for thermal stability designed in the framework of this thesis.

It is challenging to synchronise the cooling cycles to the nucleation phase of the individual monolayers since total film thickness measured by a quartz crystal micro-balance (QCM) is not a sufficient measure. The synchronisation can be achieved by making use of real-time, *in situ* x-ray diffraction experiments monitoring the anti-Bragg intensity (see Section 3.3.3). The local maxima of these growth oscillations can be used to trigger the cooling cycles. An exemplary anti-Bragg signal together with the activated thermal cycles is shown in Figure 6.7.

From an experimental point of view, steep substrate temperature modulations are extremely challenging. In order to realise heating and cooling rates in the order of 100 $K\,min^{-1}$, we designed a Peltier element based sample holder that is shown in Figure 6.6. While the substrate with a small thermal mass is attached to the one side of the Peltier element (*Eureca, Kryotherm, Typ: TEC1H-30-30-44/80-G*, usable up to 200°C), the other side is attached to a copper heat sink with comparably high thermal inertia. Depending on the polarity of the electrical current through the Peltier element, the sample can be heated up or cooled down with steep temperature gradients. Additional low frequency temperature control of the heat sink ensures a constant temperature of the backside of the Peltier element.
As all involved materials (Cu, Si and Al_2O_3) feature strongly differing thermal expansion

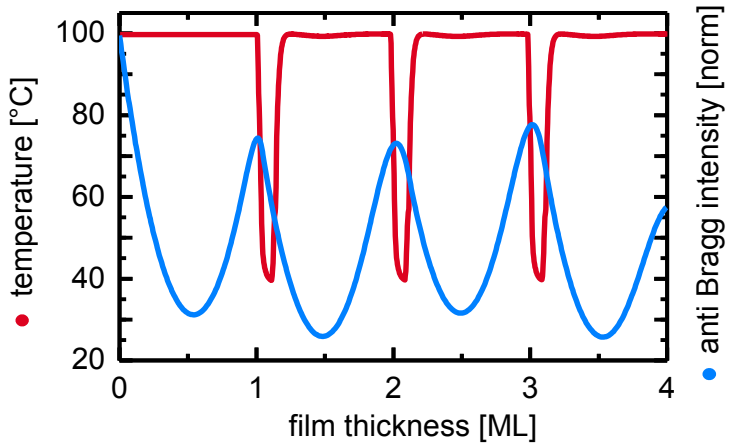

FIGURE 6.7: Temperature cycles triggered by growth oscillations to cool the substrate surface during each nucleation phase for individual monolayers. Blue: anti-Bragg intensity; Red: Temperature profile;

coefficients[6], great care has to be taken to ensure strong bonding between the individual components providing good thermal conductivity throughout numerous cycles resisting the thermally induced stress. Here we used the two-component adhesive *Polytec EC 101*. Especially when applying steep heating rates, great care has to be taken that the substrate temperature is regulated in a way that it does not overshoot and thereby re-evaporates the so far deposited molecular thin film. The shutter, which can also be seen in Figure 6.6, is motorised to allow several experiments on the same substrate which increases comparability and throughput. This is especially relevant for time limited synchrotron experiments.

[6] Cu: $16.5 \cdot 10^{-6} K^{-1}$;Si: $2.56 \cdot 10^{-6} K^{-1}$; BK96 (alumina): $4.5 - 6.5 \cdot 10^{-6} K^{-1}$ [187]

6.3. Controlling Island Densities and Interlayer Transport

The *in situ* experiments were performed at the *ESRF ID10* beamline (energy: 14 keV, beam dimensions: 300 μm horizontal x 10 μm vertical) and a summary of the experimental results is presented in Figure 6.8. We compare a film grown at 100 $^{\circ}C$ constant substrate temperature with a second film that has been grown under temperature modulated (T_{mod}) conditions with the same base temperature of 100 $^{\circ}C$ and cooling cycles down to 40 $^{\circ}C$ during the nucleation phase of each monolayer (for temperature scheme, see Figure 6.7). Visualising the GISAXS signal, we find the $q_{\parallel}$ splitting to be almost conserved over time in the T_{mod} film compared to the film grown that 100 $^{\circ}C$. Additionally, the intensity modulation of the diffusely scattered signal is significantly more pronounced for the T_{mod} film. Vanishing intensity in this case corresponds to an ideally flat surface. Extracting the island density evolution from the $q_{\parallel}$ splitting for both films and from subsequent FFT-AFM measurements on additional samples (details in Section 3.5.1) reveals that the initial island density is conserved for higher monolayers (MLs) in the T_{mod} film.
Under static substrate temperature conditions a 15-fold increase in the island density is found in ref. [110] for $T_1 = 100\,^{\circ}C$ and $T_2 = 40\,^{\circ}C$ based on the scaling law in Equation 6.1 and $E_{\mathrm{nuc}} = 460 \pm 28\,meV$ for the growth of PTCDI-C_8 on PTCDI-C_8 . Through temperature modulations we observe an increase in the island densities by a factor 3.5 in the 2$^{\mathrm{nd}}$ ML, a factor 12 in the 3$^{\mathrm{rd}}$ and a factor 15 in the 4$^{\mathrm{th}}$ ML comparing the two discussed films. The value for the second monolayer highlights that we do not reach the island density expected for constant 40 $^{\circ}C$ growth but rather reflects an effective value for 70 $^{\circ}C$. In the third and forth monolayer the increased island densities in the underlying layers has an auxiliary effect.

Regarding the shape of the island density evolution over time for the film grown under temperature modulations, we observe the characteristics of nucleation, lateral growth and coalescence phase of layer-by-layer growth (see also Figure 6.2). For the film grown at constant temperature the island density drops continuously by roughly half an order of magnitude per grown ML and does not allow to clearly identify the growth phases for each monolayer.

Looking at the anti-Bragg signal for the two films, the shape of the growth oscillation suggests a more pronounced layer-by-layer growth (the signal is less damped) for the film grown with temperature modulations. Applying the rate equation model (see Section 3.3.3)[8] to the data sets in Figure 6.8 unravels the individual layer coverages and the surface roughness during growth (also shown in Figure 6.8). We chose essentially the same parameter set to fit both films (see Table 6.1) only varying the critical layer coverages $\theta_{n,\mathrm{crit}}$ to allow for a direct comparison. While $\theta_{1,\mathrm{crit}}$ is the same for both films, $\theta_{2,\mathrm{crit}}$, $\theta_{3,\mathrm{crit}}$ and $\theta_{4,\mathrm{crit}}$ differ significantly between the two films. In the fit the growth rate for the first

[7] The oscillations for the 100 $^{\circ}C$ film are acquired at a q_z value that slightly differs from $q_{\mathrm{anti-Bragg}}$. This q_z-offset is accounted for in the fit.
[8] Using the TroFit software by P.Beyer *https://www.physik.hu-berlin.de/de/x-ray/downloads-1*

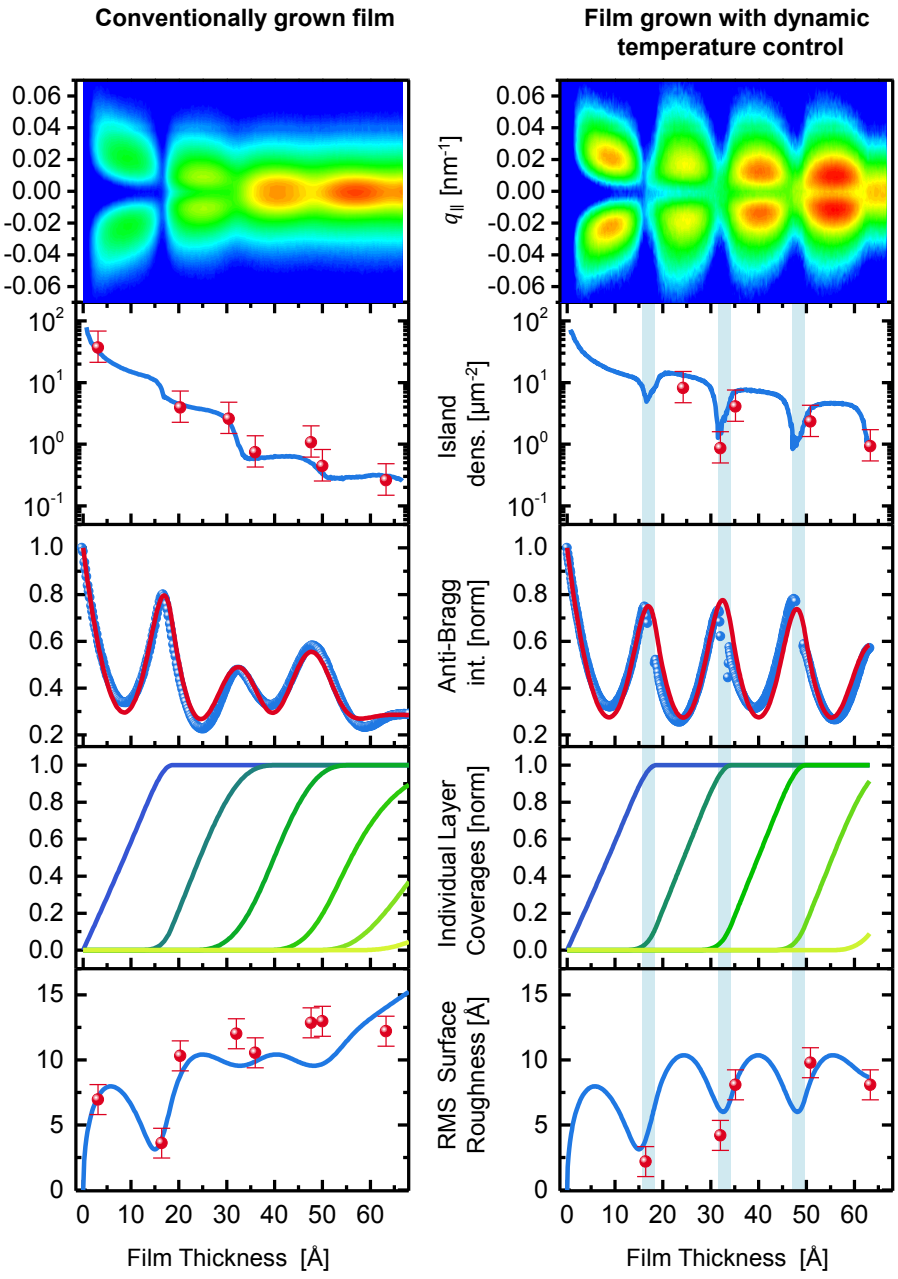

FIGURE 6.8: Diffuse scattering (GISAXS, top, false colour scale from blue to red) as a function of time allow to extract island densities evolution in the film. Simultaneous acquisition of the anti-Bragg[7] intensity enables reconstructing the out-of-plane surface evolution based on the analytical rate equation model (blue: measurement; red: fit). The two bottom panels show individual layer coverages and surface roughness extracted from the fits. The red markers represent AFM-measurements. Shown are two growth runs, one at constant substrate temperature (100 °C) and one grown under temperature modulations (100 °C to 40 °C).

Model parameter		
	const. 100°C	T_{mod}
$\theta_{1,\mathrm{crit}}$ [norm.]	0.67	0.67
$\theta_{2,\mathrm{crit}}$ [norm.]	**0.37**	**0.65**
$\theta_{3,\mathrm{crit}}$ [norm.]	**0.37**	**0.65**
$\theta_{4,\mathrm{crit}}$ [norm.]	**0.11**	**0.44**
R_1 [ML/Å$_{\mathrm{QCM}}$)]	0.0560	0.0560
R_n [ML/(Å$_{\mathrm{QCM}}$)]	0.0645	0.0645
layer spacing [Å]	20.7	20.7
q_z [Å^{-}1]	0.15026	0.15170

TABLE 6.1.: Critical layer coverages $\theta_{n,\mathrm{crit}}$ for succeeding layer nucleation resulting from rate equation model and parameters that are kept constant for fits of both films. We find a strong increase in critical coverages for all layers with preceding thermal cycle.

monolayer differs from the one of the succeeding ones reflecting the differing sticking coefficient of PTCDI-C_8 on silica compared to PTCDI-C_8 on PTCDI-C_8 .

From the non-equivalence in $\theta_{n,\mathrm{crit}}$ of the two films arises a difference in the filling behaviour of the individual layers. For the film grown at constant temperature, the third and forth monolayers are clearly starting to fill up while the preceding ML is not completely filled yet, indicating surface roughening. We demonstrate that it can be suppressed when controlling growth by temperature cycles synchronised to the nucleation phase. Different roughening behaviour is also evident in the RMS surface roughness that can also be extracted from the fits based on the rate equation model. The surface roughness decreases significantly when the second and third monolayers are completely filled (T_{mod} film), indicating a smooth surface and only little step edges on the surface. On the other hand, this periodic decrease in the RMS surface roughness is strongly reduced for the film grown at a constant temperature. Complementary to the surface roughnesses resulting from the rate equation model we additionally extracted RMS values from AFM images. Direct comparison between the two films reveals a reduction in the surface roughness by $\approx$ 40% for the T_{mod} film.

As mentioned above, complementary to the *in situ* scattering experiments, also *ex situ* AFM micrographs have been recorded to analyse the real space arrangement in the thin film (Figure 6.9). In Table 6.2 the individual layer coverages for the two films with a total thickness of 4.1 ML are given. While for the T_{mod} film the 4^{th} layer is essentially filled (97.4 %), there are still 10 % missing in the film grown at constant temperature and at the same time the fifth layer is already filled up to 20 %.

Images recorded after the cooling cycle highlight the seeding of an increased island density through the cooling phase. The images show the persistent influence of the cooling cycle on the island density as all images are recorded on samples that were heated to 100°C after the cooling phase.

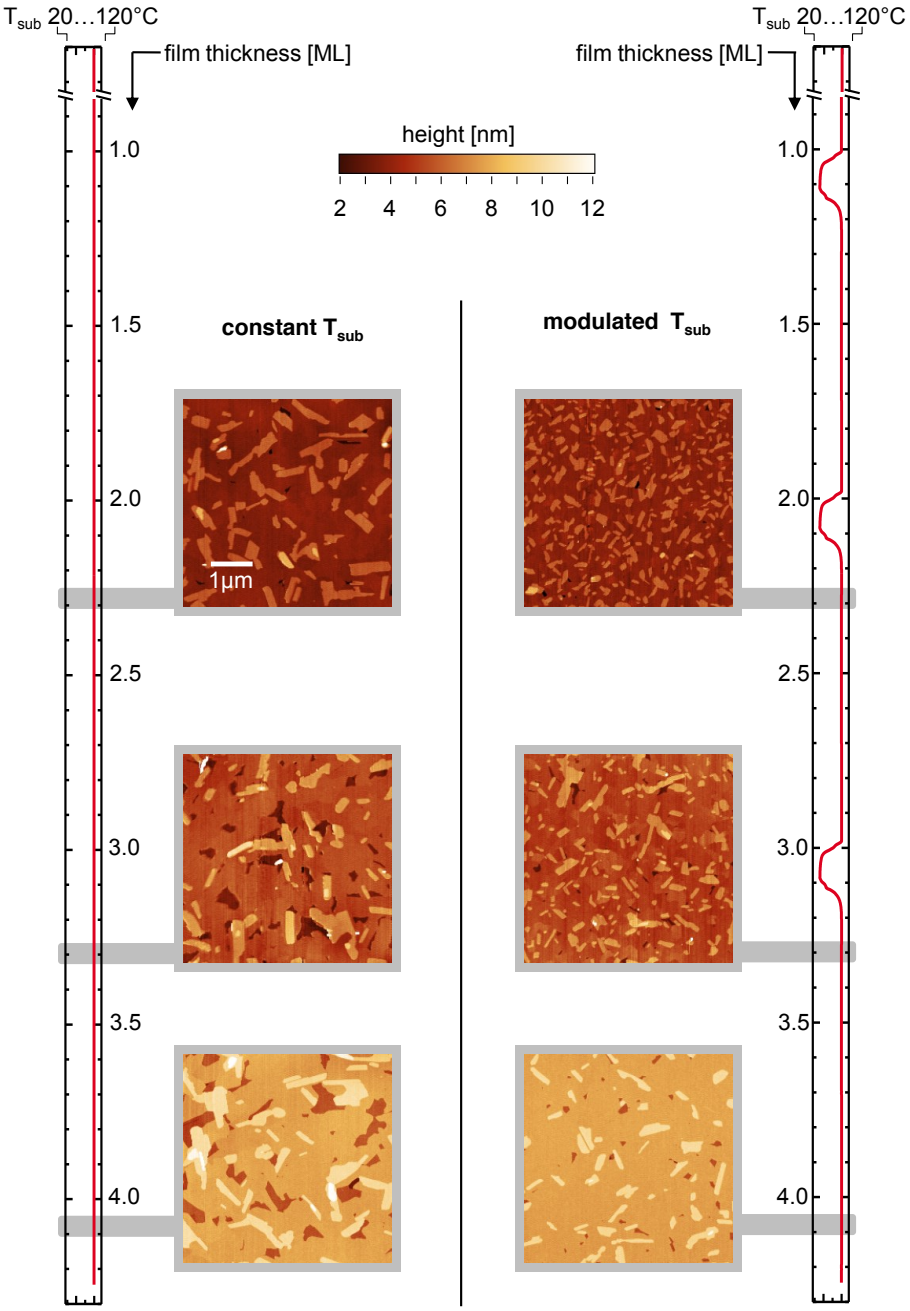

FIGURE 6.9: AFM micrographs ($5 \times 5\ \mu m$) of samples grown with and without temperature modulations. We observe increased nucleation densities and reduced surface roughnesses for samples that were grown using temperature modulations during growth. For first ML AFM micrographs, that are not affected by the temperature modulations, see Appendix A.3.1.

Monolayers coverages based on AFM

monolayer	const. 100°C	T_{mod}
1. ML	100 %	100 %
2. ML	100 %	100 %
3. ML	99.8 %	99.9 %
4. ML	89.6 %	97.4 %
5. ML	20.5 %	11.3 %
6. ML	1.4 %	0.5 %

TABLE 6.2.: Monolayer coverages extracted from AFM micrographs of films grown to a nominal thickness of 4 ML. See Figure 6.9 for raw images. There is roughly 10 % difference in the 4^{th} ML and 5^{th} ML which indicates the increased interlayer transport in films grown under temperature modulation.

6.4. Discussion

The presented experiments and simulations show that the growth of smooth thin films - and thus the thin film quality - can be enhanced through thermal cycles synchronised to the nucleation phase during monolayer growth. In order to understand the underlying mechanism of surface smoothing under conditions where kinetic processes dominate the morphology formation we focus on surface diffusion (Chapter 2.3) and discus effects of the in-plane diffusion[9] and interlayer transport on the resulting morphology separately. For perfect layer-by-layer growth ($E_{ES} = 0\,meV$ and high diffusivity), only one layer grows at a time and also fills completely before the next layer starts to nucleate. There is a direct, linear relation between layer coverage and interlayer transport rate (Figure 6.10). The more a layer is filled, the higher the share of incoming molecules undergoing step-edge diffusion before they integrate into existing solid state crystallites. Once the layer is filled, there is an abrupt change and all incoming molecules directly nucleate in the subsequent layer. Thus, it is instructive to look at the share of interlayer transport rate vs. in-plane diffusion rate over time while the film is growing.

The fits according to the rate equation model allow one to separate in-plane diffusion and interlayer transport (Section 3.3.3) for the individual MLs as shown in Figure 6.10 for both discussed films. To simplify the comparison, in-plane diffusion and interlayer transport rates are accumulated for all layers at each point in time on the right side of Figure 6.10. Together, these two terms sum up to $\sum \frac{d}{dt}\,\theta_i = 1$, the total flux of incoming molecules. The share between total in-plane diffusion and interlayer transport for the T_{mod} film shows a strongly pronounced saw tooth pattern in the second to fourth monolayer in the temperature modulated case (Figure 6.10). In fact the shape is close to the one of theoretical, perfect layer-by-layer growth. Considering the intervals with $\dot{\theta}_n = \frac{d}{dt}\,\theta_i = 1$, we find that

[9] In this context, in-plane diffusion denotes the share of incoming molecules that are integrated into crystalline islands without experiencing step-edge diffusion.

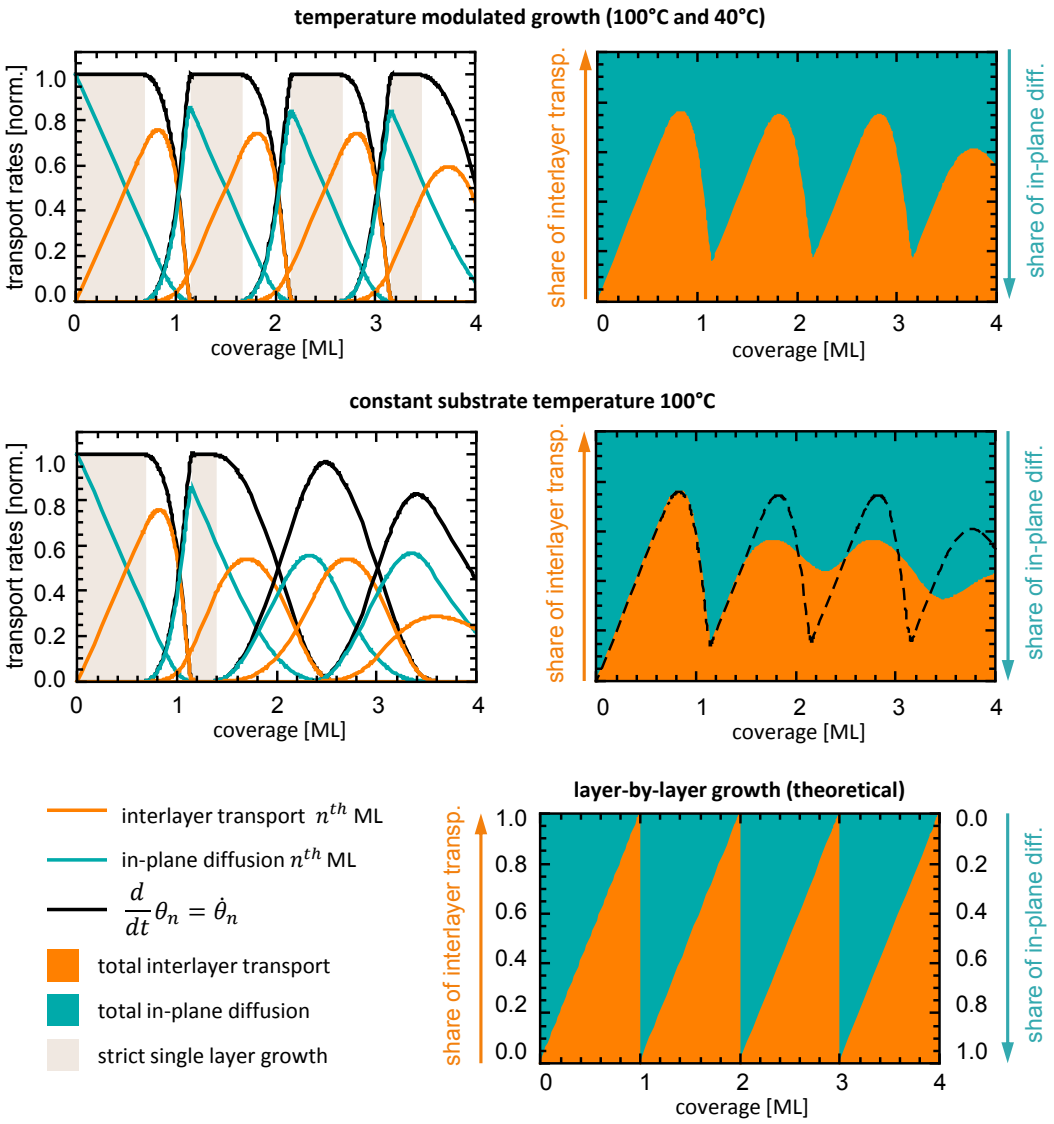

FIGURE 6.10: Left: decomposition of $\dot{\theta}_n$ into in-plane diffusion and interlayer transport. The highlighted intervals (grey) indicate strict single layer growth. Right: share of interlayer transport and in-plane diffusion during thin film growth. The incoming flux $\sum \dot{\theta}_i$ is normalised, thus, 1 corresponds to the full deposition rate of incoming molecules. There is a linearly increasing share of interlayer transport with increasing monolayer coverage for perfect layer-by-layer growth (bottom). The experimental findings suggest a less pronounced layer-by-layer growth for the film grown at const. 100 °C compared to the T_{mod} film (boundary line from the T_{mod} growth run is shown as dashed line in const. 100 °C for comparison).

Integrated interlayer transport [ML]

monolayer	T_{mod}	100 °C	difference
1. ML	0.44	0.44	
2. ML	0.40	0.32	17%
3. ML	0.40	0.35	12%
4. ML	0.34	0.27	18%

TABLE 6.3.: Integrated interlayer transport as visualized in Figure 6.11. We find approximately 15% difference in the contribution of interlayer transport for the two films.

there is a phase of single-layer growth induced by the temperature modulations in each monolayer while the layer-by-layer growth already breaks down in the second monolayer in the conventionally grown film. Even when leaving strict layer-by-layer growth behind and allowing two monolayers to grow simultaneously there has to be at least a short period of $\dot{\theta}_n = 1$, indicating that no more than two layers are growing at the same time and one of these layers closes completely, before a third one starts to fill. Thus, in the conventionally grown film there are even more than two layers growing simultaneously.

In order to quantify the enhancement of interlayer transport through the temperature modulated scheme compared to conventional thin film growth at constant substrate temperature, the integrated interlayer transport is an useful figure of merit. To account for the above discussed crucial temporal shape of the share of interlayer transport to the contribution of thin film growth, only the integrated interlayer transport before the nucleation of the subsequent monolayer is considered. Following the line of argument in the first paragraph of this chapter, we assume the moment where the nucleation in the next layer sets in to be the same point in time, where coalescence also sets in (θ_{coal}).[27] The onset of coalescence can be extracted from the temporal evolution of the island density based on GISAXS measurements (see Figure 6.11).
The resulting integrated interlayer transport for each monolayer is visualised in Figure 6.11 and summarised in Table 6.3. We find a relative increase of interlayer transport by about 15 % through the thermal cycle 100 $°C$ - 40 $°C$.

Demonstrating the applicability of synchronised thermal cycles on PTCDI-C_8 growth directly raises the question how other molecular systems react to temperature oscillations during the growth process. Preliminary results on Diindenoperylene (DIP, Appendix A.5) indicate that the influence of temperature variations during growth is much less pronounced than in PTCDI-C_8, which suggests an impact of non-kinetic processes in the case of DIP, such as thickness-dependent crystal structure re-organisation, affecting the thin film morphology. Similar to the presented findings regarding PTCDI-C_8, we find a substantial surface smoothening during thin film growth through temperature oscillations for para-sexiphenyl (6p, Appendix A.4). Thus, we conclude that it is worth to apply this new growth scheme to different molecules in order to develop a better understanding of the dominating mechanisms in organic thin film growth.

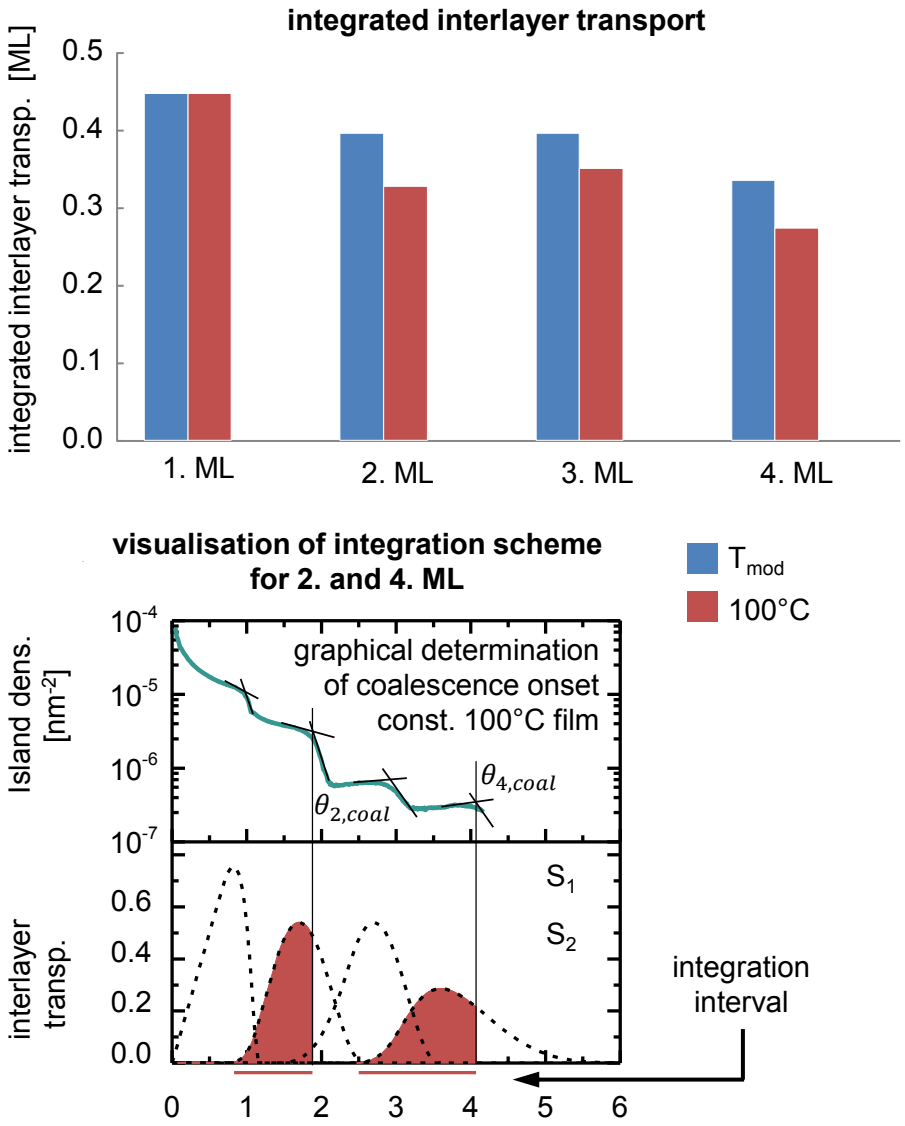

FIGURE 6.11: Top: interlayer transport contributing to layer growth as integral over interlayer transport rate. Bottom: The upper integration boundary is based on the onset of coalescences in the island density evolutions. For clarity, integration intervals are only visualised for 2nd and 4th ML.

6.5. Conclusions

We demonstrated that rapid thermal cycles triggered by anti-Bragg oscillations support the formation of smooth surfaces and layer-by-layer growth of the organic semiconductor PTCDI-C_8. Dynamic temperature modulations lead to an increase of $\approx 10\%$ in the individual monolayer coverages before nucleation in the subsequent layer sets in. With this study we show that the *concept of two mobilities* is not limited to homo-epitaxial, inorganic systems, but also works in hetero-epitaxial organic thin film growth.

From an applied sciences point of view, these film are of interest for optical applications as there is less scattering and smooth films are less dimmish. In the here pursued study the temperature swing was limited by the Peltier element of the sample holder. The ability to cool down the sample even further during the nucleation phase potentially increases the impact of the temperature modulation on the the interlayer transport beyond the observed 15%. Similar to the here employed temperature modulations, oscillations in deposition rates may be used to further increase the island density during growth recognising Equation 6.1 which gives rise to follow up experiments.
Concerning the electrical transport properties of films grown in the newly developed scheme, there are still additional experiments needed. Fully filled layers are of course beneficial for lateral transport but come on the cost of an increased number of grain boundaries induced by the higher island density. With respect to fundamental growth theory, we anticipate that applying temperature modulations during growth to further molecular species helps to understand the influence of kinetics and energetics on the growth process in a bigger picture, e.g., through possibilities to identify the Ehrlich Schwoebel barrier as attempted in Appendix B.

Overall, we consider the presented method to be a powerful tool to control island densities and thereby the surface roughness of organic thin films. Whereas high island densities and high molecular diffusivity are mutually exclusive in conventional thin film growth, our method allows combining both.

7

Thermally Driven Smoothening of Molecular Thin Films

While in the previous chapters we focus on controlling the thin film growth process *in-situ*, a different approach to control surface morphologies in organic thin films is described in the following chapter. Here we focus on molecular diffusion processes activated by thermal treatment of organic thin films after growth and at ambient conditions. Post-growth annealing as such is no new approach to influence the morphology of organic thin films but in the particular material system studied here we find a rarely observed smoothening of the thin film structure at elevated temperatures. As in the previous chapters, we focus on the role of diffusion and interlayer transport in the smoothening process. The findings presented in this chapter were published in reference [188]. In part the text and figures are reprinted with permission of the publisher AIP Publishing to reuse the article 164707 (2015) in the Journal of Chemical Physics 143.[1]

7.1. Motivation

Thermal annealing is an important process to improve structural and functional properties of molecular thin films. The increased temperature during the annealing process often helps to heal crystal defects and to increase crystallite sizes.[189] However, the structural definition at interfaces and surfaces may also decrease due to molecular diffusion, dewetting and roughening.[49,190] Organic molecular beam deposition (OMBD) in particular often leads to kinetically limited, non-equilibrium structures and postgrowth annealing

[1] A detailed listing of the contributions of all individual co-authors can be found on page 162.

and therefore can significantly influence morphology and crystal structure.[97] Here we study in detail the annealing of alkane thin films using real-time techniques. Alkane molecules with their simple, rod like molecular shape are a model system for more complex chain-like organic molecules,[191–193] and are also important building blocks, e.g., as side chains of polymers, and can dominate their crystallisation behaviour.[194,195]

Beyond its importance as generic model system for fundamental molecular processes, TTC in particular is also of technological importance in organic electronics as an encapsulation material for transistors and biosensors in an aqueous environment[196,197], where the active layer is completely wetted by TTC and therefore fully encapsulated.

In a different application, TTC has been incorporated in field-effect transistors as a smooth gate dielectric on top of a silicon gate.[31,32,198] In such devices a TTC layer beneath the active molecular layer is used to passivate traps at the substrate oxide surface and further leads to improved growth and larger grain sizes of the on-top deposited semiconducting film. In this application it has been found that the performance of ambipolar field-effect transistors can be improved by using smoothed TTC layers.[199–201] The grain size of the on-top deposited semiconducting film depends on the grain size of the underlying TTC layer. Therefore, in addition to the goal of achieving a fundamental understanding of organic thin film annealing, there is also a technological demand to maximise of the TTC grain size.

TTC films[88] and single crystals[202–205] prepared from melts have been analysed before and several crystal structures have been reported in the literature. X-ray studies on $C_{44}H_{90}$ and structural changes of alkanes near their melting point range back as far as 1930 by A. Müller and are still subject of recent studies.[88,205] Single crystals grown from solution show a monoclinic crystal structure with a d-spacing of roughly 52 Å.[203,206–208] When exposed to temperatures near the alkane melting temperature, a transformation into an orthorhombic structure[88,191,206–210] with an increased d-spacing of roughly 58 Åcan be achieved. In addition, a triclinic phase[203] and also a rotator phase[202] has been reported. Unlike most materials, alkanes feature a surface freezing behaviour resulting in a higher temperature of the ordering transition in two-dimensional than in three dimensional systems.[34,211] Due to the surface freezing effect, the melting point of the surface layer of an alkane melt is increased compared to the bulk material.[33] This behaviour has been studied in detail by Ocko *et al.* who also found a remarkably wide range lateral crystalline order of 1 μm in surface-frozen alkane monolayers.[35,212]

In this paper we show that through annealing we can achieve molecular thin films that have both larger crystalline domains, and, importantly, also feature a smoother surface morphology at the same time. However, heating beyond a phase transition reduces the crystallinity again, so that a trade-off between crystallinity and molecularly flat island size has to be found. We relate the strongly anisotropic attachment energies of TTC to its annealing behaviour and show that they can be used for interface engineering with optimisation of both morphology and crystallinity within the correct temperature range.

7.2. Experimental Details

TTC (purity > 99 %) was purchased from Sigma -Aldrich and used without further purification. TTC molecules have been evaporated and deposited in an organic molecular vapour deposition setup with a base pressure of $1.7 \cdot 10^{-7}$ *mbar* onto silicon wafers with either a native oxide or a 300 *nm* thermal oxide layer. After deposition, the TTC coated wafers were transported to a glove-box via a transfer system and stored under nitrogen atmosphere. In order to improve the contrast in reflection optical microscopy, Si wafers with dry, thermally grown 300 *nm* SiO_x layer (Siegert) were used for additional samples.

For time-resolved annealing studies we applied reflection optical microscopy to the TTC thin films and achieved contrast between molecular monolayers (ML) with heights below 1 nm. In the setup an Olympus AX70 microscope with 100x magnification illuminates the sample with coherent monochromatic laser light and a phase image is recorded by a CCD camera. Further details on the setup can be found in ref.[123]. As the sample holder in the microscope setup, a heating stage was used, which opens the possibility to monitor molecular annealing-kinetics in real space. For comparison atomic force microscopy (AFM) images with calibrated height resolution were recorded with an *Autoprobe CP* from *Park Scientific Instruments.*[213] While AFM offers superior resolution, our reflection optical microscope has higher temporal resolution, greater thermal stability and can also collect morphological information of very soft or even molten molecular films.

The grown and annealed films were subsequently analysed in different x-ray geometries. Grazing incidence wide angle x-ray scattering patterns have been recorded at the P03 beamline PETRA III at DESY, Hamburg at a wavelength of 0.957 Å and at the ESRF ID03 beamline with 1.31 Å wavelength together with $\theta - 2\theta$ scans of previously annealed samples.[81,214] All x-ray measurements have been performed at room temperature under nitrogen atmosphere. The temperature measurements of the *in situ* x-ray and the microscopy setup differed by about $2\,K$ and we estimate the overall error in the temperature measurements to be $\pm 5\,K$.

7.3. Results and Discussion

Evaporated TTC thin films undergo significant morphological and structural changes during thermal annealing. In freshly grown films, TTC molecules arrange in two distinct morphologies: flat, crystalline islands with monomolecular step-edges and crystalline mounds of more than 100 *nm* in height (see AFM insets in Figure 7.1). These two morphologies have also been found by Kraus et al.[200] Figure 7.1a shows the GIXD pattern of the TTC film as deposited. At $q_{||}$=1.50 Å^{-1} and $q_{||}$=1.66 Å^{-1}, the (110) and (020) in-plane reflections are visible. This can be assigned to textured, upright standing molecules with respect to the substrate. Further, a ring-shaped diffraction pattern above the (110) reflection is visible. This powder diffraction ring at |q| = (1.5±0.1) Å^{-1} is due to randomly oriented TTC crystallites. The ring-shaped diffraction pattern disappears when rising the film's

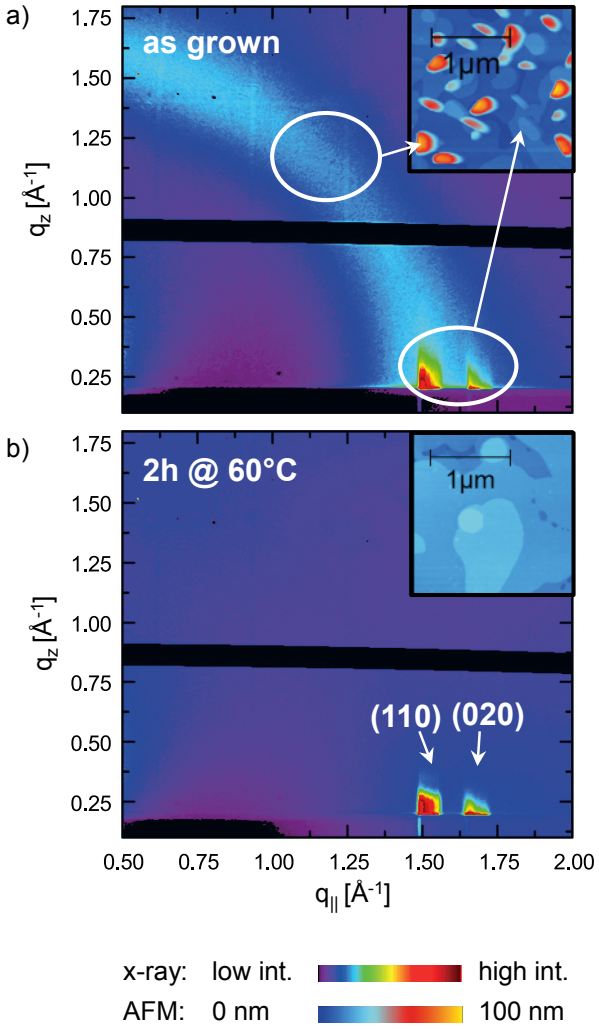

FIGURE 7.1: a) GIXD pattern of TTC grown at RT shows intense Bragg (110) and (020) Bragg reflections of textured, crystalline islands and a powder diffraction ring originating from randomly oriented crystalline mounds (inset: AFM image showing an area where both crystalline species appear). b) GIXD and AFM of the annealed sample that has been kept at 60 °C for two hours. The mound shaped crystallites as well as the diffraction ring disappear during annealing and the lateral island size increases.

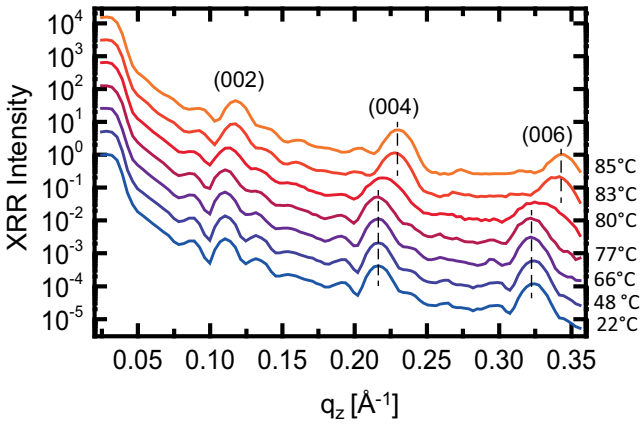

FIGURE 7.2: In-situ x-ray reflectivity at different substrate temperatures. A phase transition occurs between 77 °*C* and 83 °*C*, with phase coexistence at 80 °*C* as suggested by the increased width of the (004) and (006) Bragg reflections

temperature to 60 °*C* (Figure 7.1b). As visible from the AFM image (Figure 7.1b, inset), the mound shaped crystallites are also missing after this process. Hence, through annealing of the film the randomly oriented crystallites disappear. This leads to the conclusion that untextured molecular crystallites are located in the mound shaped structures and that they are in a thermodynamically less favourable confirmation than the underlying textured molecular film.

To study the out-of-plane structure of the textured molecular islands during the annealing process in N_2 atmosphere, we make use of *in-situ* x-ray reflectivity (XRR).[71] As shown in Figure 7.2, in the temperature range between 20 °*C* and 60 °*C* we cannot find any significant changes in the reflectivity signal. Annealing in this temperature range also increases the crystallinity of the sample (Figure 7.3). Both the films grown at room temperature as well as films heated to up to 77 °*C* show an out-of-plane lattice spacing of (58.8 ± 0.3) Å. Together with the position of the in-plane diffraction peaks (Figure 7.4) this is in agreement with the commonly known orthorhombic crystal structure (a=4.98 Å, b= 7.44 Å, c=115.2 Å).[88,191,206–210]

Further elevation of the substrate temperature from 77 °*C* to 83 °*C* induces a phase transition to a high temperature (HT) structure that is characterised by a significant decrease of the out-of-plane lattice spacing. At about 80 °*C* both crystal polymorphs coexist, as can be seen from the increased width of the Bragg reflections in Figure 7.2. The new phase persists even after cooling down the sample to room temperature (measurements presented in Figure 7.4), *i.e.* the phase transition is irreversible. For this emerging phase we find a reduced out-of-plane lattice constant of (53.4 ± 0.3) Å similar to the lattice parameter reported by Gorce *et al.*[203] and Sullivan *et al.*[208] in single crystals. Through the reduction of the out-of-plane lattice spacing from 58.8 Å to 53.4 Å, we estimate the molecular tilt angle with respect to the surface normal to be $\varphi = 90° - \left(\frac{53.4°}{58.8°}\right) \approx 24°$.

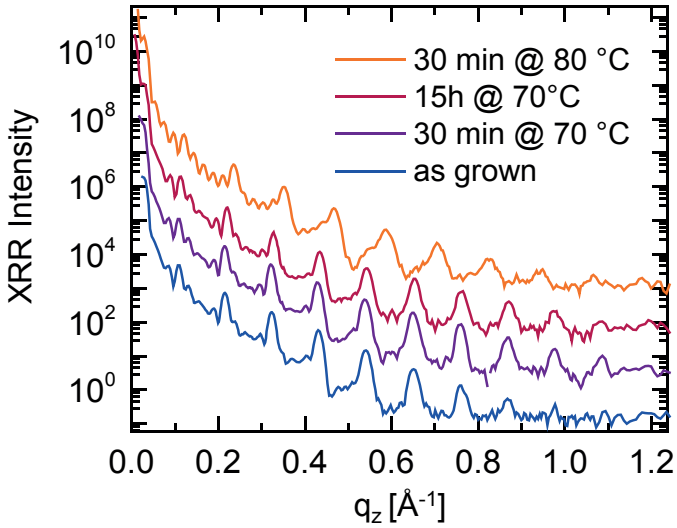

FIGURE 7.3: The intensity of higher order Bragg reflections increases significantly when elevating T_{sub} temporally to temperatures between 60 °C and 70 °C. The new crystal phase emerges at about 80 °C. Here the intensity of higher order Bragg reflections reduces again.

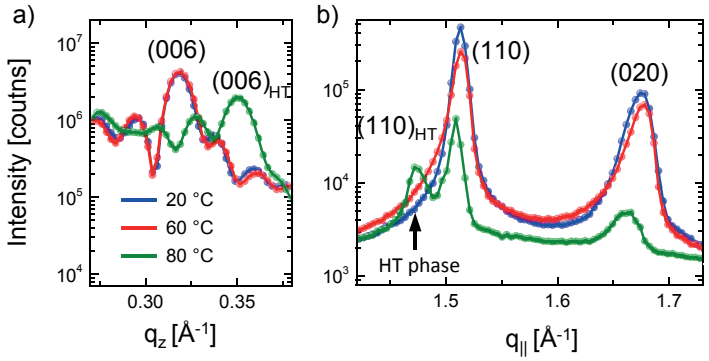

FIGURE 7.4: The new phase persists even after cooling the sample back to room temperature as evidenced by the irreversible new reflections in a) XRR and b) GIXD

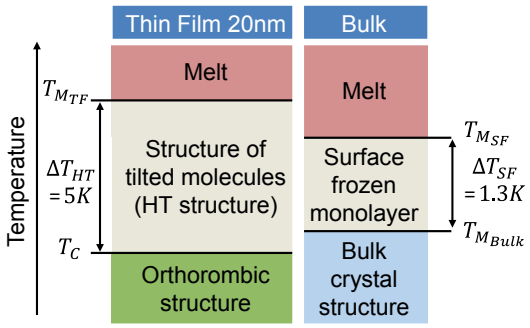

FIGURE 7.5: Comparison between temperature dependent structures in thin films and bulk crystals, that highlights the similarities between the HT structure in thin films and surface frozen monolayers. An offset in the absolute temperature values can be attributed to differing setups for thin film and bulk crystal experiments.

An additional in-plane diffraction peak at $q_{\parallel} = 1.47\,\text{Å}^{-1}$ corresponds to this HT phase (Figure 7.4). Bai *et al.* find a similar in-plane diffraction pattern for a sub-monolayer of $C_{32}H_{66}$ on Si which also emerges with increasing temperature and correlate it with surface frozen structures.[215] The new lattice spacing as well as the molecular tilt angle and the increased in-plane lattice spacing of 4.26 Å are consistent with the values found by Ocko *et al.* for the surface frozen monolayers of $C_{44}H_{90}$.[35] Therefore, we conclude that the HT structure, which emerges at a critical temperature T_C, about $\Delta T_{HT} = 5\,K$ below the thin film melting point, shows apparent similarities to surface frozen monolayers existing in a temperature range $\Delta T_{SF} = 1.3\,K$[35] between bulk and melting temperature of the surface frozen layer (see Figure 7.5). A comparable behaviour can be found for $C_{30}H_{62}$ and has been correlated to its rotator phase.[216] The general similarity of molecular thin films and surface frozen monolayers found on alkane melts close to their melting temperature due to their similar dimensionality has been previously highlighted by Witte and Wöll.[55]

We performed heating cycles on TTC thin films grown at room temperature on substrates with a 300 *nm* SiO_x layer with the aim to characterise the molecular island size evolution, which is relevant for technological use of TTC, but also serves as a model for annealing of other rod-like molecules. To gain real-time insights, the sample is monitored by reflection optical microscopy while increasing the substrate temperature (Figure 7.6 a to d). For reference, additional samples have been heated to 60 °*C* and 82 °*C* resp. and cooled down again to be analysed by AFM (insets in Figure 7.6 have the same scale with respect to optical microscopy images). The AFM image of the as-grown sample (inset of Figure 7.6a) reveals mound shaped structures on top of the film with a smaller lateral dimension (below 300 *nm*) compared to the underlying molecular terraces, but with heights of 100 *nm* and more. These mounds are too small to be resolved in the optical microscope with a lateral resolution of 500 *nm* and are only visible in AFM. Heating the TTC film to 60 °*C* (Figure 7.6b) leads to an increased lateral grain size from about 1 μm to 5 μm and to a disappearance of the mound shaped crystallites as mentioned above. Starting at temperatures above 60 °*C* the molecular islands grow significantly and reach diameters of

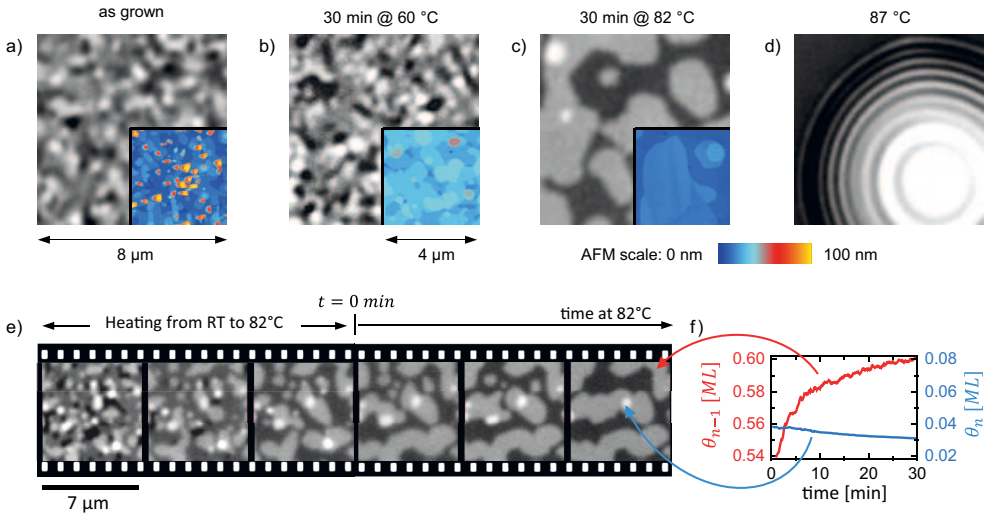

FIGURE 7.6: Top: Reflection optical microscopy images at different temperatures and corresponding AFM images (insets) for samples that have been heated to the same temperatures and cooled down to room temperature again. Contrast from step edges of single molecular height is visible in optical microscopy. This enables a real-time observation of annealing at different temperatures, starting with coexistence of islands and mounds on top in a), the disappearance of mounds and an increase of island size at 60 $°C$ in b) and a significant increase of island size at 82 $°C$ in c). At 87 $°C$ the TTC dewets into molten droplets d). Bottom: e) Time series of optical microscopy images highlighting the smoothing of the film. Downhill transport of molecules in layer n (monolayer (ML) coverage (θ_n) fills holes in layer n-2 and increases layer coverage (θ_{n-1}) in layer n-1 (see graph of layer coverages f). Ostwald ripening leads to significantly increased island sizes in the partially filled layer n-1.

up to 10 μm (average grain area in the order of 2.5 μm^2) at 82 $°C$ (Figure 7.6c), which can be fully resolved with an optical microscope. In this temperature range the phase transition to HT phase has already begun and there is phase coexistence in the film (Figure 7.2). Further heating of the sample leads to the formation of liquid TTC droplets that result in Newton-rings in the microscope (Figure 7.6d) at 87 $°C$.

Since the optical microscopy allows us to record real time data (Figure 7.6e), the individual layer coverage has been extracted [217] from an approximately 5000 m^2 sized area in Figure 7.6f. While the topmost layer n and higher structures depopulate over time at a rate of $-5 \cdot 10^{-4}$ ML/min at 82 $°C$, the underlying layer $n-1$ is filled at a rate of up to 10^{-3} ML/min. Simultaneously the number of islands and the corresponding boundary length of both layers decreases, which indicates an Ostwald ripening process. The video footage of this process clearly indicates that smaller islands coalesce with larger ones and that molecules from the topmost layer are adsorbed in underlying layers (downhill transport) resulting in a significant smoothing of the film surface. Within a few minutes at temperatures of 5 K below the melting temperature the lateral dimension of ML height islands increases drastically up to 10 μm in diameter. Bai *et al.* have observed a similar behaviour in the case of $C_{30}H_{62}$ close to its melting point. [215] Focusing on the lateral structure the model

of 2D-Ostwald ripening explains the observed behaviour in terms of the Gibbs-Thomson effect: smaller crystalline structures have a reduced melting temperature compared to larger ones due to their higher fraction of surface atoms.[28] According to this theory, a molecular island suddenly dissolves completely once its size falls below a certain limit[218] - a behaviour clearly observable in our real-time microscopy data.

Compared with other molecules such as pentacene (PEN),[219,220] PTCDA[221] or oligothiophenes[190], which tend to roughen when heated to elevated temperatures, the 2D-ripening and smoothing of a crystalline n-alkane thin film during annealing is unexpected. In what follows we contrast the molecular kinetics and energetics of TTC with PEN, as a prototypical molecule in organic thin film growth[222] that does not show thermal smoothing but surface roughening.

During the annealing process the kinetics play an important role. Therefore it is instructive to compare growth speeds in different crystallographic directions because fast lateral and slow vertical growth favours 2d ripening. Already the equilibrium crystal shape points to the fact that TTC grows more in 2d fashion as its equilibrium shape is plate-like[223,224] in contrast to the more 3d equilibrium crystal shape of PEN.[225] Further, during the annealing process the growth speeds are governed by the attachment energies and intermolecular forces of molecules to different crystal facets, which we calculated in a simple Coulomb-London-Pauli force-field model.[226] For TTC we find the head-to-tail attachment energy to be only $2.5\,kJ/mol$ while lateral attachment is strongly favoured at $334.0\,kJ/mol$. For pentacene in its bulk structure, we calculated the respective attachment energies to be $12.9\,kJ/mol$ *vs.* $256.9\,kJ/mol$. The much stronger anisotropy in attachment energies of TTC (1:140) in contrast to PEN (1:20) contributes to the observed smoothing of TTC films.

Beyond kinetics, the energetics of TTC and PEN as well as the substrate surface have to be considered, since a lowering of the surface and interface energies are major contributions to the minimisation of the Gibbs free energy during annealing. Under annealing conditions PEN exhibits a phase transition from an orthorhombic thin film phase (TF) towards its triclinic bulk crystal structure. This phase transition goes hand in hand with a morphological change that lowers the pentacene surface / volume ratio by forming 3d crystals instead of a continuous film. As a result the total surface energy increases whereas this loss is more than compensated by the reduction of the volume Gibbs free energy in the bulk phase.[227] The observed smoothening of the TTC film in contrast leads to the conclusion that in this case the reduction of the surface energy plays the dominating role and that the volume Gibbs free energy does not change much during the observed phase transition towards the HT phase.

Taking a closer look at the surface energies of PEN and TTC, a notable difference can be found in the absolute values of the surface energies that range between $50\,mJ/m^2$ and $150\,mJ/m^2$ depending on the crystal facet for PEN[228] and between $20\,mJ/m^2$ and $30\,mJ/m^2$ in the case of TTC.[229] This difference in the surface energies explains the distinct wetting behaviour of alkanes and aromatic molecules like PEN on silica surfaces

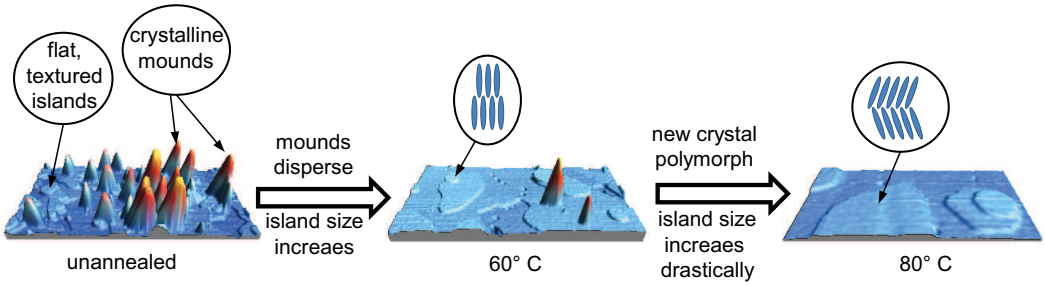

FIGURE 7.7: Sketch of the TTC surface morphology at different temperatures with indicated crystal structures.

that has a surface energy of (57.514) mJ/m^2.[180] With its low surface energy, TTC is driven to wet both the SiO_2 substrate and underlying alkane layers, as demonstrated by Lazar *et al.* for $C_{30}H_{60}$ und $C_{36}H_{74}$.[33] In this study also the coexistence of a crystalline alkane phase and a liquid phase has been observed, in contrast to PEN where only solid phases have been found for the given annealing conditions.[230] This qualitative difference is important in the context of ripening and surface smoothing as the liquid phase allows for significant mass transport across several μm.

7.4. Conclusion

Our results quantify the variety of technologically relevant morphological and structural changes that TTC thin films undergo during annealing. As illustrated in Figure 8.4, we identify two stages in the annealing process of TTC films grown at 20 $°C$ that consist of both flat 2D islands and 3D mounds. First, the crystalline mounds disappear at around 60 $°C$ and, secondly, above 80 $°C$ the lateral dimension of the TTC islands increases significantly and an irreversible phase transition occurs. We find a remarkable smoothing and strong lateral growth of flat islands which results from annealing TTC thin films at temperatures close to the melting point. The use of a phase contrast optical microscope enables us for the first time to follow the annealing and downward flux across step edges of alkane molecules in evaporated multilayer films and demonstrates the promise of this technique for real time growth studies. The flat molecular structures on large lateral scales are particularly promising for the technological use of TTC as a planar insulating layer and a template for pseudoepitaxial growth of other organic semiconductors on top. We identify the anisotropic binding energies and low surface energies as key parameters for the favourable annealing properties. This improves the understanding of organic thin film growth and might help to tailor molecules with desired wetting properties.

III

Summary & Conclusions

8

Summary

This chapter gives a summary of the presented experiments as well as their main results. Within this thesis we have used scattering, imaging, and spectroscopic methods to analyse and understand the influence of external stimuli on the growth of organic thin films. With the aim to find new degrees of freedom for tailoring growth of organic thin films, we have explored *in situ* illumination, dynamic temperature modulations and thermal annealing. We have especially focused on growth control through the presence of optical fields since light is predestined as a control parameter to shape organic thin films during growth.

Controlling Polymorphism and Phase Purity in Organic Thin Films by Light

Phase purification through growth under illumination

In Chapter 4 we presented a study of the influence of light on the crystallisation of α-sexithiophene (6T) thin films. Using laser illumination during growth, we have found a beneficial influence of light on the phase purity of 6T thin films grown on KCl. Conventionally grown 6T thin films exhibit a bimodal growth behaviour with coexistence of two crystal phases that grow simultaneously (the low temperature (LT) and high temperature (HT) polymorphs).

In synchrotron based real time x-ray reflectivity experiments we monitored the intensity of Bragg reflections corresponding to the two phases and thereby identified the phase-content of low and high temperature phase in the sample. We have found a suppression of the HT phase content by 75% in regions grown under 532 nm illumination at 1 W/cm^2. Thus, the phase purity in 6T films grown illumination was increased by a factor 4 in favour of the LT phase. This finding is independent of the substrate temperature between 0°C

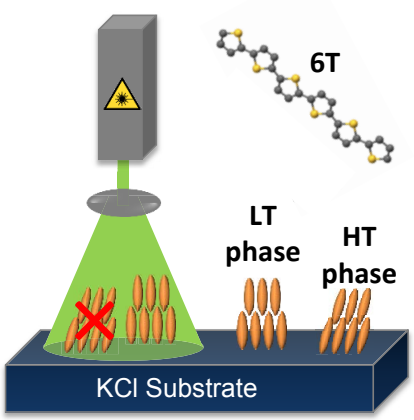

FIGURE 8.1: Phase purification in sexithiophene thin films through illumination during growth

to 60°C. Therefore, we can exclude simple opto-thermal substrate heating as mechanism behind the observed phase purification.

Origin of phase purification: increased optical absorption and lower thermal stability of the HT phase

We have identified the HT phase to be less stable and to absorb 532 *nm* light 20% stronger. The increased absorbance of this phase is explained by the 10° larger tilt angle of the long molecular axis, which is aligned parallel to the relevant transition dipole moment with respect to the surface normal of the sample. In desorption experiments we have been able to measure the reduced relative phase stability of the HT phase as predicted by *ab initio* calculations. Therefore, the combination of increased optical heating and lower thermal stability leads to the observed phase purification.

Controlling Azimuthal Molecular Alignment through Optical Fields

Polarised illumination aligns molecular crystallites in polycrystalline organic thin films on amorphous substrates

We have explored possibilities to control the molecular alignment in thin film growth through resonant illumination. Using amorphous substrates (silica and glass), we examined the potential to use the anisotropy carried by light through its polarisation (here linearly polarised light) to grow anisotropic thin films.

We demonstrated *light induced self-assembly* (LDSA) for Tetracene which has an optical transition (lower Davydoy component, $\mathbf{D}_+$) matching the $532\,nm$ laser light used for illumination during growth. The transition dipole moment $\mathbf{D}_+$ in this crystal is aligned almost parallel with the unit cell axes a of the the molecular crystal ($\sphericalangle\,[\mathbf{D}_+, a] = 4.3°$). Thus, the absorption of a Tetracene crystal at $532\,nm$ ($2.32\,eV$) is azimuthally highly anisotropic. We could show that under linearly polarised illumination with $5\,W/cm^2$ the normally observed isotropic, uniform distribution of azimuthal crystallite orientations gives way to an aligned crystal structure. In this structure a common optical axis, which we labelled as *optical twin axis*, defines the orientation the $\mathbf{D}_+$ transitions of the crystal grains in the film. Due to the triclinic nature of the tetracene unit cell there are four distinct in-plane orientations of crystal grains found in LDSA grown films which we refer to as *optically twinned crystals*.

Photoalignment due to azimuthal opto-thermal re-organisation during growth

We have considered two distinct alignment mechanisms. One based on the *optical Fréedericksz effect* which we found not to be able to explain the alignment of the fast optical axis parallel to the external optical field. The second model is based on opto-thermal heating of crystallites that are illuminated in resonance with the external laser field ($\mathbf{D}_+$ parallel to laser polarisation $\mathbf{E}_L$ during growth). Therefore, the crystallites selectively addressed by the laser are more mobile and more likely to dissolve than those that are oriented such that their $\mathbf{D}_+$ are perpendicular to $\mathbf{E}_L$. We have visualised this re-organisation mechanism in form of *pseudo-potential* with minima for azimuthal crystal orientations with $\mathbf{D}_+ \perp \mathbf{E}_L$,

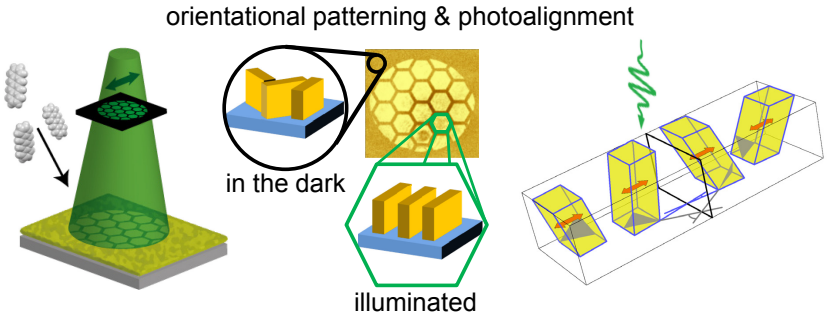

FIGURE 8.2: Inducing azimuthal alignment and patterning in tetracene thin films through polarised illumination during growth.

so that crystallites in these orientations preferentially grow under LDSA.

Photo-lithographic azimuthal top down patterning in organic thin films
In addition to the azimuthal alignment, we have patterned the optical properties of tetracene thin films using a shadow mask during illumination and growth. Illuminated regions during growth exhibit anisotropic optical luminescence properties emitting linearly polarised light while unpolarised luminescence is found in regions that were dark during growth. We anticipate this method to enable the fabrication of molecular thin films with locally controlled, anisotropic optical constants.

Controlling Thin Film Growth through Rapid Thermal Cycles

The concept of two mobilities transferred to organic thin film growth
In Chapter 6 we have made use of the concept of two mobilities to tailor organic thin film growth. While the island density is defined in the initial nucleation phase of monolayer growth, the step-edge barrier E_{ES} hinders molecular diffusion in later stages of monolayer growth. Employing a dynamic temperature modulation scheme during individual monolayer growth allowed us to grow films combining both high island densities and high molecular diffusivity. In a theoretical case study using phase-field simulations we showed that the surface smoothness of molecular thin films can be significantly increased through temperature modulations during growth.

Dynamic temperature control during monolayer growth smoothens PTCDI-C_8 films
Using *in-situ* x-ray growth oscillations, we have measured individual monolayer coverages in real-time and synchronised rapid thermal cycles to the nucleation phase during the growth of each monolayer. Cooling the underlying substrate during the nucleation phase resulted in an increase of the nucleation density by more than one order of magnitude. Elevated surface temperatures on the other hand improved diffusion. Employing a $100\,^{\circ}C$ / $40\,^{\circ}C$ temperature scheme, we were are able to grow PTCDI-C_8 films with 40% reduced surface roughness.

Enhancement of interlayer transport
We have identified both the amount of interlayer transport and its correct timing to be substantial for the growth of smooth PTCDI-C_8 films. We found an increase of 15 % in the interlayer transport through $100\,^{\circ}C$ / $40\,^{\circ}C$ cycles. This observation is based on a rate equation growth model that has been fitted to the measured anti-Bragg intensity oscillations during thin film growth. Further optimisation of the thermal cycle (e.g. steeper gradients and increased deviation) shows the potential to lead to even smoother thin films.

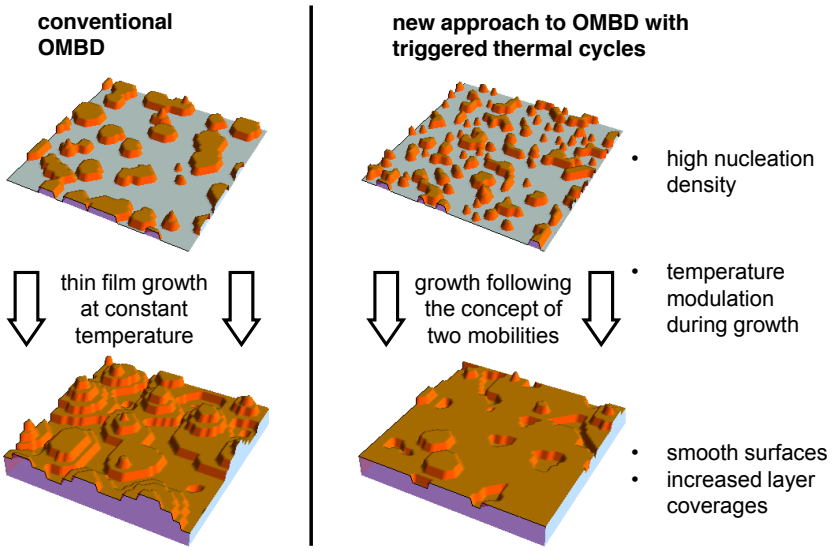

FIGURE 8.3: Enhancing thin film growth through cooling cycles to increase the island density in the film while conserving high molecular diffusivities. The illustration is based on results from phase field simulations.

Thermally Driven Smoothening of Molecular Thin Films

In Chapter 7 we studied the morphology evolution of n-alkane ($C_{44}H_{90}$, TTC) thin films under annealing conditions. Thermal treatment of organic thin films is a widely used method to alter structure and morphology after deposition. While thin film growth processes often proceed far from equilibrium, thermal annealing on the contrary can be employed to subsequently modify the structure and morphology in thin films to approach the equilibrium structure of the film. For many molecular materials this process includes dewetting and the formation of pronounced 3d crystallites.

Thermal smoothening & lateral island growth through material transport in underlying layers in n-alkane thin films

For TTC we have found a strong increase in the lateral island size through annealing and reached island diameters of up to 10 μm. From an applied physics perspective, these large, single-crystalline domains show beneficial properties for the us as, e.g., gate dielectric for organic field-effect transistors.

Together with the strong increase in the lateral domain size, we have found a smoothening process based on interlayer transport from topmost layers into underlying ones. We have studied the smoothening process via real-time *in situ* optical microscopy resolving individual molecular monolayers. From these results we conclude that Ostwald ripening dominates the morphological changes in TTC thin films during annealing. Firstly, small molecular clusters and islands exhibit a reduced melting temperature compared to larger ones. Thus, they dissolve and give rise to highly mobile molecules on the surface. Secondly, larger islands grow continuously and straighten their grain boundaries by integrating

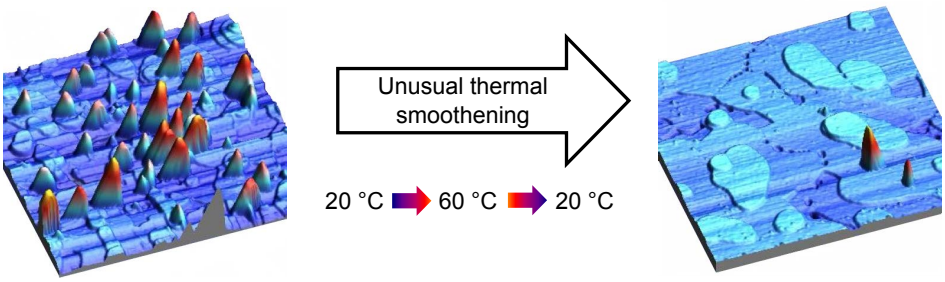

FIGURE 8.4: Thermal smoothening through annealing in n-alkane ($C_{44}H_{90}$) thin films strictly opposes roughening induced by annealing as observed for most other crystalline organic thin films.

the molecules that are available through interlayer transport. Thus, underlying layers fill up while upper ones tend to empty during the annealing process. The here presented observations potentially extend the application field of n-alkane encapsulation layers towards thermally activated, self-healing surfaces coatings.

Low surface energies together with strongly anisotropic equilibrium shape result in smooth films under annealing conditions
Structure calculations reveal plate-like equilibrium shapes for n-alkanes with chain lengths comparable to $C_{44}H_{90}$. Furthermore, we found strongly anisotropic cohesive energies due to the pronounced anisotropy in the shape of the molecule and low surface energies for the (001) surface so that complete wetting of the underlying silicon wafer is ensured. In multilayer samples the plate-like equilibrium of individual crystallites leads to formation of large, flat terraces through diffusive processes and Ostwald ripening.

Persistent crystal structure transition close to the melting point
When heating a TTC film close to its melting temperature, we found, additionally to the above described structural coarsening, intrinsic changes in the crystal structure. We documented the emergence of an additional high temperature crystal phase that shows great structural similarity with surface frozen n-alkane monolayers. Once it is formed at elevated temperature, this structure persists at room temperature after cooling down the sample again.

9

Conclusions

With this thesis we aimed to address the current challenges in the field of organic thin film growth. We implemented novel strategies to enhance control of morphology during thin film growth. Additionally we made use of the of unique photo-physical phenomena of molecular materials to produce anisotropic thin film structures. In this context we have targeted to establish design rules and recipes for the creation of functional thin films.

While significant progress has been made in the synthesis and availability of new upcoming high-performance molecular materials, there are still fundamental hurdles that hinder the way towards high-performance thin film devices. Here we focused on exploiting simple interactions between individual molecules to tailor thin film micro-structure. We have explored effective ways to force well-studied organic semiconducting materials to adopt specific intermolecular motifs in a certain crystal phase. Thus, it is possible to tune functional properties by processing modification through external stimuli in organic molecular beam deposition.

With light as a control parameter, we brought local structural control to organic thin film growth. Thereby, we established a technique bridging the gap between molecular self-assembly on the nano scale and photo-lithography on the meso & macro sale. This approach facilitates the fabrication of organic devices, such as transistors with improved charge carrier mobility, vortex retarders, active photonic meta-surfaces or polarised light emitting diodes.
In this thesis, additional emphasis has been laid on strategies to enhance thin film morphology and to produce molecular thin films with low surface roughness. Depending on material and processing conditions, thermodynamic as well as non-equilibrium processes have the potential to contribute to smoother thin film growth. We anticipate that the presented strategies will advance the morphology-by-design approach in organic thin film growth.

Acknowledgements

I would like to express my gratitude to everyone who supported me in the course of this thesis. First and foremost I want to thank Prof. Stefan Kowarik for offering me the opportunity to conduct the presented scientific research, his motivating mentorship and also the friendly and personal atmosphere in the group. Further, I want to acknowledge the guidance through Dr. Peter Schäfer concerning the details of crystallography and PD Dr. Andreas Opitz for his support realising the n-alkane and LDSA project.

Further, I would like to thank my colleagues Anton Zykov, Christopher Weber, Giuliano Duva, Sebastian Bommel and Paul Beyer for their help during numerous synchrotron beam times and their support throughout the years. Special thanks also go to Laura Bogula who I worked with on the rapid thermal cycle project. I have greatly benefited from the atomic force microscopy lab of Jürgen P. Rabe and the advice of Manuel Gensler.

I would like to express my gratitude to Prof. Claudia Draxl, Dr. Caterina Cocchi and Bernhard Klett for the fruitful collaboration on joint experimental and theoretical studies on α-sexithiophene. Additionally, I want to thank Dr. Hans Riegler, Chenyu Jin and Eduard Meister for their helping hand on the n-alkane project as well as Prof. Frank Schreiber and Dr. Alexander Gerlach for stimulating discussions.

Without the ongoing encouragement from family and friends, this thesis would not have materialised. Amongst others, I want to especially thank Henrik Wilming, Thilo Krause and Lewin Stein for numerous discussions and advice on theoretical aspects of this work and numerical aspects of partial differential equations. I also want to thank Siri Rackebrandt for her support in typesetting this thesis. Further I owe my deepest gratitude to Magdalena Uber and Helmut Pithan for their continuous support.

Finally I would also like to express my gratitude to ESRF, Diamond, Desy and SLS to enable the research presented in this thesis by allocating synchrotron beam time to the respective proposals and Studienstiftung des deutschen Volkes for the financial support.

References

[1] H. T. Yi, M. M. Payne, J. E. Anthony, and V. Podzorov. Ultra-flexible solution-processed organic field-effect transistors. *Nature Communications*, 3:1259, December 2012. doi: 10.1038/ncomms2263.

[2] M. Mas-Torrent and C. Rovira. Role of molecular order and solid-state structure in organic field-effect transistors. *Chemical Reviews*, 111(8):4833–4856, August 2011. doi: 10.1021/cr100142w.

[3] M. Gruber, M. Rawolle, J. Wagner, D. Magerl, U. Hörmann, J. Perlich, S. V. Roth, A. Opitz, F. Schreiber, P. Müller-Buschbaum, and W. Brütting. Correlating structure and morphology to device performance of molecular organic donor–acceptor photovoltaic cells based on diindenoperylene (DIP) and C_{60}. *Advanced Energy Materials*, 3(8):1075–1083, 2013. doi: 10.1002/aenm.201201012.

[4] Z. Li, H. C. Wong, Z. Huang, H. Zhong, C. H. Tan, W. C. Tsoi, J. S. Kim, J. R. Durrant, and J. T. Cabral. Performance enhancement of fullerene-based solar cells by light processing. *Nature Communications*, 4:2227, July 2013. doi: 10.1038/ncomms3227.

[5] M. Auer, L. Pevzner, S. Sax, and E. J. W. List-Kratochvil. Solution processed multilayer organic light emitting diodes. In N. Koch, editor, *Supramolecular Materials for Opto-Electronics*, chapter 7, pages 226–272. The Royal Society of Chemistry, 2015. ISBN 978-1-84973-826-2. doi: 10.1039/9781782626947-00226.

[6] C. Simbrunner, G. Hernandez-Sosa, E. Baumgartner, G. Hesser, J. Roither, W. Heiss, and H. Sitter. Para-sexiphenyl-CdSe/ZnS nanocrystal hybrid light emitting diodes. *Applied Physics Letters*, 94(7):073505, 2009. doi: http://dx.doi.org/10.1063/1.3086295.

[7] C. Wang, H. Dong, W. Hu, Y. Liu, and D. Zhu. Semiconducting π-conjugated systems in field-effect transistors: A material odyssey of organic electronics. *Chemical Reviews*, 112(4):2208–2267, 2012. doi: 10.1021/cr100380z.

[8] M. and H. Wolf. *Organic Molecular Solids*. Lehrbuch Physik. Wiley-VCH, Weinheim, Germany, 2008. ISBN 9783527618668.

[9] S. Duhm, G. Heimel, I. Salzmann, H. Glowatzki, R. L. Johnson, A. Vollmer, J. P. Rabe, and N. Koch. Orientation-dependent ionization energies and interface dipoles in ordered molecular assemblies. *Nature Materials*, 7(4):326–332, 2008. doi: 10.1038/nmat2119.

[10] J. Rivnay, L. H. Jimison, J. E. Northrup, M. F. Toney, R. Noriega, S. Lu, T. J. Marks, A. Facchetti, and A. Salleo. Large modulation of carrier transport by grain-boundary molecular packing and microstructure in organic thin films. *Nature Materials*, 8(12):952–958, December 2009. doi: 10.1038/nmat2570.

[11] J. E. Anthony. Organic electronics - addressing challenges. *Nature materials*, 13(8): 773–775, July 2014. doi: 10.1038nmat4034.

[12] S. H. Kang and M. D. Dickey. Patterning via self-organization and self-folding: Beyond conventional lithography. *MRS Bulletin*, 41(02):93–96, February 2016. doi: 10.1557/mrs.2016.3.

[13] S. Kowarik, A. Gerlach, and F. Schreiber. Organic molecular beam deposition: fundamentals, growth dynamics, and in situ studies. *Journal of Physics: Condensed Matter*, 20(18):184005, May 2008. doi: 10.1088/0953-8984/20/18/184005.

[14] D. Käfer, L. Ruppel, G. Witte, and C. Wöll. Role of molecular conformations in rubrene thin film growth. *Phys. Rev. Lett.*, 95:166602, October 2005. doi: 10.1103/PhysRevLett.95.166602.

[15] J. A. DeFranco, B. S. Schmidt, M. Lipson, and G. G. Malliaras. Photolithographic patterning of organic electronic materials. *Organic Electronics*, 7(1):22–28, February 2006. doi: 10.1016/j.orgel.2005.10.002.

[16] J. Jang, Y. Song, D. Yoo, C. K. Ober, J.-K. Lee, and T. Lee. The development of fluorous photolithographic materials and their applications to achieve flexible organic electronic devices. *Flexible and Printed Electronics*, 1(2):023001, June 2016. doi: 10.1088/2058-8585/1/2/023001.

[17] Y. Yamamoto, H. Ichikawa, K. Ueno, a. Koma, K. Saiki, and T. Shimada. Morphological change of C_{60} monolayer epitaxial films under photoexcitation. *Physical Review B*, 70(15):155415, October 2004. doi: 10.1103/PhysRevB.70.155415.

[18] A. Sander, R. Hammer, K. Duncker, S. Förster, and W. Widdra. Thermally and photoinduced polymerization of ultrathin sexithiophene films. *The Journal of chemical physics*, 141(10):104704, September 2014. doi: 10.1063/1.4894437.

[19] K. Sugi, H. Ishii, Y. Kimura, M. Niwano, E. Ito, Y. Washizu, N. Hayashi, Y. Ouchi, and K. Seki. Characterization of light-erasable giant surface potential built up in evaporated Alq_3 thin films. *Thin Solid Films*, 464-465:412–415, October 2004. doi: 10.1016/j.tsf.2004.06.035.

[20] F. Balzer and H.-G. Rubahn. Laser-controlled growth of needle-shaped organic nanoaggregates. *Nano Letters*, 2(7):747–750, July 2002. doi: 10.1021/nl0255707.

[21] L. Chen, O. Cherniavskaya, A. Shalek, and L. E. Brus. Photoinduced interfacial charging and "explosion" of monolayer pentacene islands. *Nano letters*, 5(11): 2241–5, November 2005. doi: 10.1021/nl051567m.

[22] H. Ichikawa, K. Saiki, T. Suzuki, T. Hasegawa, and T. Shimada. Uniaxial alignment of Alq_3 by laser-assisted molecular beam epitaxy. *Japanese Journal of Applied*

Physics, 44(No. 49):L1469–L1471, November 2005. doi: 10.1143/JJAP.44.L1469.

[23] G. Fang, J. Maclennan, Y. Yi, M. Glaser, M. Farrow, E. Korblova, D. Walba, T. Furtak, and N. Clark. Athermal photofluidization of glasses. *Nature Communications*, 4: 1521, February 2013. doi: 10.1038/ncomms2483.

[24] N. Kawatsuki. Photoalignment and photoinduced molecular reorientation of photosensitive materials. *Chemistry Letters*, 40(6):548–554, 2011. doi: 10.1246/cl.2011.548.

[25] S. R. Forrest. Ultrathin organic films grown by organic molecular beam deposition and related techniques. *Chemical Reviews*, 97(6):1793–1896, October 1997.

[26] G. Rosenfeld, B. Poelsema, and G. Comsa. The concept of two mobilities in homoepitaxial growth. *Journal of Crystal Growth*, 151(1-2):230–233, May 1995. doi: 10.1016/0022-0248(95)00077-1.

[27] G. Rosenfeld, B. Poelsema, and G. Comsa. Epitaxial growth modes far from equilibrium. In D. King and D. P. Woodruff, editors, *Growth and Properties of Ultrathin Epitaxial Layers*, chapter 3. Elsevier, 1997. doi: 10.1016/S1571-0785(97)80006-5.

[28] H. Brune. Epitaxial growth of thin films. In K. Wandelt, editor, *Surface and Interface Science*, chapter 20, pages 421–492. Wiley-VCH, Weinheim, Germany, November 2014. doi: 10.1002/9783527680566.ch20.

[29] S. Bommel, N. Kleppmann, C. Weber, H. Spranger, P. Schäfer, J. Novak, S. Roth, F. Schreiber, S. Klapp, and S. Kowarik. Unravelling the multilayer growth of the fullerene C_{60} in real time. *Nature Communications*, 5:5388, 2014. doi: 10.1038/ncomms6388.

[30] Y. M. Yu and B. G. Liu. Phase-field model of island growth in epitaxy. *Physical Review E - Statistical, Nonlinear, and Soft Matter Physics*, 69:1–6, 2004. doi: 10.1103/PhysRevE.69.021601.

[31] M. Kraus, S. Richler, A. Opitz, W. Brütting, S. Haas, T. Hasegawa, A. Hinderhofer, and F. Schreiber. High-mobility copper-phthalocyanine field-effect transistors with tetratetracontane passivation layer and organic metal contacts. *Journal of Applied Physics*, 107(9):094503, 2010. doi: 10.1063/1.3354086.

[32] S. Ogawa, Y. Kimura, M. Niwano, and H. Ishii. Trap elimination and injection switching at organic field effect transistor by inserting an alkane C_{44} H_{90} layer. *Applied Physics Letters*, 90(3):033504, 2007. doi: 10.1063/1.2431713.

[33] P. Lazar, H. Schollmeyer, and H. Riegler. Spreading and two-dimensional mobility of long-chain alkanes at solid/gas interfaces. *Physical Review Letters*, 94(11):116101, March 2005. doi: 10.1103/PhysRevLett.94.116101.

[34] H. Schollmeyer, B. Struth, and H. Riegler. Long chain n -alkanes at SiO_2/air interfaces: Molecular ordering, annealing, and surface freezing of triacontane in the case of excess and submonolayer coverage. *Langmuir*, 19(12):5042–5051, June

2003. doi: 10.1021/la026989f.

[35] B. M. Ocko, X. Z. Wu, E. B. Sirota, S. K. Sinha, O. Gang, and M. Deutsch. Surface freezing in chain molecules: Normal alkanes. *Physical Review E*, 55(3):3164–3182, 1997. doi: 10.1103/PhysRevE.55.3164.

[36] B. Saleh and M. Teich. *Fundamentals of Photonics*. John Wiley & Sons, Hoboken, New Jersey, 2013. ISBN 9781118585818.

[37] G. Lanzani. *The Photophysics Behind Photovoltaics and Photonics*. Wiley-VCH, Weinheim, Germany, 2012. ISBN 9783527410545.

[38] W. Demtröder. *Molekülphysik: Theoretische Grundlagen und experimentelle Methoden*. De Gruyter, Berlin, Germany, 2013. ISBN 9783486714890.

[39] J. Michl and E. Thulstrup. *Spectroscopy with Polarized Light: Solute Alignment by Photoselection, Liquid Crystal, Polymers, and Membranes*. VCH Publishers, New York, 1986. ISBN 9780471186243.

[40] A. Nefedov and C. Wöll. Advanced applications of nexafs spectroscopy for functionalized surfaces. In G. Bracco and B. Holst, editors, *Surface Science Techniques*, chapter 10, pages 277–303. Springer, Berlin, Heidelberg, 2013. ISBN 978-3-642-34243-1. doi: 10.1007/978-3-642-34243-1_10.

[41] M. S. Gordon and M. W. Schmidt. Advances in electronic structure theory. In *Theory and Applications of Computational Chemistry*, pages 1167–1189. Elsevier, 2005. doi: 10.1016/B978-044451719-7/50084-6.

[42] B. Botter, C. Nonhof, J. Schmidt, and J. van der Waals. The “mini-exciton” in the $C_{10}H_8$ naphthalene pair in a $AC_{10}D_8$ host as studied by electron spin echo and odmr techniques. *Chemical Physics Letters*, 43(2):210–216, October 1976. doi: 10.1016/0009-2614(76)85287-6.

[43] A. S. Davydov. The theory of molecular excitons. *Soviet Physics Uspekhi*, 7(2): 145–178, February 1964. doi: 10.1070/PU1964v007n02ABEH003659.

[44] M. Kasha, H. R. Rawls, and M. Ashraf El-Bayoumi. The exciton model in molecular spectroscopy. *Pure and Applied Chemistry*, 11(3-4):371–392, January 1965. doi: 10.1351/pac196511030371.

[45] M. Klessinger and J. Michl. *Excited states and photochemistry of organic molecules*. VCH Publishers, New York, 1995. ISBN 9781560815884.

[46] J. Wright. *Molecular Crystals*. Cambridge University Press, 1995. ISBN 9780521477307.

[47] T. Tsurumi, H. Hirayama, M. Vacha, and T. Taniyama. *Nanoscale Physics for Materials Science*. CRC Press, Boca Raton, USA, 2009. ISBN 9781439800607.

[48] P. Peumans, S. Uchida, and S. R. Forrest. Efficient bulk heterojunction photovoltaic cells using small-molecular-weight organic thin films. *Nature*, 425(6954):158–162, September 2003. doi: 10.1038/nature01949.

[49] P. Beyer, T. Breuer, S. Ndiaye, A. Zykov, A. Viertel, M. Gensler, J. P. Rabe, S. Hecht, G. Witte, and S. Kowarik. Lattice matching as the determining factor for molecular tilt and multilayer growth mode of the nanographene hexa-peri-hexabenzocoronene. *ACS Applied Materials & Interfaces*, 6(23):21484–21493, December 2014. doi: 10.1021/am506465b.

[50] S. Blumstengel, H. Glowatzki, S. Sadofev, N. Koch, S. Kowarik, J. P. Rabe, and F. Henneberger. Band-offset engineering in organic/inorganic semiconductor hybrid structures. *Physical Chemistry Chemical Physics*, 12(37):11642, 2010. doi: 10.1039/c004944c.

[51] S. Kowarik, A. Gerlach, S. Sellner, F. Schreiber, L. Cavalcanti, and O. Konovalov. Real-time observation of structural and orientational transitions during growth of organic thin films. *Physical Review Letters*, 96(12):1–4, March 2006. doi: 10.1103/PhysRevLett.96.125504.

[52] V. C. Sundar, J. Zaumseil, V. Podzorov, E. Menard, R. L. Willett, T. Someya, M. E. Gershenson, and J. A. Rogers. Elastomeric transistor stamps : Transport in organic crystals. *Science*, 303(March):1644–1646, 2004.

[53] M. M. Ling, C. Reese, A. L. Briseno, and Z. Bao. Non-destructive probing of the anisotropy of field-effect mobility in the rubrene single crystal. *Synthetic Metals*, 157(6-7):257–260, 2007. doi: 10.1016/j.synthmet.2007.02.004.

[54] O. Ostroverkhova, D. G. Cooke, F. a. Hegmann, R. R. Tykwinski, S. R. Parkin, and J. E. Anthony. Anisotropy of transient photoconductivity in functionalized pentacene single crystals. *Applied Physics Letters*, 89(19):1–3, 2006. doi: 10.1063/1.2387135.

[55] G. Witte and C. Wöll. Growth of aromatic molecules on solid substrates for applications in organic electronics. *Journal of Materials Research*, 19(07):1889–1916, 2004. doi: 10.1557/JMR.2004.0251.

[56] T. Breuer, M. A. Celik, P. Jakob, R. Tonner, and G. Witte. Vibrational davydov splittings and collective mode polarizations in oriented organic semiconductor crystals. *Journal of Physical Chemistry C*, 116(27):14491–14503, 2012. doi: 10.1021/jp304080g.

[57] T. Kampen. *Low Molecular Weight Organic Semiconductors*. Wiley-VCH, Weinheim, Germany, 2011. ISBN 9783527643745.

[58] T. Seki, S. Nagano, and M. Hara. Versatility of photoalignment techniques: From nematics to a wide range of functional materials. *Polymer (United Kingdom)*, 54(22): 6053–6072, 2013. doi: 10.1016/j.polymer.2013.08.058.

[59] O. Yaroshchuk and Y. Reznikov. Photoalignment of liquid crystals: basics and current trends. *Journal of Materials Chemistry*, 22(2):286, 2012. doi: 10.1039/c1jm13485j.

[60] T. Fujiwara, J. Locklin, and Z. Bao. Solution deposited liquid crystalline semiconductors on a photoalignment layer for organic thin-film transistors.

Applied Physics Letters, 90(23):232108, 2007. doi: 10.1063/1.2746937.

[61] S. Liu, W. M. Wang, A. L. Briseno, S. C. B. Mannsfeld, and Z. Bao. Controlled deposition of crystalline organic semiconductors for field-effect-transistor applications. *Advanced Materials*, 21(12):1217–1232, 2009. doi: 10.1002/adma.200802202.

[62] S. Kowarik, K. Broch, and F. Schreiber. Beim wachstum zusehen. *Physik Journal*, 12: 33, 2014.

[63] K. Jackson. *Kinetic Processes: Crystal Growth, Diffusion, and Phase Transitions in Materials*. John Wiley & Sons, New York, 2010. ISBN 9783527327362.

[64] J. Bernstein. *Polymorphism in Molecular Crystals*. IUCr monographs on crystallography. OUP Oxford, 2007. ISBN 9780199236565.

[65] R. G. Della Valle, E. Venuti, A. Brillante, and A. Girlando. Are crystal polymorphs predictable? The case of sexithiophene. *The journal of physical chemistry. A*, 112 (29):6715–22, July 2008. doi: 10.1021/jp801749n.

[66] S. Iannotta and T. Toccoli. Supersonic molecular beam growth of thin films of organic materials: A novel approach to controlling the structure, morphology, and functional properties. *Journal of Polymer Science Part B: Polymer Physics*, 41(21): 2501–2521, November 2003. doi: 10.1002/polb.10644.

[67] C. Westermeier, A. Cernescu, S. Amarie, C. Liewald, F. Keilmann, and B. Nickel. Sub-micron phase coexistence in small-molecule organic thin films revealed by infrared nano-imaging. *Nature communications*, 5(May):4101, 2014. doi: 10.1038/ncomms5101.

[68] C. Ambrosch-Draxl, D. Nabok, P. Puschnig, and C. Meisenbichler. The role of polymorphism in organic thin films: oligoacenes investigated from first principles. *New Journal of Physics*, 11(12):125010, 2009. doi: 10.1088/1367-2630/11/12/125010.

[69] E. Zojer, N. Koch, P. Puschnig, F. Meghdadi, A. Niko, R. Resel, C. Ambrosch-Draxl, M. Knupfer, J. Fink, J. Brédas, and G. Leising. Structure, morphology, and optical properties of highly ordered films of para-sexiphenyl. *Physical Review B*, 61(24): 16538–16549, June 2000. doi: 10.1103/PhysRevB.61.16538.

[70] A. O. F. Jones, B. Chattopadhyay, Y. H. Geerts, and R. Resel. Substrate-induced and thin-film phases: Polymorphism of organic materials on surfaces. *Advanced Functional Materials*, 26(14):2233–2255, 2016. doi: 10.1002/adfm.201503169.

[71] M. Sparenberg, A. Zykov, P. Beyer, L. Pithan, C. Weber, Y. Garmshausen, F. Carlà, S. Hecht, S. Blumstengel, F. Henneberger, and S. Kowarik. Controlling the growth mode of para-sexiphenyl (6p) on ZnO by partial fluorination. *Physical chemistry chemical physics : PCCP*, 16(47):26084–93, December 2014. doi: 10.1039/c4cp04048a.

[72] S. Kowarik, A. Gerlach, S. Sellner, L. Cavalcanti, O. Konovalov, and F. Schreiber. Real-time x-ray diffraction measurements of structural dynamics and polymorphism in diindenoperylene growth. *Applied Physics A*, 95(1):233–239,

December 2008. doi: 10.1007/s00339-008-5012-2.

[73] G. Nan and Z. Li. Modeling of charge transport in polycrystalline sexithiophene from quantum charge transfer rate theory beyond the first-order perturbation. *Organic Electronics*, 12(12):2198–2206, December 2011. doi: 10.1016/j.orgel.2011.09.018.

[74] Y. Diao, B. C.-K. Tee, G. Giri, J. Xu, D. H. Kim, H. a. Becerril, R. M. Stoltenberg, T. H. Lee, G. Xue, S. C. B. Mannsfeld, and Z. Bao. Solution coating of large-area organic semiconductor thin films with aligned single-crystalline domains. *Nature materials*, 12(7):665–71, July 2013. doi: 10.1038/nmat3650.

[75] S. Tavazzi, L. Silvestri, and P. Spearman. Optical properties of molecular crystals : The effect of molecular packing and polymorphism. In E. Borisenko, editor, *Crystallization and Materials Science of Modern Artificial and Natural Crystals*. InTech, 2008. doi: 10.5772/30671.

[76] L. Pithan, C. Cocchi, H. Zschiesche, C. Weber, A. Zykov, S. Bommel, S. J. Leake, P. Schäfer, C. Draxl, and S. Kowarik. Light controls polymorphism in thin films of sexithiophene. *Crystal Growth & Design*, 15(3):1319–1324, March 2015. doi: 10.1021/cg501734w.

[77] B. Gumí-Audenis, F. Carlà, M. V. Vitorino, A. Panzarella, L. Porcar, M. Boilot, S. Guerber, P. Bernard, M. S. Rodrigues, F. Sanz, M. I. Giannotti, and L. Costa. Custom AFM for x-ray beamlines: in situ biological investigations under physiological conditions. *Journal of Synchrotron Radiation*, 22(6):1364–1371, Nov 2015. doi: 10.1107/S1600577515016318.

[78] D. M. Smilgies, N. Boudet, B. Struth, and O. Konovalov. Troika II: a versatile beamline for the study of liquid and solid interfaces. *Journal of Synchrotron Radiation*, 12(3):329–339, May 2005. doi: 10.1107/S0909049505000361.

[79] C. Nicklin, T. Arnold, J. Rawle, and A. Warne. Diamond beamline I07: a beamline for surface and interface diffraction. *Journal of Synchrotron Radiation*, 23(5): 1245–1253, September 2016. doi: 10.1107/S1600577516009875.

[80] P. R. Willmott, D. Meister, S. J. Leake, M. Lange, A. Bergamaschi, M. Böge, M. Calvi, C. Cancellieri, N. Casati, A. Cervellino, Q. Chen, C. David, U. Flechsig, F. Gozzo, B. Henrich, S. Jäggi-Spielmann, B. Jakob, I. Kalichava, P. Karvinen, J. Krempasky, A. Lüdeke, R. Lüscher, S. Maag, C. Quitmann, M. L. Reinle-Schmitt, T. Schmidt, B. Schmitt, A. Streun, I. Vartiainen, M. Vitins, X. Wang, and R. Wullschleger. The materials science beamline upgrade at the swiss light source. *Journal of synchrotron radiation*, 20(Pt 5):667–82, September 2013. doi: 10.1107/S0909049513018475.

[81] A. Buffet, A. Rothkirch, R. Döhrmann, V. Körstgens, M. M. Abul Kashem, J. Perlich, G. Herzog, M. Schwartzkopf, R. Gehrke, P. Müller-Buschbaum, and S. V. Roth. P03, the microfocus and nanofocus x-ray scattering (minaxs) beamline of the petra iii storage ring: The microfocus endstation. *Journal of Synchrotron Radiation*, 19(4): 647–653, 2012. doi: 10.1107/S0909049512016895.

[82] J. Als-Nielsen and D. McMorrow. *Elements of Modern X-Ray Physics*. John Wiley & Sons, 2011. ISBN 0470973951.

[83] C. Ponchut. Characterization of x-ray area detectors for synchrotron beamlines. *Journal of Synchrotron Radiation*, 13(2):195–203, Mar 2006. doi: 10.1107/S0909049505034278.

[84] I. K. Robinson and D. J. Tweet. Surface x-ray diffraction. *Reports on Progress in Physics*, 55(5):599–651, May 1992. doi: 10.1088/0034-4885/55/5/002.

[85] J. Als-Nielsen and D. McMorrow. *Elements of Modern X-Ray Physics*. John Wiley & Sons, West Sussex, England, 2011. ISBN 0470973951.

[86] M. Tolan. *X-Ray Scattering from Soft-Matter Thin Films*, volume 148 of *Springer Tracts in Modern Physics*. Springer Berlin Heidelberg, 1999. ISBN 978-3-540-65182-6. doi: 10.1007/BFb0112834.

[87] S. Kowarik, A. Hinderhofer, A. Gerlach, and F. Schreiber. Modeling of thin film deposition based on real-time observation. In Z. Cao, editor, *Thin film growth*, chapter 7. Woodhead Publishing, 2011. ISBN 978-1845697365.

[88] C. Weber, C. Frank, S. Bommel, T. Rukat, W. Leitenberger, P. Schäfer, F. Schreiber, and S. Kowarik. Chain-length dependent growth dynamics of n-alkanes on silica investigated by energy-dispersive x-ray reflectivity in situ and in real-time. *The Journal of Chemical Physics*, 136(20):204709, 2012. doi: 10.1063/1.4719530.

[89] V. I. Trofimov, J. Kim, and S. Bae. Temperature behavior of the growth mechanism during layer epitaxial growth. *Journal of Physics: Conference Series*, 100(8):082005, March 2008. doi: 10.1088/1742-6596/100/8/082005.

[90] V. I. Trofimov and V. G. Mokerov. Rate equations model for layer epitaxial growth kinetics. *Thin Solid Films*, 428(1-2):66–71, 2003. doi: 10.1016/S0040-6090(02)01272-5.

[91] J. A. Venables, G. D. T. Spiller, and M. Hanbucken. Nucleation and growth of thin films. *Reports on Progress in Physics*, 47(4):399–459, April 1984. doi: 10.1088/0034-4885/47/4/002.

[92] A. R. Woll, T. V. Desai, and J. R. Engstrom. Quantitative modeling of in situ x-ray reflectivity during organic molecule thin film growth. *arXiv.org*, 1102.2676, February 2011.

[93] F.-J. Meyer zu Heringdorf, M. C. Reuter, and R. M. Tromp. Growth dynamics of pentacene thin films. *Nature*, 412(6846):517–520, August 2001. doi: 10.1038/35087532.

[94] V. I. Trofimov, J. Kim, and S. Bae. Influence of two different adatom mobilities on the initial heteroepitaxial growth kinetics. *Surface Science*, 601(18):4465–4469, 2007. doi: 10.1016/j.susc.2007.04.143.

[95] H. Dosch. *Critical Phenomena at Surfaces and Interfaces*, volume 126 of *Springer Tracts in Modern Physics*. Springer-Verlag, Berlin/Heidelberg, 1992. ISBN 3-540-54534-4. doi: 10.1007/BFb0045209.

[96] T. Joo Shin and H. Yang. Grazing incidence x-ray diffraction (gixd). In Z. Bao and J. Locklin, editors, *Organic Field-Effect Transistors*, pages 253–276. Taylor & Francis, 2007. ISBN 978-0-8493-8080-8. doi: 10.1201/9781420008012.ch4.1.

[97] A. Hinderhofer, T. Hosokai, K. Yonezawa, A. Gerlach, K. Kato, K. Broch, C. Frank, J. Novák, S. Kera, N. Ueno, and F. Schreiber. Post-growth surface smoothing of thin films of diindenoperylene. *Applied Physics Letters*, 101(3):033307, 2012.

[98] C. Lorch, R. Banerjee, C. Frank, J. Dieterle, A. Hinderhofer, A. Gerlach, and F. Schreiber. Growth of competing crystal phases of α-sexithiophene studied by real-time in situ x-ray scattering. *The Journal of Physical Chemistry C*, 119(1): 819–825, January 2015. doi: 10.1021/jp510321k.

[99] D. M. Smilgies, N. Boudet, and H. Yanagi. In-plane alignment of para-sexiphenyl films grown on KCl (001). *Applied Surface Science*, 189(1-2):24–30, April 2002. doi: 10.1016/S0169-4332(01)01029-7.

[100] D. W. Bennett. *Understanding Single-Crystal X-Ray Crystallography*. Wiley-VCH, Weinheim, Germany, 2010. ISBN 978-3-527-32794-2.

[101] B. Arndt, R. Bliem, O. Gamba, J. E. van der Hoeven, H. Noei, U. Diebold, G. S. Parkinson, and A. Stierle. Atomic structure and stability of magnetite fe3o4(001): An x-ray view. *Surface Science*, 653:76 – 81, 2016. doi: http://dx.doi.org/10.1016/j.susc.2016.06.002.

[102] S. Bommel. Phd thesis: Unravelling nanoscale molecular processes in organic thin films; submitted to HU Berlin, Mathematisch-Naturwissenschaftliche Fakultät. 2015. URL http://edoc.hu-berlin.de/docviews/abstract.php?id=42048.

[103] L. Pithan. Master thesis: Structure, optical properties and light-controlled molecular selfassembly of organic thin films; submitted to TU Berlin. 2013.

[104] A. Gibaud, G. Vignaud, and S. K. Sinha. The correction of geometrical factors in the analysis of x-ray reflectivity. *Acta Crystallographica Section A*, 49(4):642–648, Jul 1993. doi: 10.1107/S0108767392013126.

[105] P. Müller-Buschbaum. Applications of synchrotron light to scattering and diffraction in materials and life sciences. In M. Gomez, A. Nogales, M. C. Garcia-Gutierrez, and T. Ezquerra, editors, *Lecture Notes in Physics*, volume 776, pages 61–89. Springer, Berlin, Heidelberg, 2009. ISBN 978-3-540-95967-0. doi: 10.1007/978-3-540-95968-7.

[106] C. Frank, J. Novák, R. Banerjee, A. Gerlach, F. Schreiber, A. Vorobiev, and S. Kowarik. Island size evolution and molecular diffusion during growth of organic thin films followed by time-resolved specular and off-specular scattering. *Physical Review B*, 90(4):045410, July 2014. doi: 10.1103/PhysRevB.90.045410.

[107] C. Durniak, M. Ganeva, G. Pospelov, W. Van Herck, and J. Wuttke. *BornAgain - Software for simulating and fitting x-ray and neutron small-angle scattering at grazing incidence*, 2015. URL http://www.bornagainproject.org.

[108] R. Lazzari. IsGISAXS: a program for grazing-incidence small-angle x-ray scattering analysis of supported islands. *Journal of Applied Crystallography*, 35(4):406–421, August 2002. doi: 10.1107/S0021889802006088.

[109] D. Babonneau. FitGISAXS: software package for modelling and analysis of GISAXS data using IGOR Pro. *Journal of Applied Crystallography*, 43(4):929–936, August 2010. doi: 10.1107/S0021889810020352.

[110] A. Zykov, S. Bommel, C. Wolf, L. Pithan, C. Weber, P. Beyer, G. Santoro, J. P. Rabe, and S. Kowarik. Diffusion and nucleation in multilayer growth of PTCDI-C_8 studied with in situ x-ray growth oscillations and real-time small angle x-ray scattering. *Journal of Chemical Physics*, 146(5):052803, February 2017. doi: 10.1063/1.4961460.

[111] C. Frank, R. Banerjee, M. Oettel, A. Gerlach, J. Novák, G. Santoro, and F. Schreiber. Analysis of island shape evolution from diffuse x-ray scattering of organic thin films and implications for growth. *Physical Review B*, 90(20):205401, November 2014. doi: 10.1103/PhysRevB.90.205401.

[112] J. I. Langford and D. Louër. Powder diffraction. *Reports on Progress in Physics*, 59(2): 131–234, February 1996. doi: 10.1088/0034-4885/59/2/002.

[113] R. J. Hill and C. J. Howard. Quantitative phase analysis from neutron powder diffraction data using the rietveld method. *Journal of Applied Crystallography*, 20 (6):467–474, December 1987. doi: 10.1107/S0021889887086199.

[114] R. Forker, M. Gruenewald, and T. Fritz. Optical differential reflectance spectroscopy on thin molecular films. *Annual Reports Section "C" (Physical Chemistry)*, 108:34–68, 2012. doi: 10.1039/c2pc90002e.

[115] U. Heinemeyer. Phd thesis: Optical properties of organic semiconductor thin films : Static spectra and real-time growth studies; submitted to Universität Tübingen, Fakultät für Mathematik und Physik. 2009. URL http://tobias-lib.uni-tuebingen.de/volltexte/2009/4122/pdf/Dissertation_Heinemeyer_online.pdf.

[116] J. McIntyre and D. Aspnes. Differential reflection spectroscopy of very thin surface films. *Surface Science*, 24(2):417–434, February 1971. doi: 10.1016/0039-6028(71)90272-X.

[117] S. B. Kaemmer. Introduction to brukers scanasyst and peakforce tapping atomic force microscopy technology AFM. *Bruker Nano Surfaces Division Application Notes*, 133, 2011.

[118] G. Binnig, C. F. Quate, and C. Gerber. Atomic force microscope. *Physical Review Letters*, 56(9):930–933, March 1986. doi: 10.1103/PhysRevLett.56.930.

[119] D. Johnson, N. Hilal, and W. R. Bowen. Chapter 1 - basic principles of atomic force microscopy. In W. R. Bowen and N. Hilal, editors, *Atomic Force Microscopy in Process Engineering*, pages 1 – 30. Butterworth-Heinemann, Oxford, 2009. ISBN 978-1-85617-517-3. doi: http://dx.doi.org/10.1016/B978-1-85617-517-3.00001-8.

[120] G. Haugstad. *Atomic Force Microscopy: Understanding Basic Modes and Advanced Applications*. John Wiley & Sons, New York, 2012. ISBN 9781118360682.

[121] P. Eaton and P. West. *Atomic Force Microscopy*. OUP Oxford, 2010. ISBN 9780191576676.

[122] E. W. Weisstein. *Fourier Transform. From MathWorld - A Wolfram Web Resource*, accessed 24.08.2016. URL http://mathworld.wolfram.com/FourierTransform.html.

[123] R. Köhler, P. Lazar, and H. Riegler. Optical imaging of thin films with molecular depth resolution. *Applied Physics Letters*, 89(24):241906, 2006. doi: 10.1063/1.2404601.

[124] M. A. Green. Self-consistent optical parameters of intrinsic silicon at 300k including temperature coefficients. *Solar Energy Materials and Solar Cells*, 92(11): 1305–1310, November 2008. doi: 10.1016/j.solmat.2008.06.009.

[125] N. Kleppmann and S. H. L. Klapp. Particle-resolved dynamics during multilayer growth of C_{60}. *Physical Review B*, 91(4):045436, January 2015. doi: 10.1103/PhysRevB.91.045436.

[126] J. Papac, D. Margetis, F. Gibou, and C. Ratsch. Island-dynamics model for mound formation: Effect of a step-edge barrier. *Physical Review E*, 90(2):022404, 2014. doi: 10.1103/PhysRevE.90.022404.

[127] R. Backofen and A. Voigt. A cellular automata algorithm for step dynamics in continuum modeling of epitaxial growth. *Journal of Crystal Growth*, 303(1): 100–104, May 2007. doi: 10.1016/j.jcrysgro.2006.11.336.

[128] R. E. Caflisch. Growth, structure and pattern formation for thin films. *Journal of Scientific Computing*, 37(1):3–17, October 2008. doi: 10.1007/s10915-008-9206-8.

[129] J. Evans, P. Thiel, and M. Bartelt. Morphological evolution during epitaxial thin film growth: Formation of 2d islands and 3d mounds. *Surface Science Reports*, 61 (1-2):1–128, April 2006. doi: 10.1016/j.surfrep.2005.08.004.

[130] Y. M. Yu and B. G. Liu. Self-organized formation of regular nanostripes on vicinal surfaces. *Physical Review B - Condensed Matter and Materials Physics*, 70(20):1–7, 2004. doi: 10.1103/PhysRevB.70.205414.

[131] Y. M. Yu, R. Backofen, and A. Voigt. Phase-field simulation of stripe arrays on metal bcc(110) surfaces. *Physical Review E - Statistical, Nonlinear, and Soft Matter Physics*, 77(5):1–7, 2008. doi: 10.1103/PhysRevE.77.051605.

[132] F. Ming and A. Zangwill. Phase field modeling of submonolayer epitaxial growth. *Physical Review B*, 81(23):1–5, 2010. doi: 10.1103/PhysRevB.81.235431.

[133] B. Klett, C. Cocchi, L. Pithan, S. Kowarik, and C. Draxl. Polymorphism in α-sexithiophene crystals: relative stability and transition path. *Phys. Chem. Chem. Phys.*, 18(21):14603–14609, 2016. doi: 10.1039/C6CP01405D.

[134] D. Fichou. Structural order in conjugated oligothiophenes and its implications on

opto-electronic devices. *Journal of Materials Chemistry*, 10(3):571–588, 2000. doi: 10.1039/a908312j.

[135] U. Hörmann, J. Wagner, M. Gruber, A. Opitz, and W. Brütting. Approaching the ultimate open circuit voltage in thiophene based single junction solar cells by applying diindenoperylene as acceptor. *physica status solidi (RRL) - Rapid Research Letters*, 5(7):241–243, July 2011. doi: 10.1002/pssr.201105238.

[136] A. Opitz, J. Wagner, W. Brütting, I. Salzmann, N. Koch, J. Manara, J. Pflaum, A. Hinderhofer, and F. Schreiber. Charge separation at molecular donor–acceptor interfaces: Correlation between morphology and solar cell performance. *IEEE Journal of Selected Topics in Quantum Electronics*, 16(6):1707–1717, November 2010. doi: 10.1109/JSTQE.2010.2048096.

[137] T. Siegrist, R. Fleming, R. Haddon, R. Laudise, A. Lovinger, H. Katz, P. Bridenbaugh, and D. Davis. The crystal structure of the high-temperature polymorph of α–hexathienyl (α–6T/HT). *Journal of Materials Research*, 10(09):2170–2173, March 1995. doi: 10.1557/JMR.1995.2170.

[138] A. Lovinger, D. Davis, R. Ruel, L. Torsi, A. Dodabalapur, and H. Katz. Morphology of α-hexathienyl thin-film-transistor films. *Journal of Materials Research*, 10(11): 2958–2962, March 1995. doi: 10.1557/JMR.1995.2958.

[139] B. Servet, G. Horowitz, S. Ries, O. Lagorsse, P. Alnot, A. Yassar, F. Deloffre, P. Srivastava, and R. Hajlaoui. Polymorphism and charge transport in vacuum-evaporated sexithiophene films. *Chemistry of Materials*, 6(10):1809–1815, October 1994. doi: 10.1021/cm00046a039.

[140] E. Umbach, W. Gebauer, A. Soukopp, M. Bässler, and M. Sokolowski. New insight in the optical properties of ultrathin oligothiophene films by epitaxial preparation. *Journal of Luminescence*, 76-77(97):641–651, February 1998. doi: 10.1016/S0022-2313(97)00170-1.

[141] J.-O. Vogel, I. Salzmann, R. Opitz, S. Duhm, B. Nickel, J. P. Rabe, and N. Koch. Sub-nanometer control of the interlayer spacing in thin films of intercalated rodlike conjugated molecules. *The journal of physical chemistry. B*, 111(51): 14097–101, December 2007. doi: 10.1021/jp077158r.

[142] S. Trabattoni, M. Moret, M. Campione, L. Raimondo, and A. Sassella. Epitaxial growth of organic semiconductor polymorphs on natural amino acid single crystals. *Crystal Growth & Design*, 13(10):4268–4278, October 2013. doi: 10.1021/cg400481h.

[143] G. Schwabegger, T. Djuric, H. Sitter, R. Resel, and C. Simbrunner. Morphological and structural investigation of sexithiophene growth on KCl (100). *Crystal growth & design*, 13(2):536–542, February 2013. doi: 10.1021/cg3010823.

[144] C. Simbrunner. Epitaxial growth of sexi-thiophene and para-hexaphenyl and its implications for the fabrication of self-assembled lasing nano-fibres. *Semiconductor Science and Technology*, 28(5):053001, May 2013. doi: 10.1088/0268-1242/28/5/053001.

[145] M. A. Loi, E. D. Como, F. Dinelli, M. Murgia, R. Zamboni, F. Biscarini, and M. Muccini. Supramolecular organization in ultra-thin films of α-sexithiophene on silicon dioxide. *Nature Materials*, 4(1):81–85, December 2004. doi: 10.1038/nmat1279.

[146] E. Da Como, M. A. Loi, M. Murgia, R. Zamboni, and M. Muccini. J-aggregation in alpha-sexithiophene submonolayer films on silicon dioxide. *Journal of the American Chemical Society*, 128(13):4277–81, April 2006. doi: 10.1021/ja056060s.

[147] G. Horowitz, B. Bachet, A. Yassar, P. Lang, F. Demanze, J.-l. Fave, and F. Garnier. Growth and characterization of sexithiophene single crystals. *Chemistry of Materials*, 7:1337–1341, July 1995. doi: 10.1021/cm00055a010.

[148] A. Soyer. Fhkl – a program to compute rocking curves and crystallographic data of interest for the dynamical theory of x-rays. *Journal of Applied Crystallography*, 28 (2):244–244, April 1995. doi: 10.1107/S0021889894013397.

[149] A. Gulans, S. Kontur, C. Meisenbichler, D. Nabok, P. Pavone, S. Rigamonti, S. Sagmeister, U. Werner, and C. Draxl. Exciting: a full-potential all-electron package implementing density-functional theory and many-body perturbation theory. *Journal of physics. Condensed matter : an Institute of Physics journal*, 26(36): 363202, September 2014. doi: 10.1088/0953-8984/26/36/363202.

[150] D. Fichou, G. Horowitz, B. Xu, and F. Garnier. Low temperature optical absorption of polycrystalline thin films of α-quaterthiophene, α-sexithiophene and α-octithiophene, three model oligomers of polythiophene. *Synthetic Metals*, 48(2): 167–179, July 1992. doi: 10.1016/0379-6779(92)90059-R.

[151] X. Cheng, K. Ichimura, D. Fichou, and T. Kobayashi. Nanosecond time-resolved absorption spectra of thin films of α-conjugated thiophene oligomers. *Chemical Physics Letters*, 185(3-4):286–291, October 1991. doi: 10.1016/S0009-2614(91)85061-Z.

[152] A. Salleo. Organic electronics: Something out of nothing. *Nature Materials*, 14(11): 1077–1078, September 2015. doi: 10.1038/nmat4420.

[153] S. C. McEldowney, D. M. Shemo, R. A. Chipman, and P. K. Smith. Creating vortex retarders using photoaligned liquid crystal polymers. *Optics Letters*, 33(2):134, January 2008. doi: 10.1364/OL.33.000134.

[154] N. Yu and F. Capasso. Flat optics with designer metasurfaces. *Nature Materials*, 13 (2):139–150, 2014. doi: 10.1038/nmat3839.

[155] P. Rotter, B. A. J. Lechner, A. Morherr, D. M. Chisnall, D. J. Ward, A. P. Jardine, J. Ellis, W. Allison, B. Eckhardt, and G. Witte. Coupling between diffusion and orientation of pentacene molecules on an organic surface. *Nature Materials*, 15(4): 397–400, February 2016. doi: 10.1038/nmat4575.

[156] S.-H. Jin, H.-U. Seo, D.-H. Nam, W. S. Shin, J.-H. Choi, U. C. Yoon, J.-W. Lee, J.-G. Song, D.-M. Shin, and Y.-S. Gal. Surface-induced alignment of pentacene by photo-alignment technology for organic thin film transistors. *Journal of Materials*

Chemistry, 15(47):5029–5036, 2005. doi: 10.1039/b510731h.

[157] V. Y. Gayvoronsky, S. V. Yakunin, V. M. Pergamenshchik, and V. G. Nazarenko. Sign inversion of the optical torque on the nematic director enhanced by anthraquinone dye dopants stable to the light action. *Laser Physics Letters*, 3(11):531–535, November 2006. doi: 10.1002/lapl.200610049.

[158] W. M. Gibbons, P. J. Shannon, S.-T. Sun, and B. J. Swetlin. Surface-mediated alignment of nematic liquid crystals with polarized laser light. *Nature*, 351(6321): 49–50, May 1991. doi: 10.1038/351049a0.

[159] A. Pick and G. Witte. Patterned growth of organic semiconductors: Selective nucleation of perylene on self-assembled monolayers. *Langmuir*, 32(32):8019–8028, August 2016. doi: 10.1021/acs.langmuir.6b01833.

[160] I. Martín-Fabiani, E. Rebollar, M. C. García-Gutiérrez, D. R. Rueda, M. Castillejo, and T. A. Ezquerra. Mapping the structural order of laser-induced periodic surface structures in thin polymer films by microfocus beam grazing incidence small-angle x-ray scattering. *ACS Applied Materials & Interfaces*, 7(5):3162–3169, February 2015. doi: 10.1021/am5074968.

[161] Z. Sekkat, J. Wood, W. Knoll, W. Volksen, R. D. Miller, and A. Knoesen. Light-induced orientation in azo-polyimide polymers 325 °C below the glass transition temperature. *Journal of the Optical Society of America B*, 14(4):829–833, April 1997. doi: 10.1364/JOSAB.14.000829.

[162] S. Tavazzi, L. Raimondo, L. Silvestri, P. Spearman, A. Camposeo, M. Polo, and D. Pisignano. Dielectric tensor of tetracene single crystals: The effect of anisotropy on polarized absorption and emission spectra. *The Journal of Chemical Physics*, 128 (15):154709, 2008. doi: 10.1063/1.2897436.

[163] M. J. Y. Tayebjee, R. G. C. R. Clady, and T. W. Schmidt. The exciton dynamics in tetracene thin films. *Physical Chemistry Chemical Physics*, 15(35):14797, September 2013. doi: 10.1039/c3cp52609g.

[164] S. Tavazzi and M. Campione. Variable-angle ellipsometry and molecular orientation in monoclinic organic semiconductors. *Applied Physics Letters*, 88(7): 071918, 2006. doi: 10.1063/1.2173254.

[165] B. Gompf, D. Faltermeier, C. Redling, M. Dressel, and J. Pflaum. Tetracene film morphology: Comparative atomic force microscopy, x-ray diffraction and ellipsometry investigations. *The European Physical Journal E*, 27(4):421–424, December 2008. doi: 10.1140/epje/i2008-10405-5.

[166] D. Holmes, S. Kumaraswamy, A. J. Matzger, and K. P. C. Vollhardt. On the nature of nonplanarity in the [n]phenylenes. *Chemistry European Journal*, 5(11):3399–3412, November 1999. doi: 10.1002/(SICI)1521-3765(19991105)5:11<3399::AID-CHEM3399>3.0.CO;2-V.

[167] S. Milita, C. Santato, and F. Cicoira. Structural investigation of thin tetracene films on flexible substrate by synchrotron x-ray diffraction. *Applied Surface Science*, 252

(22):8022–8027, September 2006. doi: 10.1016/j.apsusc.2006.04.028.

[168] S. Milita, M. Servidori, F. Cicoira, C. Santato, and A. Pifferi. Synchrotron x-ray investigation of tetracene thin films grown at different deposition fluxes. *Nuclear Instruments and Methods in Physics Research B*, 246(1):101–105, May 2006. doi: 10.1016/j.nimb.2005.12.042.

[169] D. H. Arias, J. L. Ryerson, J. D. Cook, N. H. Damrauer, and J. C. Johnson. Polymorphism influences singlet fission rates in tetracene thin films. *Chem. Sci.*, 7 (2):1185–1191, 2016. doi: 10.1039/C5SC03535J.

[170] B. Schatschneider, S. Monaco, A. Tkatchenko, and J.-J. Liang. Understanding the structure and electronic properties of molecular crystals under pressure: Application of dispersion corrected DFT to oligoacenes. *The Journal of Physical Chemistry A*, 117(34):8323–8331, August 2013. doi: 10.1021/jp406573n.

[171] T. Hahn and H. Klapper. Twinning of crystals. In *International Tables for Crystallography*, volume D, pages 393–448. International Union of Crystallography, Chester, England, October 2006. ISBN 978-1-4020-0714-9. doi: 10.1107/97809553602060000644.

[172] A. Bekshaev, M. Soskin, and M. Vasnecov. *Paraxial light beams with angular momenum*. Nova Science Publ., New York, 2008. ISBN 9781604561142.

[173] E. Higurashi, R. Sawada, and T. Ito. Optically induced angular alignment of birefringent micro-objects by linear polarization. *Applied Physics Letters*, 73(21): 3034, 1998. doi: 10.1063/1.122663.

[174] E. Higurashi, R. Sawada, and T. Ito. Optically induced angular alignment of trapped birefringent micro-objects by linearly polarized light. *Physical Review E*, 59(3): 3676–3681, March 1999. doi: 10.1103/PhysRevE.59.3676.

[175] I. Jánossy. Molecular interpretation of the absorption-induced optical reorientation of nematic liquid crystals. *Physical Review E*, 49(4):2957–2963, April 1994. doi: 10.1103/PhysRevE.49.2957.

[176] E. M. Grumstrup, J. C. Johnson, and N. H. Damrauer. Enhanced triplet formation in polycrystalline tetracene films by femtosecond optical-pulse shaping. *Physical Review Letters*, 105(25):257403, December 2010. doi: 10.1103/PhysRevLett.105.257403.

[177] W. Brütting. Light-emitting organic crystal field-effect transistors for future organic injection lasers. In C. Adachi, editor, *Physics of Organic Semiconductors*. Wiley-VCH, Weinheim, Germany, 2 edition, January 2013. ISBN 9783527410538. doi: 10.1002/9783527654949.ch18.

[178] M. Muccini. A bright future for organic field-effect transistors. *Nature Materials*, 5 (8):605–613, August 2006. doi: 10.1038/nmat1699.

[179] S. Pratontep, M. Brinkmann, F. Nüesch, and L. Zuppiroli. Nucleation and growth of ultrathin pentacene films on silicon dioxide: Effect of deposition rate and substrate

temperature. *Synthetic Metals*, 146(3):387–391, 2004. doi: 10.1016/j.synthmet.2004.08.017.

[180] P. R. Ribič, V. Kalihari, C. D. Frisbie, and G. Bratina. Growth of ultrathin pentacene films on polymeric substrates. *Physical Review B*, 80(11):115307, September 2009. doi: 10.1103/PhysRevB.80.115307.

[181] T. Potocar, S. Lorbek, D. Nabok, Q. Shen, L. Tumbek, G. Hlawacek, P. Puschnig, C. Ambrosch-Draxl, C. Teichert, and A. Winkler. Initial stages of a para-hexaphenyl film growth on amorphous mica. *Physical Review B*, 83(7):075423, February 2011. doi: 10.1103/PhysRevB.83.075423.

[182] G. Rosenfeld, N. N. Lipkin, W. Wulfhekel, J. Kliewer, K. Morgenstern, B. Poelsema, and G. Comsa. New concepts for controlled homoepitaxy. *Applied Physics A Materials Science & Processing*, 61(5):455–466, November 1995. doi: 10.1007/BF01540247.

[183] T. Michely and J. Krug. *Islands, Mounds and Atoms.* Springer Series in Surface Sciences. Springer Berlin Heidelberg, 2012. ISBN 9783642186721.

[184] P. Šmilauer and S. Harris. Determination of step-edge barriers to interlayer transport from surface morphology during the initial stages of homoepitaxial growth. *Physical Review B*, 51(20):14798–14801, May 1995. doi: 10.1103/PhysRevB.51.14798.

[185] T. N. Krauss, E. Barrena, D. G. de Oteyza, X. N. Zhang, J. Major, V. Dehm, F. Würthner, and H. Dosch. x-ray/atomic force microscopy study of the temperature-dependent multilayer structure of PTCDI-C_8 films on SiO_2. *The Journal of Physical Chemistry C*, 113(11):4502–4506, March 2009. doi: 10.1021/jp808037w.

[186] T. N. Krauss, E. Barrena, X. N. Zhang, D. G. de Oteyza, J. Major, V. Dehm, F. Würthner, L. P. Cavalcanti, and H. Dosch. Three-dimensional molecular packing of thin organic films of PTCDI-C_8 determined by surface x-ray diffraction. *Langmuir*, 24(22):12742–12744, November 2008. doi: 10.1021/la8030182.

[187] B. Y. Stadnyk and E. Antonyuk. Termoelectric cooling modules. *Journal of Thermoelectricity*, 97, 1994.

[188] L. Pithan, E. Meister, C. Jin, C. Weber, A. Zykov, K. Sauer, W. Brütting, H. Riegler, A. Opitz, and S. Kowarik. Thermally driven smoothening of molecular thin films: Structural transitions in n-alkane layers studied in real-time. *Journal of Chemical Physics*, 143(16), 2015. doi: 10.1063/1.4934501.

[189] O. A. Melville, B. H. Lessard, and T. P. Bender. Phthalocyanine-based organic thin-film transistors: A review of recent advances. *ACS Applied Materials & Interfaces*, 7(24):13105–13118, June 2015. doi: 10.1021/acsami.5b01718.

[190] A. Zen, P. Pingel, D. Neher, and U. Scherf. Organic transistors utilising highly soluble swivel-cruciform oligothiophenes. *Physica Status Solidi A*, 205(3):440–448, March 2008. doi: 10.1002/pssa.200723504.

[191] S. R. Craig, G. P. Hastie, K. J. Roberts, and J. N. Sherwood. Investigation into the structures of some normal alkanes within the homologous series $C_{13}H_{28}$ to $C_{60}H_{122}$ using high-resolution synchrotron x-ray powder diffraction. *Journal of Materials Chemistry*, 4(6):977–891, 1994. doi: 10.1039/jm9940400977.

[192] A. Holzwarth, S. Leporatti, and H. Riegler. Molecular ordering and domain morphology of molecularly thin triacontane films at SiO_2/air interfaces. *Europhysics Letters (EPL)*, 52(6):653–659, December 2000. doi: 10.1209/epl/i2000-00488-0.

[193] C. Merkl, T. Pfohl, and H. Riegler. Influence of the molecular ordering on the wetting of SiO_2/air interfaces by alkanes. *Physical Review Letters*, 79(23):4625–4628, December 1997. doi: 10.1103/PhysRevLett.79.4625.

[194] J. L. Lee, E. M. Pearce, and T. K. Kwei. Morphological development in alkyl-substituted semiflexible polymers. *Macromolecules*, 30(26):8233–8244, 1997. doi: 10.1021/ma970647c.

[195] C. Weber, T. Liebig, M. Gensler, L. Pithan, S. Bommel, D. Bléger, J. P. Rabe, S. Hecht, and S. Kowarik. Light-controlled "molecular zippers" based on azobenzene main chain polymers. *Macromolecules*, 48(5):1531–1537, March 2015. doi: 10.1021/ma502551b.

[196] M. Göllner, M. Huth, and B. Nickel. Pentacene thin-film transistors encapsulated by a thin alkane layer operated in an aqueous ionic environment. *Advanced materials (Deerfield Beach, Fla.)*, 22(39):4350–4, October 2010. doi: 10.1002/adma.201001345.

[197] D.-I. Kim, T. Quang Trung, B.-U. Hwang, J.-S. Kim, S. Jeon, J. Bae, J.-J. Park, and N.-E. Lee. A sensor array using multi-functional field-effect transistors with ultrahigh sensitivity and precision for bio-monitoring. *Scientific Reports*, 5:12705, 2015. doi: 10.1038/srep12705.

[198] M. Irimia-Vladu, E. D. Gåowacki, P. a. Troshin, G. Schwabegger, L. Leonat, D. K. Susarova, O. Krystal, M. Ullah, Y. Kanbur, M. a. Bodea, V. F. Razumov, H. Sitter, S. Bauer, and N. S. Sariciftci. Indigo - a natural pigment for high performance ambipolar organic field effect transistors and circuits. *Advanced Materials*, 24(3): 375–380, 2012. doi: 10.1002/adma.201102619.

[199] M. Horlet, M. Kraus, W. Brütting, and A. Opitz. Diindenoperylene as ambipolar semiconductor: Influence of electrode materials and mobility asymmetry in organic field-effect transistors. *Applied Physics Letters*, 98(23):233304, 2011. doi: 10.1063/1.3598423.

[200] M. Kraus, S. Haug, W. Brütting, and A. Opitz. Achievement of balanced electron and hole mobility in copper-phthalocyanine field-effect transistors by using a crystalline aliphatic passivation layer. *Organic Electronics*, 12(5):731–735, May 2011. doi: 10.1016/j.orgel.2011.02.001.

[201] A. Opitz and W. Brütting. Ambipolar charge-carrier transport in molecular field-effect transistors. In W. Brütting and C. Adachi, editors, *Physics of Organic*

Semiconductors, pages 239–265. Wiley-VCH, Weinheim, Germany, January 2013. doi: 10.1002/9783527654949.ch8.

[202] M. Dirand, M. Bouroukba, A.-J. Briard, V. Chevallier, D. Petitjean, and J.-P. Corriou. Temperatures and enthalpies of (solid + solid) and (solid + liquid) transitions of n-alkanes. *The Journal of Chemical Thermodynamics*, 34(8):1255–1277, August 2002. doi: 10.1006/jcht.2002.0978.

[203] J.-p. Gorce, S. J. Spells, X.-b. Zeng, and G. Ungar. Infrared active methyl group vibrations in tetratetracontane: A probe for chain end organization and crystal structure. *The Journal of Physical Chemistry B*, 108(10):3130–3139, March 2004. doi: 10.1021/jp030794e.

[204] A. Müller. An x-ray investigation of normal paraffins near their melting points. *Proceedings of the Royal Society A: Mathematical, Physical and Engineering Sciences*, 138(836):514–530, December 1932. doi: 10.1098/rspa.1932.0200.

[205] A. Müller. The crystal structure of the normal paraffins at temperatures ranging from that of liquid air to the melting points. *Proceedings of the Royal Society A: Mathematical, Physical and Engineering Sciences*, 127(805):417–430, May 1930. doi: 10.1098/rspa.1930.0068.

[206] O. Phaovibul, H. Čačković, J. Loboda-Čačković, and R. Hosemann. Phase transition and paracrystalline order in solution-crystallized solid n-paraffins. *Journal of Polymer Science Part A-2: Polymer Physics*, 11(12):2377–2391, December 1973. doi: 10.1002/pol.1973.180111207.

[207] P. K. Sullivan. Solid-phase behavior of several long-chain n-paraffins, esters, and a ketone. *Journal of Research of the NBS Section A: Physics and Chemistry*, 78A(2):129, March 1974. doi: 10.6028/jres.078A.009.

[208] P. K. Sullivan and J. J. Weeks. The intensity as a function of temperature of the low-angle x-ray diffraction maxima of the n-paraffins: Hexatriacontane, tetratetracontane, and tetranonacontane. *Journal of Research of the NBS Section A: Physics and Chemistry*, 74A(2):203, March 1970. doi: 10.6028/jres.074A.015.

[209] B. G. Rånby, F. F. Morehead, and N. M. Walter. Morphology of n-alkanes, linear polyethylene, and isotactic polypropylene crystallized from solution. *Journal of Polymer Science*, 44(144):349–367, June 1960. doi: 10.1002/pol.1960.1204414407.

[210] A.-j. Briard, M. Bouroukba, D. Petitjean, N. Hubert, and M. Dirand. Experimental enthalpy increments from the solid phases to the liquid phase of homologous n-alkane series (C_{18} to C_{38} and C_{41}, C_{44}, C_{46}, C_{50}, C_{54}, and C_{60}). *Journal of Chemical & Engineering Data*, 48(3):497–513, May 2003. doi: 10.1021/je0201368.

[211] A. Tkachenko and Y. Rabin. Fluctuation-stabilized surface freezing of chain molecules. *Physical Review Letters*, 76(14):2527–2530, 1996. doi: 10.1103/PhysRevLett.76.2527.

[212] B. M. Ocko, E. B. Sirota, M. Deutsch, E. DiMasi, S. Coburn, J. Strzalka, S. Zheng, A. Tronin, T. Gog, and C. Venkataraman. Positional order and thermal expansion of

surface crystalline n -alkane monolayers. *Physical Review E*, 63(3):032602, February 2001. doi: 10.1103/PhysRevE.63.032602.

[213] D. Nečas and P. Klapetek. Gwyddion: an open-source software for spm data analysis. *Open Physics*, 10(1):181–188, January 2012. doi: 10.2478/s11534-011-0096-2.

[214] O. Balmes, R. van Rijn, D. Wermeille, a. Resta, L. Petit, H. Isern, T. Dufrane, and R. Felici. The id03 surface diffraction beamline for in-situ and real-time x-ray investigations of catalytic reactions at surfaces. *Catalysis Today*, 145(3-4):220–226, 2009. doi: 10.1016/j.cattod.2009.02.008.

[215] M. Bai, K. Knorr, M. J. Simpson, S. Trogisch, H. Taub, S. N. Ehrlich, H. Mo, U. G. Volkmann, and F. Y. Hansen. Nanoscale observation of delayering in alkane films. *Europhysics Letters (EPL)*, 79(2):26003, July 2007. doi: 10.1209/0295-5075/79/26003.

[216] H. Schollmeyer, B. Ocko, and H. Riegler. Surface freezing of triacontane at SiO_x/air interfaces: Submonolayer coverage. *Langmuir*, 18(11):4351–4355, May 2002. doi: 10.1021/la011620w.

[217] W. Rasband. *ImageJ*, 2015. URL http://imagej.nih.gov/ij/.

[218] C. Wagner. Theorie der Alterung von Niederschlägen durch Umlösen. *Z. Elektrochem.*, 65:581–591, 1961. doi: 10.1002/bbpc.19610650704.

[219] T. Ji, S. Jung, and V. K. Varadan. On the correlation of postannealing induced phase transition in pentacene with carrier transport. *Organic Electronics*, 9(5):895–898, October 2008. doi: 10.1016/j.orgel.2008.03.005.

[220] R. Ye, M. Baba, K. Suzuki, Y. Ohishi, and K. Mori. Effect of thermal annealing on morphology of pentacene thin films. *Japanese Journal of Applied Physics*, 42(Part 1, No. 7A):4473–4475, 2003. doi: 10.1143/JJAP.42.4473.

[221] B. Krause, A. C. D ürr, F. Schreiber, H. Dosch, and O. H. Seeck. Thermal stability and partial dewetting of crystalline organic thin films: 3,4,9,10-perylenetetracarboxylic dianhydride on Ag (111). *The Journal of Chemical Physics*, 119(6):3429, 2003. doi: 10.1063/1.1589471.

[222] S. Kowarik, A. Gerlach, W. Leitenberger, J. Hu, G. Witte, C. Wöll, U. Pietsch, and F. Schreiber. Energy-dispersive x-ray reflectivity and gid for real-time growth studies of pentacene thin films. *Thin Solid Films*, 515(14):5606–5610, May 2007. doi: 10.1016/j.tsf.2006.12.020.

[223] P. Bennema, X. Y. Liu, K. Lewtas, R. Tack, J. Rijpkema, and K. Roberts. Morphology of orthorhombic long chain normal alkanes: theory and observations. *Journal of Crystal Growth*, 121(4):679–696, 1992. doi: 10.1016/0022-0248(92)90575-4.

[224] P. van Hoof, R. Grimbergen, H. Meekes, W. van Enckevort, and P. Bennema. Morphology of orthorhombic n-paraffin crystals: a comparison between theory and experiments. *Journal of Crystal Growth*, 191(4):861–872, 1998. doi: 10.1016/S0022-0248(98)00374-1.

[225] T. Kakudate, N. Yoshimoto, and Y. Saito. Polymorphism in pentacene thin films on sio2 substrate. *Applied Physics Letters*, 90(8):081903, 2007. doi: 10.1063/1.2709516.

[226] A. Gavezzotti. Efficient computer modeling of organic materials. the atom–atom, coulomb–london–pauli (AA-CLP) model for intermolecular electrostatic-polarization, dispersion and repulsion energies. *New Journal of Chemistry*, 35(7):1360–1368, 2011. doi: 10.1039/c0nj00982b.

[227] C. Yang, S. Li, and J. Armellin. Size and temperature dependence of phase stability in nanocrystalline pentacene thin films. *Journal of Physical Chemistry C*, 111(47): 17512–17515, November 2007. doi: 10.1021/jp073505l.

[228] L. F. Drummy, P. K. Miska, D. Alberts, N. Lee, and D. C. Martin. Imaging of crystal morphology and molecular simulations of surface energies in pentacene thin films. *The journal of physical chemistry. B*, 110(12):6066–6071, 2006. doi: 10.1021/jp054951g.

[229] X. Z. Wu, B. M. Ocko, E. B. Sirota, S. K. Sinha, M. Deutsch, B. H. Cao, and M. W. Kim. Surface tension measurements of surface freezing in liquid normal alkanes. *Science (New York, N.Y.)*, 261(5124):1018–21, August 1993. doi: 10.1126/science.261.5124.1018.

[230] J. E. Goose, K. Wong, P. Clancy, and M. O. Thompson. Direct melt processing of pentacene at temperatures above 1000 °C by pulsed laser irradiation. *Applied Physics Letters*, 93(18):10–13, 2008. doi: 10.1063/1.3009289.

[231] R. Ruiz, B. Nickel, N. Koch, L. C. Feldman, R. F. Haglund, A. Kahn, F. Family, and G. Scoles. Dynamic scaling, island size distribution, and morphology in the aggregation regime of submonolayer pentacene films. *Physical review letters*, 91 (13):136102, 2003. doi: 10.1103/PhysRevLett.91.136102.

[232] J. A. Meyer, J. Vrijmoeth, H. A. van der Vegt, E. Vlieg, and R. J. Behm. Importance of the additional step-edge barrier in determining film morphology during epitaxial growth. *Physical Review B*, 51(20):14790–14793, May 1995. doi: 10.1103/PhysRevB.51.14790.

[233] I. Markov. Method for evaluation of the ehrlich-schwoebel barrier to interlayer transport in metal homoepitaxy. *Physical Review B*, 54(24):17930–17937, December 1996. doi: 10.1103/PhysRevB.54.17930.

[234] K. Bromann, H. Brune, H. Röder, and K. Kern. Interlayer mass transport in homoepitaxial and heteroepitaxial metal growth. *Physical Review Letters*, 75(4): 677–680, July 1995. doi: 10.1103/PhysRevLett.75.677.

[235] J. Villain, A. Pimpinelli, and D. Wolf. Layer by layer growth in molecular beam epitaxy. *Comments Cond. Mat. Phys*, 16(1):1–18, 1992.

[236] J. E. Goose, E. L. First, and P. Clancy. Nature of step-edge barriers for small organic molecules. *Physical Review B*, 81(20):205310, May 2010. doi: 10.1103/PhysRevB.81.205310.

IV

Appendix

A

Additional Experimental Results

A.1. Sexithiophene

A.1.1. Needle Shaped LT Phase Crystallites with Flat Lying Molecular Orientation

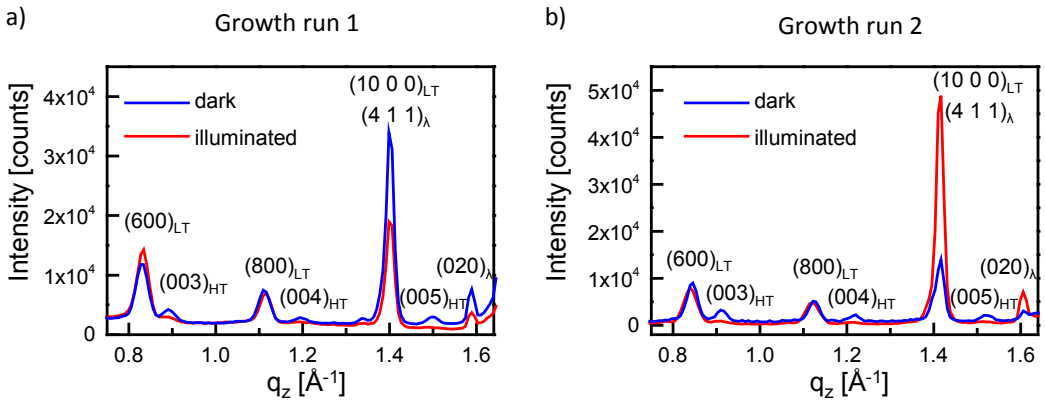

Figure A.1: $\theta/2\theta$- scan of 6T thin films grown at 60°C with and without illumination on four different substrates. Independent of substrate we find a reduction of the HT phase with respect to the LT phase for standing molecules in the experiments in a) and b). For the flat lying molecules no systematic effect of the laser is found with a reduction of flat lying molecules upon illumination in a) and an increase in b).

For crystallites of flat lying molecules the microscopic structure of the KCl substrate surface and not the laser illumination seems to play a dominant role with respect to the amount of molecules crystallising in this orientation. All measurements presented in

Figure A.1 were conducted on samples grown under similar conditions on four different, cleaved KCl crystals. In the first batch of substrates (in Figure A.1a)) more flat lying molecules (which only occur in the LT phase) are found on the sample grown in the dark, whereas in the second batch (in Figure A.1b)) more lying molecules are found in the illuminated case, so that no clear trend due to illumination is obvious. However, the reflections originating from upright standing molecules behave similarly in both sets of measurements, that is there exists a robust light induced effect on the coexistence ratio for standing upright molecules as discussed in the main paper.

A.1.2. Rocking Width of Out-of-Plane Reflections

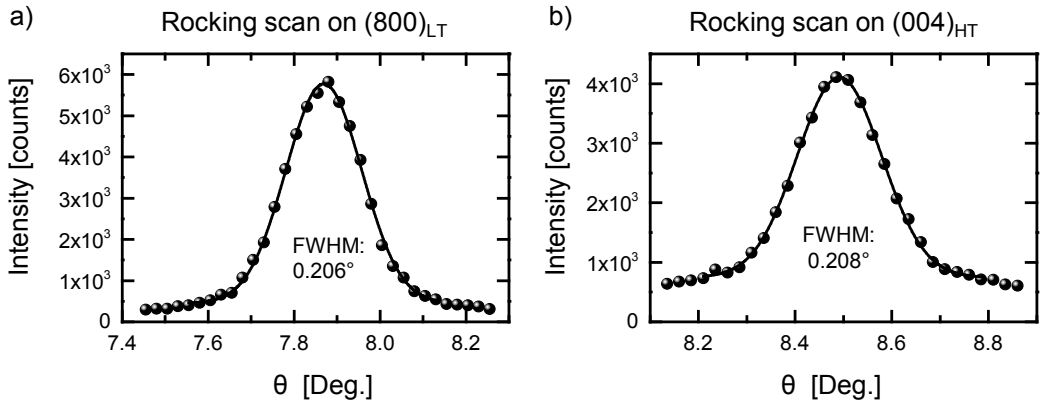

FIGURE A.2: Rocking scans of the $(800)_{LT}$ reflection in a) and the $(004)_{HT}$ reflection in b) on a sample grown under illumination at 60°C.

Due to the identical rocking width of the $(00l)_{HT}$ resp. $(k00)_{LT}$ reflection, it is appropriate to use the intensity of a $\theta - 2\theta$ scan as measure for the integrated intensity. In Figure A.2 we exemplarily show the rocking curve of the $(800)_{LT}$ and $(004)_{HT}$ reflections for a 6T film grown at 60°C under illumination. We observed no influence of the illumination on the rocking width.

A.2. Light Induced Shift in Phase-Coexistence in Pentacene Thin Films

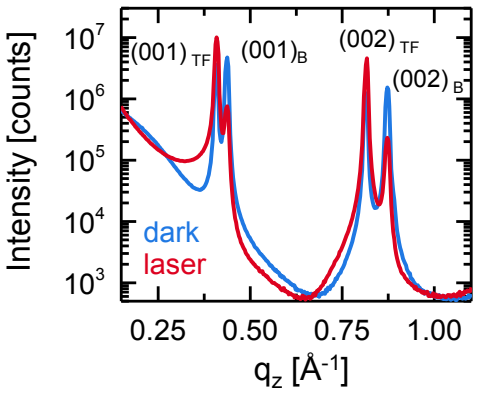

FIGURE A.3: Phase coexistence in pentacene thin films grown under 532 *nm* illumination and in the dark. We find a strong shift in the form bulk phase crystallites towards more thin film phase content.

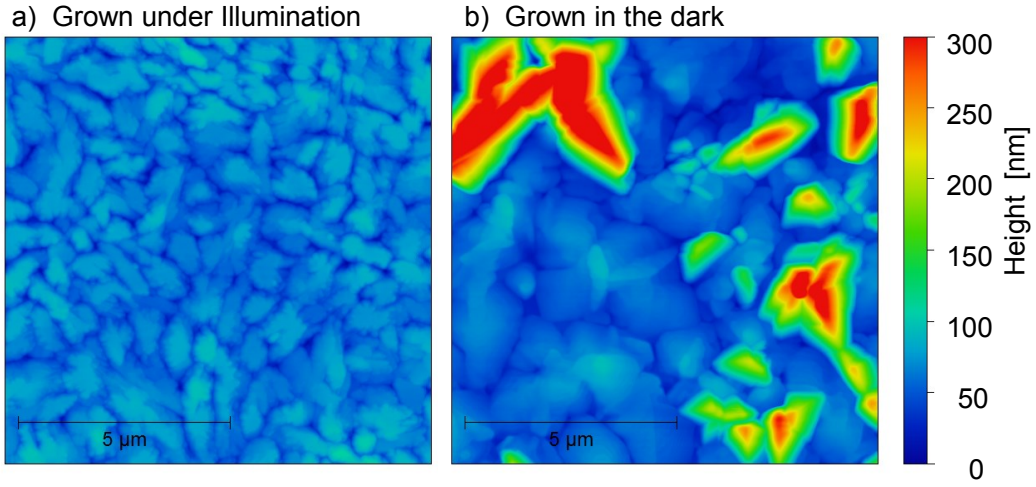

FIGURE A.4: AFM images of pentacene thin films grown under illumination and in the dark. The overall surface morphology changes towards smaller structures under illumination. Furthermore, there are no additional crystal grains lying on top of the film as in the case of films grown in the dark.

Preliminary results on the influence of illumination on the thin film growth of the organic semiconductor pentacene ($C_{14}H_{22}$) also indicate a shift in crystal-phase coexistence ratio similar to the observation presented in Chapter 4 for 6T. In Figure A.3 the (001) reflection of the pentacene thin film phase and bulk phase[1] are shown for films grown to a thickness

[1] for unit cell parameter please see Table 5.1 in Chapter 5

of 100 nm at 8.5 Å$/min$ and $T_{sub} = 70\,°C$. Under illumination (532 nm, $p \approx 3\,W/cm^2$), we observe a strong decrease in the relative intensity of bulk phase reflection while the intensity of the thin film phase reflection increases by a factor of 6.
Accompanying AFM images (Figure A.4) show a decrease in molecular island sizes under illumination and a reduction of pentacene crystallites that lie on top of the film. It is worth mentioning that for pentacene films of submonolayer coverage a *photoinduced explosion* has been observed by Chen *et al.* at even lower power densities.[21] The authors of this study attribute their observation to an electrical charging of the pentacene film. To what extend their model is also applicable to illumination during multilayer grow has not been evaluated so far.

The comparison of rocking scans (also known as ω−scans) of samples grown with and without illumination (Figure A.5) is particular interesting around the bulk phase reflection. Other than in ref. [231], where the rocking scans are performed near the critical angle, the scans presented here are measured around the first and second order out-of-plane Bragg reflections. The here observed satellite peaks cannot be attributed to an in-plane length scale. The q_x component according to the satellite peaks significantly differs for the $(001)_{\text{Bulk}}$ and $(002)_{\text{Bulk}}$. We rather find that the angular offset between the specular reflection and the satellite peaks is $\approx 0.8°$ for both reflections. Therefore, we tentatively assign these satellite peaks to molecular crystallites that have a contact plane with the underlying silica substrate that differs from the *ab*-plane of the molecular unit cell.

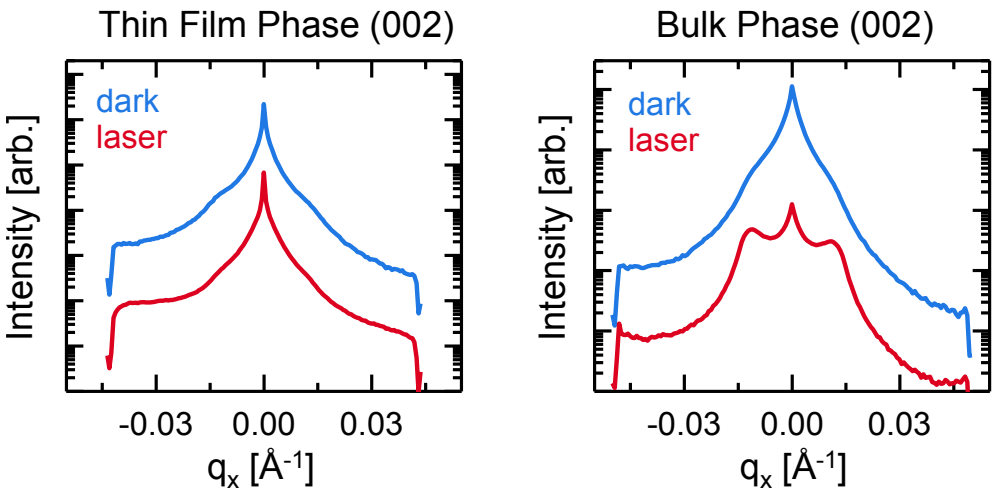

Figure A.5: Rocking scans around the (002) reflections of TF and Bulk phase. Under illumination the bulk phase reflection features two pronounced satellite peaks.

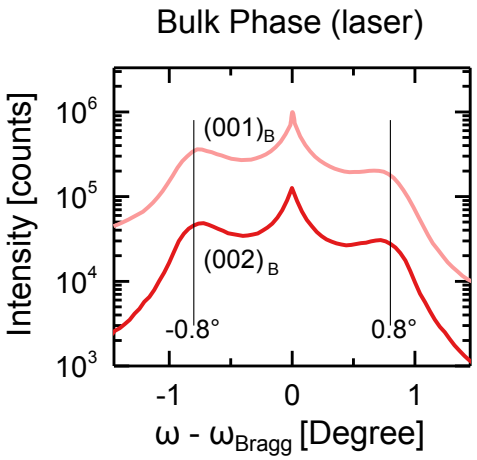

FIGURE A.6: Comparison of rocking scans around the $(001))_{\text{Bulk}}$ and $(002)_{\text{Bulk}}$ reflections reveals that the satellite peaks rather lie at a constant angular offset for both reflections (0.8°) than at constant q_x.

A.3. PTCDI-C_8

A.3.1. First Monolayer Island Density of PTCDI-C_8 on Silica

In continuation of Figure 6.9 here we show additional AFM micrographs of the growth of PTCDI-C_8 on silica with sub-monolayer coverages in Figure A.7. For the first monolayer we find based on AFM an island density of $55.0\,\mu m^{-2}$ which lies an order of magnitude above the value for the second monolayer island density of $7,9\,\mu m^{-2}$ at $100\,^{\circ}C$. We also find that the first ML almost closes completely (> 98% coverage) before the second layer starts to grow. Due due the high initial island density in the first monolayer on the bare substrate and we did not perform any temperature cycle during the nucleation phase of the first monolayer in the optimised temperature scheme discussed in Chapter 6.

A.3.2. PTCDI-C_8 Growth with Temperature Modulations Between 70°C and 35°C

For the films shown in Figure A.8 we emplyed a different temperature scheme: Here we grew the samples at $70\,^{\circ}C$ base temperature and cool down the substrate to $35\,^{\circ}C$ during the cooling cycle with a deposition rate of $\approx 1.3\,\text{Å}/min$. These measurements are performed at a laboratory x-ray source (rotating anode, Cu-K_α). From the critical layer coverages based on the rate equation model (Equation 3.3) in Table A.1 we conclude that there is a persistent influence of the temperature modulations on the surface roughness even for thicker films compared to those discussed in Chapter 6.

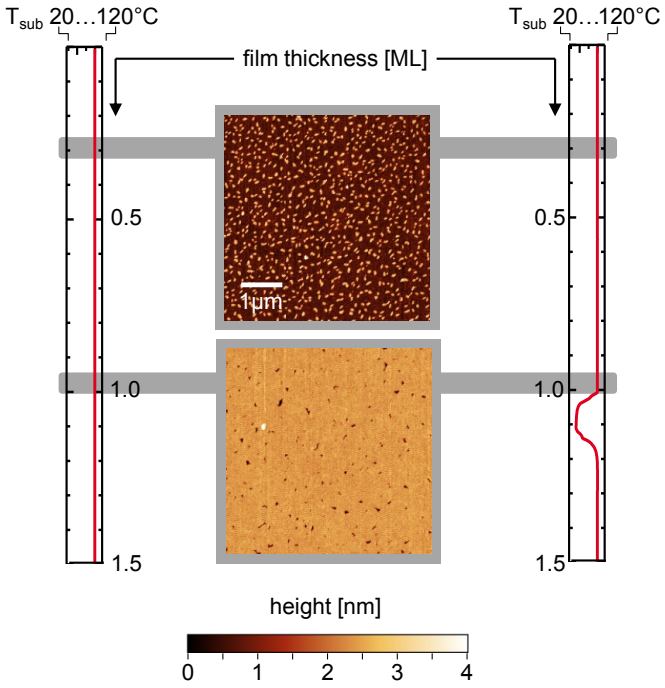

FIGURE A.7: AFM micrographs ($5 \times 5\,\mu m$) of sub-monolayer coverages of PTCDI-C_8 on silica. The island density at 0.3 ML coverage lies with $55.0\,\mu m^{-2}$ about one order of magnitude higher than what we observe in the second monolayer for the growth of PTCDI-C_8 on PTCDI-C_8 .

	const. 70°C	T_{mod} 70°C/35°C
$\theta_{1,\mathrm{crit}}$ [norm.]	66.0%	66.0 %
$\theta_{2,\mathrm{crit}}$ [norm.]	29.0%	45.9 %
$\theta_{3,\mathrm{crit}}$ [norm.]	28.7%	39.1 %
$\theta_{4,\mathrm{crit}}$ [norm.]	19.2%	32.4 %
$\theta_{5,\mathrm{crit}}$ [norm.]	19.2%	32.1 %
$\theta_{6,\mathrm{crit}}$ [norm.]	16.8%	24.1 %
layer spacing 1ML [Å]	20.4	20.4
layer spacing upper MLs [Å]	20.5	20.5
q_z [Å^{-1}]	0.154	0.154

TABLE A.1.: Critical layer coverages and simulation parameters to fit the data shown in Figure A.8 using the rate equation model. The critical layer coverages of the film grown under temperature modulations are increased by ≈ 10% compared to the film grown at constant temperature.

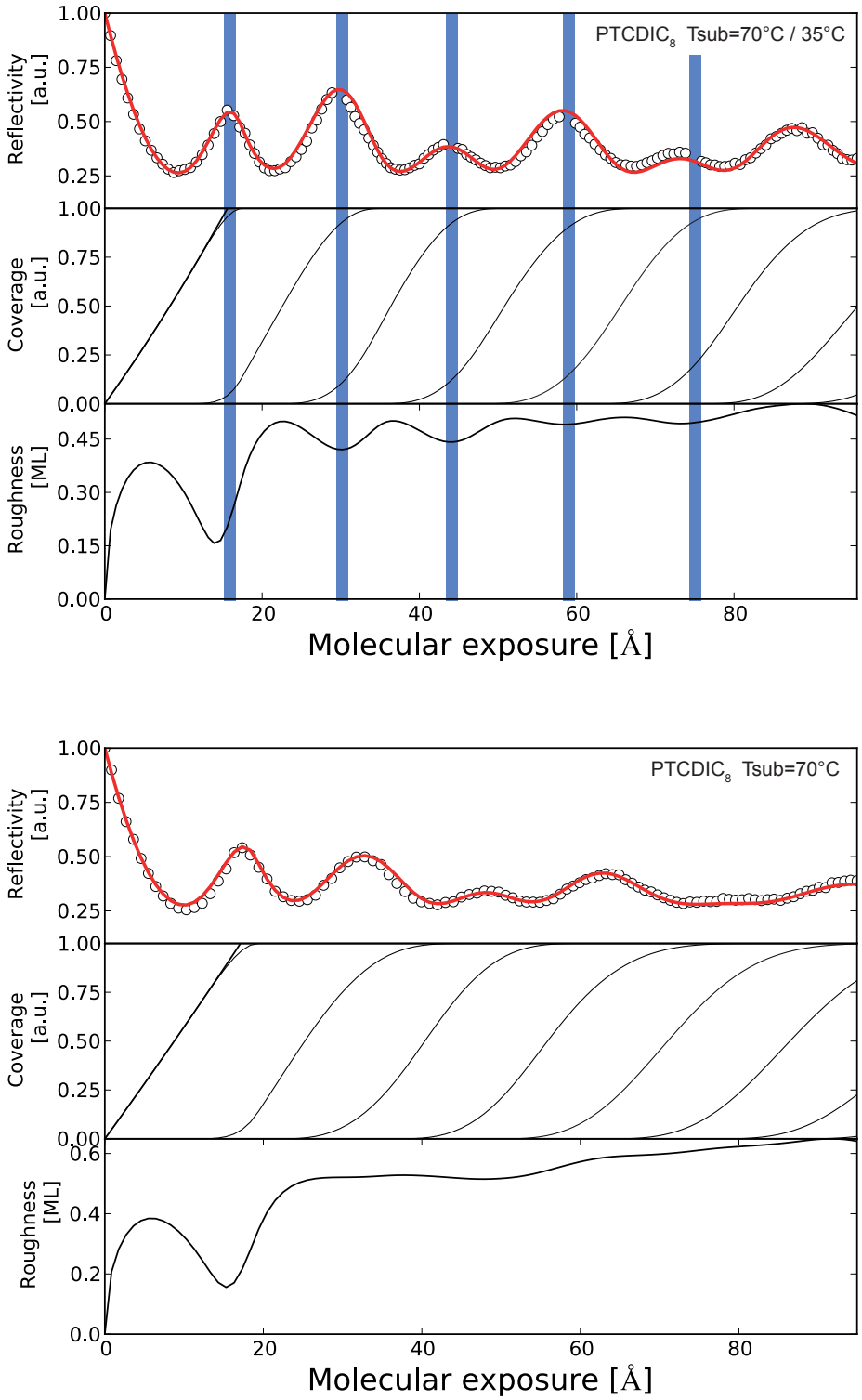

FIGURE A.8: Growth of PTCDI-C_8 thin films of 7 monolayer thickness with (top) and without (bottom) temperature modulations. We find an persistent influence of the temperature modulations in the surface roughness of the 5^{th} and 6^{th} monolayer. Blue: Period of reduced substrate temperature.

A.4. Temperature Modulated Growth of para-Sexiphenyl

Dynamic temperature control during growth gives rise to the possibility to grow para-Sexiphenyl (6p) thin films at elevated temperatures where conventional OMBD thin film growth is not possible. At 150 °C 6p does not stick on silica substrates. Employing dynamic temperature control allows us to cool down the substrate at the beginning of thin film growth (here to 80 °C) and pursue growth at 150 °C base temperature afterwards. The film in Figure A.9 grown at constant temperature (130 °C) shows the anti-Bragg oscillations that reveal pronounced layer-by-layer growth for the first two monolayers, where the surface roughness reduces once the according layer is complete filled. For upper monolayers this layer smoothening due to complete layer filling is not observed.
The damping in the growth oscillations of the film grown under temperature modulations (150 °C / 80 °C) is significantly reduced which is an indication for more pronounced layer-by-layer growth in the upper monolayers. Based on the rate equation model we extract roughness reductions also for the third and forth monolayer which we could not observe for films grown at constant temperature.
For the 2nd, 3rd and 4th monolayer the critical coverages (Table A.2) are increased by 10 to 15% through the temperature modulations and increased base temperature.

	const. 130°C	T_{mod} 150°C/80°C
$\theta_{1,\mathrm{crit}}$ [norm.]	78.0 %	78.0 %
$\theta_{2,\mathrm{crit}}$ [norm.]	48.3 %	64.1 %
$\theta_{3,\mathrm{crit}}$ [norm.]	23.5 %	57.2 %
$\theta_{4,\mathrm{crit}}$ [norm.]	20.7 %	42.5 %
$\theta_{5,\mathrm{crit}}$ [norm.]	10.9 %	9.4 %
$\theta_{6,\mathrm{crit}}$ [norm.]	7.5 %	5.4 %
$\theta_{7,\mathrm{crit}}$ [norm.]	3.0 %	2.6 %
layer spacing [Å]	27.8	27.8
q_z [Å^{-1}]	0.1096	0.1096

Table A.2.: Fit parameters for the rate equation model to reproduce the growth oscillations shown in Figure A.9.

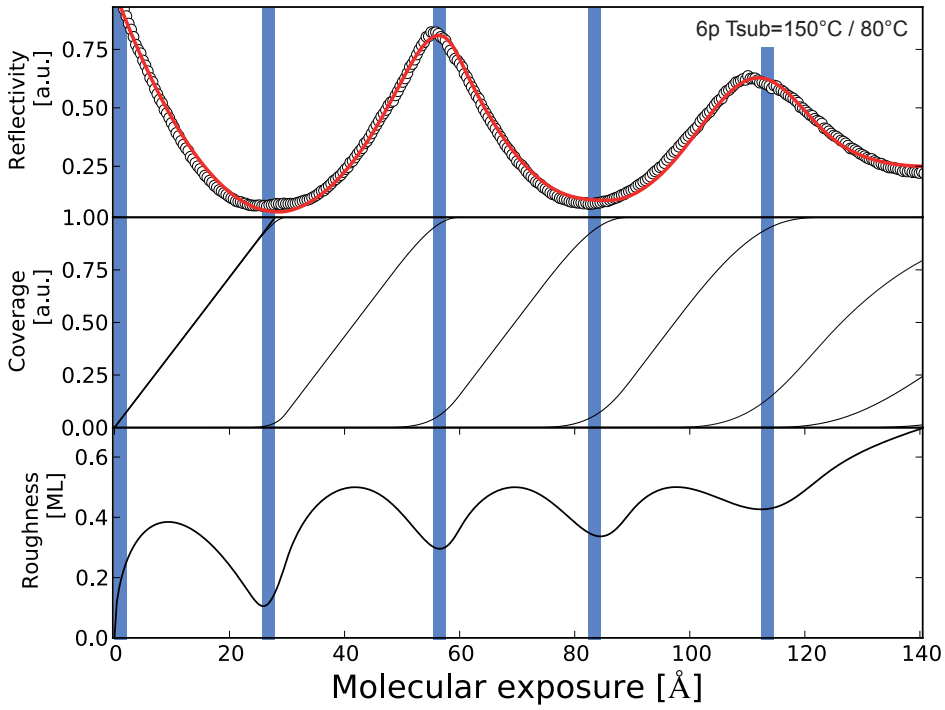

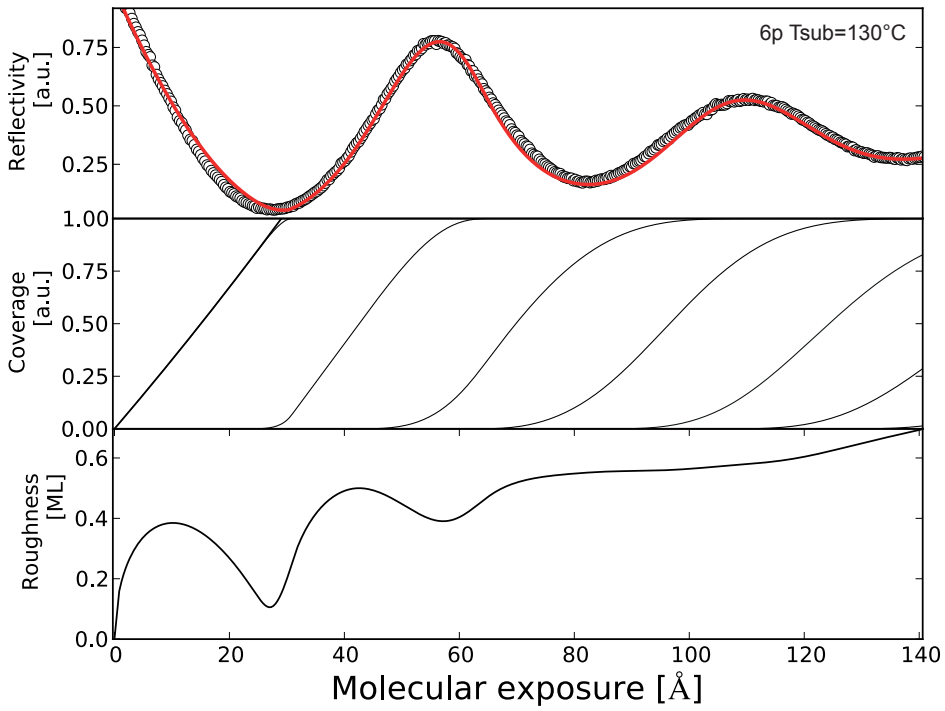

FIGURE A.9: para-Sexiphenyl growth oscillations and fits with (top) and without (bottom) temperature modulation during growth. Blue: Period of reduced substrate temperature.

A.5. Temperature Modulated Growth of Diindenoperylene

We have investigated the influence of thermal cycles as described in Chapter 6 on the growth of Diindenoperylene (DIP). For DIP we find under certain conditions (temperature modulations 130 °C vs 95 °C) a more pronounced smoothening for completely filled monolayer covarages as visible in the surface roughness extracted from anti-Bragg fits shown in Figure A.10. The according layer coverages are listed in Table A.3. While the impact of the temperature modulations on critical layer coverages is comparable to what we find for other molecules, the influence on the overall shape of the surface roughness evolution seems limited.
Not shown here is a dataset grown at 90 °C base temperature that we compared to a sample grown with 90 °C vs 40 °C temperature modulated growth. Under theses conditions we found significantly less influence of the temperature so that further experiments are needed for a confident interpretation of the results.

	const. 130°C	T_{mod} 130°C/95°C
$\theta_{1,\mathrm{crit}}$ [norm.]	78.9 %	77.2 %
$\theta_{2,\mathrm{crit}}$ [norm.]	58.4 %	77.2 %
$\theta_{3,\mathrm{crit}}$ [norm.]	58.4 %	76.8 %
$\theta_{4,\mathrm{crit}}$ [norm.]	49.6 %	70.7 %
$\theta_{5,\mathrm{crit}}$ [norm.]	16.0 %	26.9 %
$\theta_{6,\mathrm{crit}}$ [norm.]	14.9 %	15.0 %
$\theta_{7,\mathrm{crit}}$ [norm.]	17.8 %	16.2 %
layer spacing 1$^{\mathrm{st}}$ ML [Å]	16.97	17.15
layer spacing upper ML [Å]	17.07	17.07
q_z [Å$^{=-1}$]	0.181	0.187

Table A.3.: Fit parameters for the rate equation model to reproduce the growth oscillations shown in Figure A.10.

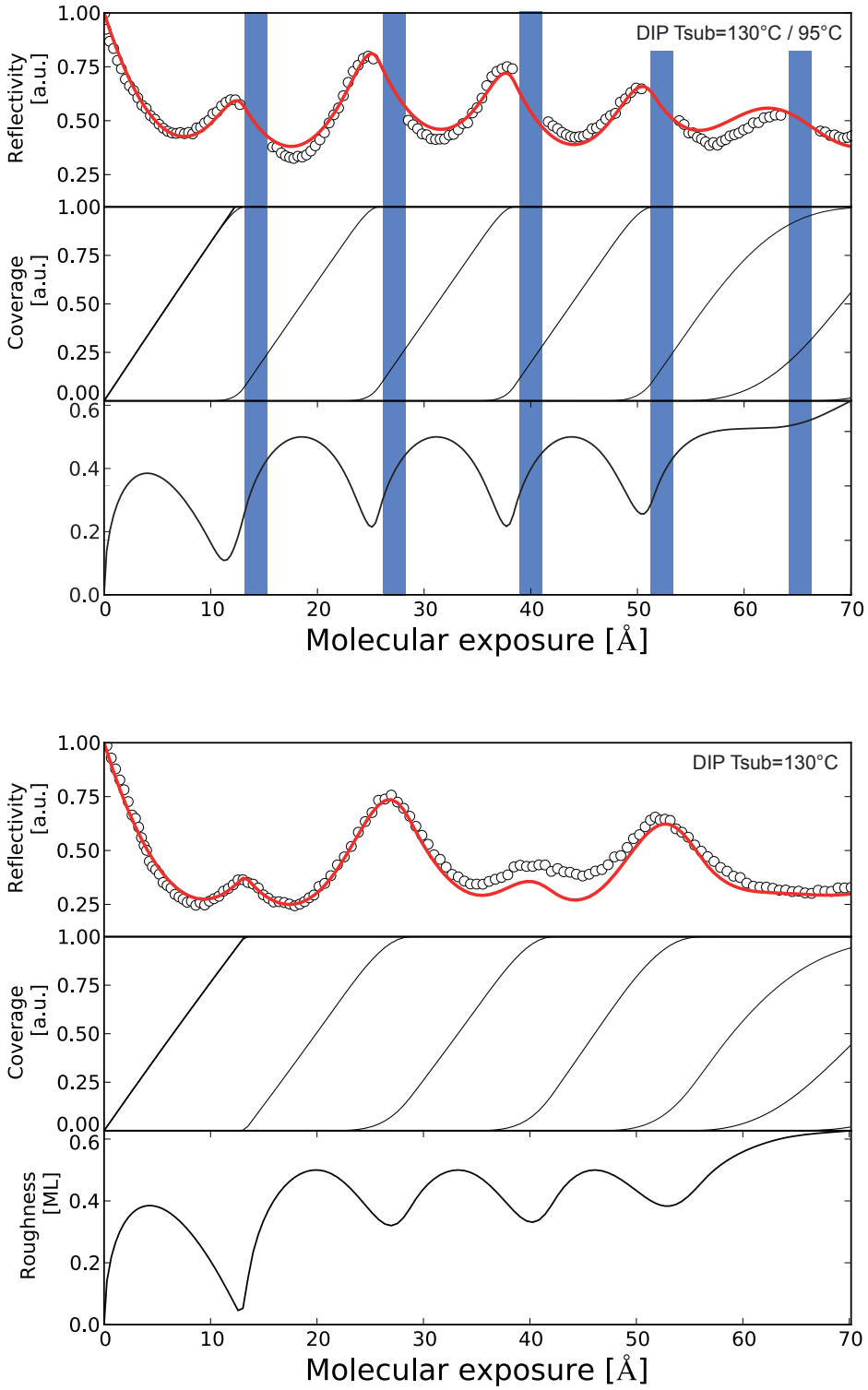

FIGURE A.10: Diindenoperylene growth oscillations and fits with (top) and without (bottom) temperature modulation during growth. Blue: Period of reduced substrate temperature.

B

Determining Ehrlich-Schwoebel Barrier through Critical Layer Coverages

Based on the approach by Meyer *et al.*[232] to assume that the critical ad-atom concentration on top of an island at the moment of second layer nucleation is equal to the concentration between the islands, it is possible to obtain a approximating expressions for the Ehrlich-Schwoebel Barrier.[184,233,234] However, this approach is not always accepted in literature as differing boundary conditions in the layer and on top of the islands may suggest a different ad-atom density on top of the islands compared to the one between the islands for second layer nucleation (e.g. in [183] chap. 4 footnote 18).

Following the approach by Meyer and assuming round islands, Markov[233] formulates

$$e^{-\frac{E_s}{k_b T}} = \frac{R_c}{2a}\left(\frac{1}{\theta_c} - 1\right) \tag{B.1}$$

with the critical radius for second layer nucleation R_c, E_s the Ehrlich-Schwoebel barrier, θ_c the critical coverage and a the spacing between absorption sides. In a compatible form Šmilauer and Harris[184] express

$$e^{\frac{E_s}{k_b T}} \approx \frac{2L}{R_c} - \frac{R_c}{2} \tag{B.2}$$

assuming the same attempt frequencies for intra- and inter-layer diffusion. Here L is half the distance between two islands. They also state that others[235] would rather write $\frac{8L}{R_c} - \frac{R_c}{2}$ instead. Using the relation $\theta_c = \pi R_c^2/4L^2$ and applying the logarithm, the formula

reads

$$E_s \approx k_B T \, ln \left[\frac{L}{\sqrt{\pi}} \left(\frac{\pi}{\sqrt{\theta_c}} - \sqrt{\theta_c} \right) \right]. \tag{B.3}$$

Disregarding the true island shapes found in PTCDI-C_8 films, assuming round islands and applying Equation B.3 to the experimental data (all length provided in the units of lattice constants), we find $E_s \approx 200\, meV$. The order of magnitude of this value of the energy barrier seems plausible when comparing it with what is found for other molecules.[29,236]. To extract reliable values based on this approach, the real island shape has to be considered.

C

Numerical Details of Phase Field Simulations

The results of the phase field simulations presented in Chapter 6.1 are produced using a *JAVA* code developed in the framework of this thesis inspired by Yu *et al.*.[30] The finite difference scheme is kept very basic to reduce computational costs. The time integration is realised in a simple Euler forward method, it can however simply be replaced by a *Runge Kutta 4* scheme due to the object oriented nature of the code. All derivative kernels are chosen symmetric to prevent asymmetric numerical drift. The laplacian $\nabla^2\Phi$ is calculated using the kernel

$$\begin{bmatrix} 0 & 1 & 0 \\ 1 & -4 & 1 \\ 0 & 1 & 0 \end{bmatrix}. \tag{C.1}$$

More delicate is the implementation of the term $\nabla\left[D(\mathbf{r},t)\nabla u(\mathbf{r},t)\right]$ as it contains two spatially varying quantities. We choose to implement it in a way that the flux[1] across each boundary to neighbouring lattice points is calculated separately to avoid the need to calculate $\nabla D(\mathbf{r},t)$ as $D(\mathbf{r},t)$ is not derivable at island boundaries due to the discontinuity induced by the Ehrlich Schwoeble barrier applied at singular lattice points. This discontinuity leads to a reduced stability when solving Equation 3.25 numerically.
A second problem arises from the identification of step edges in Φ. In the following we describe how we overcome these problems in a two step process, first the step edges in Φ are identified and then $\nabla\left[D(\mathbf{r},t)\nabla u(\mathbf{r},t)\right]$ is calculated.

[1] amount of $u(t)$ diffusing into / out of a neighbouring lattice side

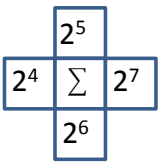

FIGURE C.1: Bits in step index SI_{ij} that have to be set if the concerned neighbour's coverage is integer-wise smaller than the one of the central lattice side.

Detecting Boundaries To identify the islands' 'boundaries' (outermost pixel in the upper ML) we pursue the following steps:

- **1. Step**
  Count how many of the 8 next neighbours have smaller (integer) coverage Φ than the central lattice side. (Just adding 1 for each position to the step index variable SI_{ij})

- **2. Step**
  In case there are more than 6 next neighbours with lower coverage, we do not consider the field as a step edge side since we do not want islands that are smaller than 4 lattice sides to have an Ehrlich-Schwoebel barrier to avoid numerical artefacts. This criteria ensures that the diffusion of freshly deposited u works without complications. If there are between 1 and 6 next neighbours with lower coverage the 2^3 bit in step index variable SI_{ij} will be set and we continue with step 3. In case there are 0,7,8 next neighbours with lower coverage we set the SI_{ij} to 0.

- **3. Step**
  To identify in which direction there are lower lying next neighbours, we set bits in SI_{ij} according to Figure C.1

Calculation of $\nabla\left[\mathbf{D}(\mathbf{r},\mathbf{t})\nabla\mathbf{u}(\mathbf{r},\mathbf{t})\right]$ To implement step edge barriers in the diffusion equation for $\frac{du}{dt}$ the material transport between certain pixels is exposed to reduced diffusion constant D, therefore, D is a spatially varying quantity. A straight forward approach to $\nabla\left[D(\mathbf{r},t)\nabla u(\mathbf{r},t)\right]$ would be the calculation of $\nabla D(\mathbf{r},t)\nabla u(\mathbf{r},t) + D(\mathbf{r},t)\nabla^2 u(\mathbf{r},t)$, however, as $D(\mathbf{r},t)$ is discontinuous at step-edges in $\Phi(\mathbf{r},t)$ we cannot calculate $\nabla D(\mathbf{r},t)$ easily. To work around this problem we make use of Green's first identity and calculate the flux across the boundaries of lattice points. To secure mass conservation we follow the convention to always consider the diffusion constant of the position into which the flow of u is directed. In the following we use the inplane diffusion constant D_R and step edge diffusion constant D_{ES}.

- **central lattice side without step-edge boundary**
  $\nabla(D\nabla u)_{11} = (D\nabla^2 u) = D_R \cdot (u_{01} + u_{10} + u_{12} + u_{21} - 4u_{11})/\Delta_x^2$

- **with step-edge boundary** as in Figure C.2b

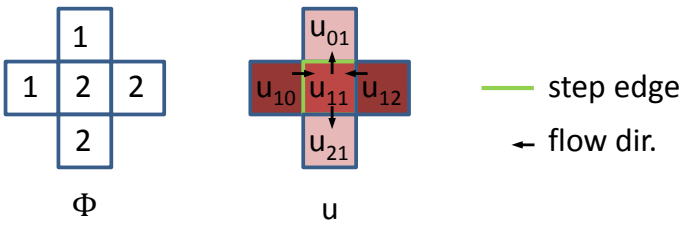

FIGURE C.2: The different cases that occur during the calculation of $\nabla\left[D(\mathbf{r},t)\nabla u(\mathbf{r},t)\right]$ in a pathologic example for u and ϕ. Dark red levels in u symbolise high u values and thus specify the flow direction.

$$\nabla^2(Du)_{11} = \left[\underbrace{D_{ES}\cdot(u_{01}-u_{11})}_{p_{01}} + \underbrace{D_R\cdot(u_{10}-u_{11})}_{p_{10}} + \underbrace{D_R\cdot(u_{12}-u_{11})}_{p_{12}} + \underbrace{D_R\cdot(u_{21}-u_{11})}_{p_{21}}\right]/\Delta_x^2$$

In general this reads as

$$\nabla(D\nabla u)_{11} = (p_{01}+p_{10}+p_{12}+p_{21})/\Delta_x^2 \tag{C.2}$$

$$p_{01} = \left\{\begin{array}{ll} D_{ES} & \text{if } u_{11} < u_{01} \text{ and } (0x20 \text{ and stepindex}_{11}) \\ D_{ES} & \text{if } u_{11} > u_{01} \text{ and } (0x40 \text{ and stepindex}_{01}) \\ D_R & \text{otherwise} \end{array}\right\} \cdot (u_{01}-u_{11}) \tag{C.3}$$

$$p_{10} = \left\{\begin{array}{ll} D_{ES} & \text{if } u_{11} < u_{10} \text{ and } (0x10 \text{ and stepindex}_{11}) \\ D_{ES} & \text{if } u_{11} > u_{10} \text{ and } (0x80 \text{ and stepindex}_{10}) \\ D_R & \text{otherwise} \end{array}\right\} \cdot (u_{10}-u_{11}) \tag{C.4}$$

$$p_{12} = \left\{\begin{array}{ll} D_{ES} & \text{if } u_{11} < u_{12} \text{ and } (0x80 \text{ and stepindex}_{11}) \\ D_{ES} & \text{if } u_{11} > u_{12} \text{ and } (0x10 \text{ and stepindex}_{12}) \\ D_R & \text{otherwise} \end{array}\right\} \cdot (u_{12}-u_{11}) \tag{C.5}$$

$$p_{21} = \left\{\begin{array}{ll} D_{ES} & \text{if } u_{11} < u_{21} \text{ and } (0x40 \text{ and stepindex}_{11}) \\ D_{ES} & \text{if } u_{11} > u_{21} \text{ and } (0x20 \text{ and stepindex}_{21}) \\ D_R & \text{otherwise} \end{array}\right\} \cdot (u_{21}-u_{11}) \tag{C.6}$$

Δ_x represents the distance between two points on the calculation grid in units of the crystal lattice constant.

Glossary

ν_0	attempt frequency
θ_n	layer coverage of n^{th} layer
ξ_n	feeding zone contributing to the growth of the n^{th} layer
$\mathbf{D}_-$	transition dipole moment of upper Davydov compoment
$\mathbf{D}_+$	transition dipole moment of lower Davydov compoment
E_D	energy barrier of diffusion
E_{ES}	Ehrlich-Schwoebel barrier

6p	para-sexiphenyl ($C_{36}H_{26}$)
6T	α-sexithiophene ($C_{24}H_{14}S_6$)
AFM	atomic force microscopy
DFT	density functional theory
DIP	diindenoperylene ($C_{32}H_{16}$)
DRS	differential reflectance spectroscopy
GISAXS	grazing incidence small angle x-ray scattering
GIXD	grazing incidence x-ray diffraction
HOMO	highest occupied molecular orbital
HT	high temperature phase
LDSA	light directed molecular self assembly
LT	low temperature phase
LUMO	lowest unoccupied molecular orbital
ML	monolayer
OFET	organic field effect transistor
OLED	organic light emitting diode
OMBD	organic molecular beam deposition
PEN	pentacene ($C_{22}H_{14}$)
$PTCDIC_8$	N,N'-Dioctyl-3,4,9,10-perylenedicarboximide ($C_{40}H_{42}N_2O_4$)
QCM	quartz crystal micro balance
S_0	molecular ground state (singlet)
S_1	first exited state (singlet)
TDM	transition dipole moment
TTC	N-tetratetracontane ($C_{44}H_{90}$)
XRR	x-ray reflectivity

List of Figures

V

Attachments

Publications & Presentations

Peer reviewed publications

2016

Direct photoalignment and optical patterning of molecular thin films
L. Pithan, P. Beyer, L. Bogula, A. Zykov, P. Schäfer, J. Rawle, C. Nicklin, A. Opitz, S. Kowarik; **Adv. Mater. 2016, 1604382**

Diffusion and nucleation in multilayer growth of PTCDI-C_8 studied with in situ x-ray growth oscillations and real-time small angle x-ray scattering
A. Zykov, S. Bommel, C. Wolf, **L. Pithan**, C. Weber, P. Beyer, G. Santoro, J. P. Rabe, S. Kowarik; **The Journal of Chemical Physics, 146, 052803 doi: 10.1063/1.4961460**

Cooperative switching in nanofibers of azobenzene oligomers
C. Weber, T. Liebig, M. Gensler, A. Zykov, **L. Pithan**, J.P. Rabe, S. Hecht, D. Bléger, S. Kowarik; **Scientific Reports 6, 25605**

Polymorphism in α-sexithiophene crystals: Relative stability and transition path
B. Klett, C. Cocchi, **L. Pithan**, S. Kowarik, C. Draxl; **Phys. Chem. Chem. Phys., 18, 14603-14609**

Dynamic substrate temperature modulations for enhanced layer-by-layer growth in organic thin films
L. Pithan, L. Bogula, G. Duva, A. Zykov, A. Gerlach, F. Schreiber, S. Kowarik; **in preparation**

2015

Light controls polymorphism in thin films of sexithiophene
L. Pithan, C. Cocchi, H. Zschiesche, C. Weber, A. Zykov, S. Bommel, S. Leake, P. Schäfer, C. Draxl, S. Kowarik; **Crystal Growth & Design 15 (3), 1319-1324**

2015 *Thermally driven smoothening of molecular thin films: Structural transitions in n-alkane layers studied in real-time*
L. Pithan, E. Meister, C. Jin, C. Weber, A. Zykov, K. Sauer, W. Brütting, H. Riegler, A. Opitz, S. Kowarik;
The Journal of Chemical Physics 143 (16), 164707

Light-controlled "molecular zippers" based on azobenzene main chain polymers
C. Weber, T. Liebig, M. Gensler, **L. Pithan**, S. Bommel, D. Bléger, J. P Rabe, S. Hecht, S. Kowarik; **Macromolecules 48 (5), 1531-1537**

2014 *Controlling the growth mode of para-sexiphenyl (6P) on ZnO by partial fluorination*
M. Sparenberg, A. Zykov, P. Beyer, **L. Pithan**, C. Weber, Y. Garmshausen, F. Carlà, S. Hecht, S. Blumstengel, F. Henneberger, S. Kowarik;
Physical Chemistry Chemical Physics 16 (47), 26084-26093

Conference Contributions and Presentations

2016 ESRF, Grenoble, France: *Controlling organic thin film growth through external stimuli* (Invited talk)

DPG Spring Meeting Regensburg, Germany: *Towards large area atomically flat n-alkane layers: A real-time study of thermal annealing* (Talk)

ESRF User Meeting, Grenoble, France: *Real time diffuse and specular scattering for 3d characterisation of thin film growth* (Poster & Poster-Clip)

2015 European Conference on Crystal Growth (ECCG5), Bologna, Italy: *Controlling polymorphism in organic thin films by light* (Talk)

Universität Tübingen, Group Seminar AG Prof. Schreiber: *Controlling thin film structures with external stimuli* (Invited talk)

MRS Spring Meeting, San Francisco, USA: *Light control over polymorphism in evaporated molecular thin films* (Poster)

DPG Spring Meeting, Berlin, Germany: *Enhanced phase purity in sexithiophene thin films through laser illumination* (Poster)

2014 DPG Spring Meeting Dresden, Germany: *Influencing molecular thin film growth with light* (Talk)

2013 DPG Spring Meeting Regensburg, Germany: *Real-time studies on annealing of Tetratetracontane by X-Ray diffraction* (Poster)

Selbstständigkeitserklärung

Ich erkläre, dass ich die Dissertation selbständig und nur unter Verwendung der von mir angegebenen Hilfsmittel gemäß § 7 Abs. 3 der Promotionsordnung der Mathematisch-Naturwissenschaftlichen Fakultät, veröffentlicht im Amtlichen Mitteilungsblatt der Humboldt-Universität zu Berlin Nr. 126/2014 am 18.11.2014, angefertigt habe.

Berlin, den

Autorenbeitäge

Die Kapitel 4 und 7 wurden zu Teilen in den Erstautorpublikationen [76] and [188] veröffentlicht. Die Beiträge der Koautoren zu diesen Publikationen stellen sich wie folgt dar:

- Referenz [76]: L. Pithan entwickelte zusammen mit S. Kowarik das Konzept der Studie. Entwicklung des Versuchsdesign, der Datenauswertung und Literaturrecherche lagen nahezu vollständig bei L. Pithan. Neben L. Pithan waren H. Zschiesche, C. Weber, A. Zykov, S. Bommel und S. J. Leake an der Datenerhebung beteiligt. P. Schäfer trug beratend bei Fragen zur Interpretation der Resultate der Röntegenstreuexperimente bei. C. Cocchi und C. Draxl beteiligten sich durch die Berechung der theoretischen Absorptionsspekten sowie deren Analyse. Die Erstellung des Manuskripts lag in den Händen von L. Pithan, der durch Beiträger aller Koautoren unterstützt wurde.

- Referenz [188]: A. Opitz, S. Kowarik und W. Brütting schlugen das Projekt vor. E. Meister präparierte die Proben und erhob mit K. Sauer die Daten am Raster-Kraft Mikroskop. C. Jin und H. Riegler arbeiten mit L. Pithan bei optischen Mikroskopiemessungen zusammen. C. Weber und A. Zykov unterstützten L. Pithan bei den Röntegenbeugungsmessungen. Auswertung und Interpretation aller Daten erfolgte durch L. Pithan, ebenso wie Literaturrechere und die Erstellung des Manuskripts. Das Manuskirpt wurde von S. Kowarik und A. Opitz redigiert.

Hilfsmittel

Zusätzlich zu den in Literaturverzeichnis und Fußnoten angegebenen Quellen wurden folgende Softwarepakete verwendet: Origin 9, ImageJ, Mathematica 9, Gwyddion 2.3, Latex, Microsoft Powerpoint 2013, Adobe Illustrator CC, BlueJ 3.1, Java 8